Bedforms, macroturbulence, and sediment transport at the fluid-bed interface

Dissertation zur Erlangung des Doktorgrades der Naturwissenschaften
im Fachbereich Geowissenschaften der Universität Bremen
vorgelegt von

Eva Kwoll

Bremen, September 2013

Gutachter:

PD Dr. Christian Winter

Prof. Dr. Jeremy Venditti, Simon Fraser University, Kanada

Tag des Dissertationskolloquiums:

22. November 2013

Prüfungsausschuss:

PD Dr. Christian Winter

Prof. Dr. Jeremy Venditti

Prof. Dr. Dierk Hebbeln

Prof. Dr. Achim Kopf

Dr. Alice Lefebvre

Markus Benninghoff

Erklärung

Name: Eva Kwoll

Datum: 30 September 2013

Anschrift: MARUM

Leobenerstr

28359 Bremen

Hiermit versichere ich, dass ich

1. die Arbeit ohne unerlaubte fremde Hilfe angefertigt habe,

2. keine anderen als die von mir angegebenen Quellen und Hilfsmittel benutzt habe und

3. die den benutzten Werken wörtlich oder inhaltlich entnommenen Stellen als solche kenntlich gemacht habe.

Eva Kwoll

Bremen, den 30.09.2013

Abstract

Small scale morphodynamic processes at the fluid-bed interface in coastal environments are still not fully understood. Deformation of the seabed by hydrodynamic forces results in the occurrence of complex bedforms on a variety of scales. Owing to their interaction with the water column and turbulence production, large bedforms, such as dunes, significantly influence sediment transport and hydraulic roughness. Turbulence production above bedforms is predominately associated with large-scale coherent flow structures (macroturbulence). It has been suggested that macroturbulence is the principle mechanism behind the entrainment and transport of sediment in suspension.

The objective of this thesis was to investigate the formation and occurrence of macroturbulent structures and their coupling to suspended sediment transport forming downstream of natural bedforms. Specifically, the effect of flow unsteadiness and bedform geometry was examined. The research is based on multiple research approaches including two field campaigns into the German Elbe Estuary and Danish tidal inlet Knudedyb. Ship-based observations and lander-based moorings deploying acoustic Doppler current profilers and optical measurement probes were conducted. The field research was complemented by laboratory experiments and a 2DV numerical model study.

Results show that flow unsteadiness has significant implications on the production of macroturbulence. In both, the Elbe Estuary and the tidal inlet Knudedyb, very large compound bedforms occur in water depths of < 20 m. The primary bedforms remain ebb-oriented during a tidal cycle while smaller superimposed bedforms reverse direction with each tidal phase. Water-depth scale macroturbulence develops when flow direction and primary bedform orientation are aligned (ebb phase), once the accelerating ebb flow overcomes a velocity threshold. The frequency of macroturbulent structures falls into the Strouhal range of macroturbulence associated with flow separation zones downstream of bedforms. The flow structures originate in the region of high velocity gradients in the bedform lee and are traceable over the downstream bedform stoss-side.

The magnitude of turbulence production decreases with the slope of the bedform lee-side. Our laboratory and model results show that the velocity gradient downstream of bedforms decreases with lower lee-slopes. Low turbulence intensities above lower lee-slopes are attributed to a smaller scale of macroturbulent structures though this has yet to be verified. In the field, water-depth scale macroturbulence is absent when bedform orientation and flow direction are opposed (flood phase). The former gentle-sloping ebb stoss-side now serves temporally as the hydraulic

lee-side. High velocity and pressure gradients are absent preventing the generation of macroturbulence of this scale.

Macroturbulent structures are responsible for the rapid upward transport and mixing of suspended sediment. In the Elbe Estuary, sediment within flow structures forms distinct clouds of sediment with cohesive properties. Confined clouds can be observed for up to one hour after their first occurrence, even after they merge to form larger structures. In the Knudedyb, such cohesive properties are absent. Sediment disperses more rapidly under the high flow velocities of the upper water column. During the flood tide, due to the absence of water-depth scale macroturbulence, suspended sediment transport is smaller in magnitude and believed to be associated with turbulence generated at the secondary bedforms. Transport distances are limited by the steep flow-facing flank of the primary bedforms. The complexity of these processes currently lacks adequate description and might result in under- or overestimation of regional sedimentary budgets.

The variability of macroturbulence production due to flow unsteadiness causes a change in hydraulic roughness between tidal phases. Hydraulic roughness is also shown to vary for bedforms with equal height and length, based on the lee-slope. Our results demonstrate that there is a need for current generations of morphodynamic models to take into account the variability of hydraulic roughness induced by flow unsteadiness, the relative orientation of flow to bedforms, and lee-slope characteristics.

Zusammenfassung

Bis heute sind kleinskalige, morphodynamische Prozesse an der Grenzschicht Sohle/Wassersäule in Küstengewässern kaum verstanden. Hydrodynamische Kräfte verformen die bewegliche Sohle und bilden Bodenformen unterschiedlicher Größen. Großskalige bodenformen, wie zum Beispiel Dünen, haben großen Einfluss auf den Sedimenttransport und die Bodenrauhigkeit durch Wechselwirkungen mit der Wassersäule und Produktion von Turbulenz. Der Hauptanteil der Turbulenzproduktion findet in Form von großskaligen Wirbelstrukturen (Makroturbulenz) statt. Es wird angenommen, dass Makroturbulenz für den Großteil der Erosion und des Transportes von Sediment in Suspension verantwortlich ist.

Ziel dieser Arbeit ist es die Entstehung und das Vorkommen von Makroturbulenz über Bodenformen zu untersuchen. Außerdem soll der Zusammenhang zwischen Makroturbulenz und dem Transport von Sediment in Suspension erforscht werden. Insbesondere soll die Auswirkung von instationären Strömungen und Geometrie der Bodenformen untersucht werden. Diese Forschungsarbeit beruht auf mehreren Methoden. Zum Einen wurden zwei Ausfahrten unternommen, eine in das Ästuar der Elbe und eine weitere in das dänische Seegatt Knudedyb. Hier wurden vom Schiff aus und mit Hilfe von stationären Plattformen hydro-akustische und optische Messungen durchgeführt. Zusätzlich wurden aufwendige Experimente im Labor durchgeführt und mit einem numerischen 2DV Model verbunden.

Die Ergebnisse zeigen, dass instationäre Strömungen große Folgen auf die Ausbildung von Makroturbulenz haben. Im Elbe Ästuar und Knudedyb Seegatt befinden sich sehr große „compound“ (engl. zusammengesetzt) Bodenformen in Wassertiefen von < 20 m. Die primären Bodenformen sind stets in Richtung der Ebbströmung ausgerichtet, während die sekundären, überlagernden Bodenformen ihre Orientierung der Gezeitenströmung anpassen. Wenn die Strömungsrichtung und Orientierung der Primär-Bodenformen parallel sind (Ebb Phase) entsteht Makroturbulenz, welche die Ausmaße der Wassertiefe erreicht. Die Wirbelstrukturen treten auf, sobald die Ebbströmung einen Geschwindigkeitsgrenzwert überschreitet. Die Frequenz der Wirbelstrukturen fällt in den Bereich der Strouhal Frequenzen, die Makroturbulenz aus den Bereichen der Strömungsablösung hinter Bodenformen zugeschrieben wird. Die Wirbelstrukturen werden in den Bereichen hoher Geschwindigkeitsgradienten in der strömungsabgewandten Seite (Lee) der Bodenformen erzeugt. Sie können entlang der strömungszugewandten Seite (Luv) der nächsten Bodenform verfolgt werden.

Die Magnitude der Turbulenzproduktion nimmt mit der Neigung der Lee-Seite der Bodenform ab. Unsere Labormessungen und Modellergebnisse zeigen, dass der Geschwindigkeitsgradient hinter Bodenformen mit niedrigerer Lee-Neigung abnimmt. Geringe turbulente Intensitäten bei geringeren Lee-Neigungen werden mit kleinskaligerer Makroturbulenz verbunden, obwohl dies

noch bestätigt werden muss. Makroturbulenz, die das Ausmaß der Wassertiefe erreicht, tritt nicht in unseren Feldmessungen auf, wenn Strömungsrichtung und Orientierung der Bodenformen entgegengesetzt sind (Flut Phase). Die gering geneigte Ebb-Luv-Seite, bildet vorübergehend die Flut-Lee-Seite. Hohe Geschwindigkeits- oder Druckgradienten sind in dieser Konstellation nicht vorhanden, sodass Makroturbulenz von dieser Größe nicht generiert wird.

Makroturbulente Wirbelstrukturen sorgen für den aufwärts gerichteten Transport und die Vermengung von suspendiertem Sediment. Im Elbe Ästuar bilden sich Trübungswolken durch die kohäsiven Eigenschaften des Sediments in den Wirbelstrukturen. Einzelne Wolken können noch bis zu einer Stunde, nachdem sie bereits mit anderen Wolken vermischt wurden, beobachtet werden. Im Knudedyb sind solche kohäsiven Eigenschaften nicht vorhanden. In der oberen Wassersäule unterliegt Sediment einer schnelleren Dispersion, durch Vorherrschen von höheren Strömungsbedingungen. Während der Flut ist der Transport von Sediment in Suspension geringer, da großskalige Makroturbulenz nicht vorhanden ist, und stattdessen nur kleinerskalige Turbulenz der Sekundär-Bodenformen auftritt. Die steile, in die Strömung gewandte Seite der primären Bodenformen begrenzt die Reichweite des Transportes in Suspension. Diese komplizierten Wechselwirkungen können heute noch nicht eindeutig beschrieben werden. Die Unsicherheit kann zur Über- oder Unterschätzung des regionalen Sedimenteintrags führen.

Die Unterschiede in der Produktion von Makroturbulenz durch instationäre Strömungen führen zu wechselnder Bodenrauhigkeit zwischen einzelnen Tidenzyklen. Es wurde auch gezeigt, dass die Bodenrauhigkeit für Bodenformen mit gleicher Höhe und Länge variiert, wenn die Neigung der Lee-Seite variiert. Unsere Ergebnisse zeigen, dass ein Bedarf daran besteht, dynamische Rauhigkeitsbeschreibungen in aktuelle morphodynamische Modelle zu implementieren. Solche Beschreibungen sollten instationäre Strömungen, die relative Orientierung von Bodenformen und Strömung, und die Eigenschaften der Lee-Seite in Betracht ziehen.

Table of Contents

List of Figures

List of Tables

List of Symbols

C	Chèzy roughness coefficient	$[m^{1/2}\ s^{-1}]$
c	suspended sediment concentration	$[g\ L^{-1}]$
D	grain diameter	[m]
D_{50}	50 percentile of grain diameter distribution	[m]
f	frequency	[Hz]
f_v	eddy shedding frequency (Simpson, 1989)	[Hz]
f_w	wake flapping frequency (Simpson, 1989)	[Hz]
Fr	Froude Number	-
g	gravitational acceleration	$[m\ s^{-2}]$
H	bedform height	[m]
h	water depth	[m]
I	number of ensembles	-
k_s	effective roughness height	[m]
κ	von Kármán constant	-
L	bedform length	[m]
$Q1_s$	spatial quadrant 1 ($u'_s > 0, w'_s > 0$)	-
$Q1_t$	temporal quadrant 1 ($u'_t > 0, w'_t > 0$)	-
$Q2_s$	spatial quadrant 2 ($u'_s < 0, w'_s > 0$)	-
$Q2_t$	temporal quadrant 2 ($u'_t < 0, w'_t > 0$)	-
$Q3_s$	spatial quadrant 3 ($u'_s < 0, w'_s < 0$)	-
$Q3_t$	temporal quadrant 3 ($u'_t < 0, w'_t < 0$)	-
$Q4_s$	spatial quadrant 4 ($u'_s > 0, w'_s < 0$)	-
$Q4_t$	temporal quadrant 4 ($u'_t > 0, w'_t < 0$)	-
q_u	horizontal sediment flux	$[kg\ s^{-1}\ m^{-2}]$
q_w	vertical sediment flux	$[kg\ s^{-1}\ m^{-2}]$
R^2	coefficient of determination	-
Re	Reynolds number	-
ρ_s	sediment density	$[kg\ m^{-3}]$
ρ_w	water density	$[kg\ m^{-3}]$
S	water surface slope	-
Sr	Strouhal number	-
T	transport stage	-

TKE_{uw}	vertical turbulent kinetic energy	[Pa]
τ_*	Shields number	-
τ_{*cr}	critical Shields number for sediment entrainment	-
τ_T	total shear stress	[Pa]
τ_{uw}	Reynolds stress	[Pa]
u	streamwise velocity	[m s^{-1}]
U	transect-averaged velocity magnitude	[m s^{-1}]
U_b	Bulk mean flow velocity	[m s^{-1}]
U_0	average velocity upstream of the step	[m s^{-1}]
u_*	shear velocity	[m s^{-1}]
u_{rms}	root-mean-square of streamwise velocity	[m s^{-1}]
v	spanwise velocity	[m s^{-1}]
w	vertical velocity	[m s^{-1}]
w_{rms}	root-mean-square of vertical velocity	[m s^{-1}]
w_s	settling velocity	[m s^{-1}]
x	distance along bedform	[m]
z	height above the seabed	[m]
z_0	roughness length	[m]
z_c	convergence height of log-profiles	[m]
□	placeholder to be substitutes by either u, w, c	
$□'_s$	spatial deviation of quantity □	[as □]
$□'_t$	temporal fluctuation of quantity □	[as □]
$\overline{□}_t$	time-averaged quantity □	[as □]
$\widetilde{□}$	transect-averaged quantity □	[as □]
<□>	spatial mean of quantity □ along streamlines	[as □]

Acknowledgements

Funding for this project was received through the DFG Research Centre and Excellence Cluster "The Ocean in the Earth System" held at MARUM – Center for Marine Environmental Sciences hosted at the University of Bremen. The project originated in 10.2010 within the former framework of the subproject SD4 – Dynamics of the fluid-bed interface, and is since 06.2013 incorporated into the SD1 subproject - Bridging scales: From small-scale morphological and sedimentological features to coastal and shelf systems. Research was conducted within the coastal dynamics research group at MARUM.

Additional funding for conference visits and a research stay was obtained through the GLOMAR graduate school and an 'Impulse grant' through the Central Research Development Fund at the University of Bremen. A 6-month research stay was conducted in the Environmental Fluid and Sediment Dynamics Laboratory held at the Simon Fraser University in Burnaby, Canada.

This thesis would not have been possible without the continuous support of my supervisor, Christian Winter, who offered the opportunity to freely develop the research questions and approaches comprising this thesis. I greatly value his constant care, affirmation and guidance throughout the past three years. I would also like to thank Jeremy Venditti, who provided the opportunity to conduct research at SFU and by agreeing to act as the second Examiner of this thesis, has shown continuous interest and support of my work.

Within the coastal dynamic research group, I have found both, a thriving team of young coastal researchers and friends that made the day-to-day working environment productive and enjoyable. I am especially thankful to Marius Becker, for his expertise on ADCPs and contributions to the first and second manuscript of this thesis. I furthermore would like to thank Alice Lefebvre for her contribution to the third paper, continuous feedback on all forms of scientific presentation and for the great efforts she has taken to regularly bring our individual floating minds together. I thank both, Alice and Marius for their clear heads in the last weeks of this thesis when mine wasn't. Thank you, and also Tina and Gauvain for proof-reading parts of this thesis.

My strength has always relied on the close network of my friends and family. Thank you for traveling distances to see me, many phone calls, letters and emails supporting my random choices of places to live. Thank you for your understanding, when at times I seemingly disappear into work and the little signs of care in form of office visits, food parcels and post cards that mean so much.

CHAPTER 1 - GENERAL INTRODUCTION

1.1. INTRODUCTION

The world's coastal zones are highly dynamic systems due to the mutual interaction of marine and terrestrial processes. The complexity of these interactions results in a great diversity of coastlines, ranging e.g., from rocky cliffs to sandy beaches, and ecologically-rich tidal embayments. Increasingly, these natural coastal processes are interfered by anthropogenic activity: rising socio-economic demands alter the natural coastline, peaking in heavily engineered coastal metropoles and port constructions. Coastal zone management strategies have emerged on national and international level (e.g., the International Coastal Zone Management (ICZM) by the European Commission), attempting to mediate between competing socio-economic interests in future development while attaining to the overarching goal of sustainability. Such frameworks highlight the need for a detailed understanding and prediction of the coastal system.

The key aspect for predicting future development of coastal areas is to fundamentally understand governing physical and biogeochemical processes. This comprises identification of hydrodynamic drivers (wind, waves, tidal currents, and river discharge) and their role in erosion, transport and deposition of particulate matter (sediments, organics, and pollutants). Regarding the sedimentary system, the term "morphodynamics" was coined to encompass the mutual adjustment of the governing hydrodynamics and seabed morphology by sediment transport [*Wright and Thom*, 1977] under the influence of boundary conditions (e.g., hydrodynamic drivers, sediment characteristics and availability) [*Winter*, 2011]. For a given location, these morphodynamic processes act on a variety of spatial and temporal scales (e.g., bedform formations in tidal channels, evolution of tidal shoals, tidal channel migration).

A variety of research methodologies is applied to determine morphodynamic processes within their range of spatio-temporal scales: in-situ techniques involve the monitoring of seabed morphology, sediment transport and hydrodynamics via long-term moorings or short-term surveys from a boat or plane. Modeling approaches help to overcome limited financial and time resources by interpolation and extrapolation of field data. Physical models are applied for research applications involving small-scale morphodynamic processes. They comprise the down-scaling of the governing processes to laboratory scale. Under controlled boundary conditions, the environmental parameters of interests are monitored. Numerical models suites are a tool widely applied for the various scales of morphodynamic processes.

Numerical models mathematically solve the governing equations of relevant processes on a discretized grid. Current generations of morphodynamic models rely on simplified parameterizations partially to achieve computational feasibility (e.g., application of turbulence closure schemes instead of direct numerical simulation) and partially due to the currently still incomplete deterministic understanding of sediment-fluid interactions.

The author of this thesis contributed to the on-going research on morphodynamic models by evaluating the potential of current modeling suites in (1) compensating the lack of field data regarding surficial sediment distribution in tidal inlets or estuaries [*Kwoll and Winter*, 2011] (2) evaluating specific hydrodynamic drivers of heavy mineral deposits in the coastal area [*Badesab et al.*, 2012].

Qualitative investigations readily made with current morphodynamic models, still suffer from significant shortcomings that need to be overcome for accurate quantitative predictions [*Davies et al.*, 2002; *Winter et al.*, 2006]. This is due to the empirical formulations used in the derivation of hydraulic roughness and sediment transport formulations. Currently used formulations typically stem from observations in simplified laboratory conditions (i.e., simple dune geometries, simplified grain size distribution). Often, hydraulic roughness is averaged over the model grid scale and treated as a simple calibration coefficient. The natural variability in grain size distributions and bedform configurations under unsteady flow conditions can currently not be accounted for. A more detailed understanding regarding the interaction between the seabed and flow field on a bedform scale is vital in overcoming the present shortcomings [*Parsons and Best*, 2013].

This doctoral thesis compiles recent work of the author regarding the interaction of flow and bedforms in variable coastal settings. After the introduction on the research background (**section 1.2**), main objectives are formulated (**section 1.3**). A detailed thesis outline is presented in **section 1.4**. Three research projects form the main core of the thesis (**Chapter 2-4**). Research findings are summarized and concluded in **Chapter 5**.

1.2. Background

Bedforms are seabed features with distinct and often periodic geometric properties developing through the interaction of flow with a mobile bed. A great variety of bedform geometries exists on a number of spatio-temporal scales, owing to the availability and textural variability of sediment and prevailing hydrodynamic drivers. In the coastal area, bedforms commonly exceed hundreds of meters in length and several meters in height, occupying up to one third of the water depth. Bedforms of this scale provide substantial resistance to the flow, and thus are the predominant contributor to hydraulic roughness. A detailed discussion of theories regarding the origin of bedforms is given by Coleman and Nikora [2011] and Venditti [2013].

Common flow features above bedforms are converging, accelerating flow above the upward-sloping bedform stoss-side and flow expansion and deceleration above the downward-sloping lee-side (**Figure 1.1**). Previous research focused mainly on laboratory studies of asymmetric dunes, characterized by a long, gentle sloping stoss-side and short steep lee-side close to the angle-of-repose [e.g., *Nelson et al.*, 1993; *Bennett and Best*, 1995; *Kadota and Nezu*, 1999; *Venditti and Bennett*, 2000; *Wren et al.*, 2007] (**Figure 1.1a**). Here, the high pressure gradient downstream of the bedform crest induces the formation of a separated shear layer that reattaches 4-6 bedform heights downstream. A flow recirculation cell is formed in the bedform lee. Downstream of the flow reattachment point an internal boundary layer develops with increasing vertical extent towards the crest. A wake region, characterized by high turbulence intensities, originates along the shear layer and overlies the internal boundary layer.

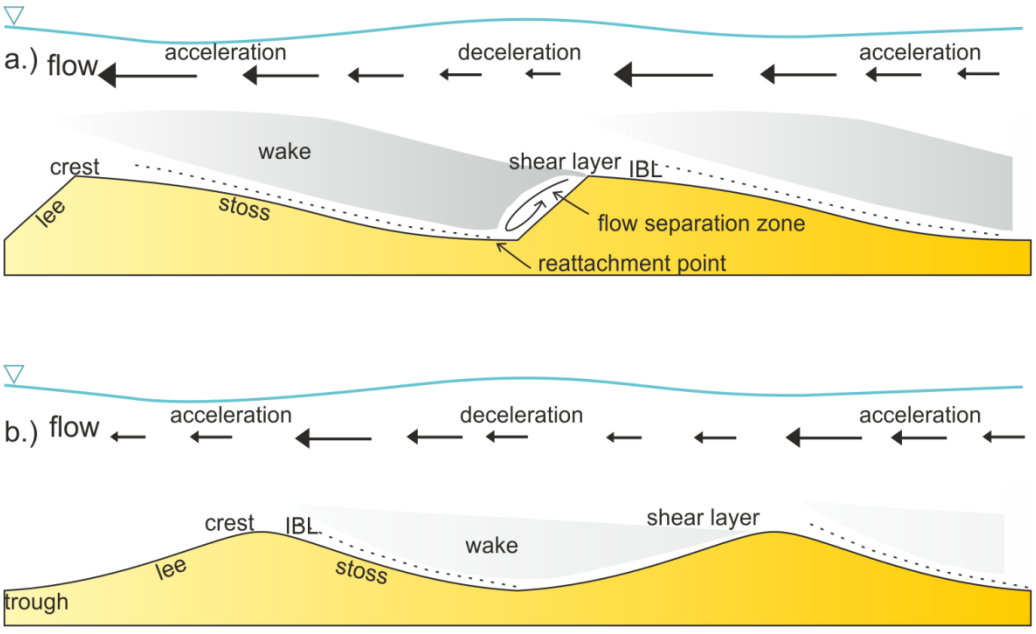

Figure 1.1. Flow field characteristic above (a) bedforms with a lee-slope close to the angle-of-repose and (b) low-angle symmetric bedforms adapted from Venditti [2013]. IBL = internal boundary layer.

A variety of bedform symmetry ratios are known to occur in nature with the majority of observed bedform lee-slopes being smaller than the angle-of-repose (usually < 14°) [e.g., *Smith and McLean*, 1977; *Gabel*, 1993; *Kostaschuk and Villard*, 1999; *Carling et al.*, 2000; *Sukhodolov et al.*, 2006]. In this case flow separation in the bedform lee is absent or possibly intermittent [*Best and Kostaschuk*, 2002]. Nonetheless, a shear layer, internal boundary layer, and wake region are also found over such low-angle bedforms without permanent flow separation [*Best and Kostaschuk*, 2002; *Sukhodolov et al.*, 2006] (**Figure 1.1b**).

Bedforms cause hydraulic roughness (form roughness) through the extraction of mean flow momentum for turbulence production. Turbulence production above bedforms is predominately associated with large-scale turbulence (macroturbulence) originating in the bedform lee-side [e.g., *Kadota and Nezu*, 1999; *Schmeeckle et al.*, 1999; *Stoesser et al.*, 2008; *Chang and Constantinescu*, 2013]. Many studies suggest macroturbulence forms in the bedform lee due to flow separation (*Bennett and Best*, 1995; *Venditti and Bennett*, 2000; *Shugar et al*., 2010). However, macroturbulence has also been observed in the absence of permanent flow separation above low-angle bedforms [*Kostaschuk and Church*, 1993; *Best and Kostaschuk*, 2002], suggesting that low-angle bedforms also contribute to hydraulic roughness.

Macroturbulent structures are advected along the entire water depth and erupt at the water surface as boils [*Matthes*, 1947; *Jackson*, 1976; *Babakaiff and Hickin*, 1996; *Best*, 2005a]. Recent laboratory investigations and numerical modeling studies have examined the origin and topology of bedform-related macroturbulence [*Kadota and Nezu*, 1999; *Stoesser et al.*, 2008; *Grigoriadis et al.*, 2009; *Omidyeganeh and Piomelli*, 2011; *Chang and Constantinescu*, 2013] with no clear consensus. Macroturbulence and boils have been attributed to hairpin-shaped streamwise oriented vortices developing downstream of reattachment [*Best*, 2005a; *Stoesser et al.*, 2008; *Chang and Constantinescu*, 2013] or spanwise vortices (termed roller structures or vortex tubes) originating from Kelvin-Helmholtz instabilities along the shear layer [*Venditti and Bennett*, 2000; *Grigoriadis et al.*, 2009; *Omidyeganeh and Piomelli*, 2011]. The later mechanism has also been proposed for macroturbulence production in the absence of flow separation along the wall-bound shear layer [*Best and Kostaschuk*, 2002].

Macroturbulent structures above natural bedforms have been linked to the entrainment and transport of sediment in suspension [*Lapointe*, 1992; *Kostaschuk and Church*, 1993; *Kostaschuk and Villard*, 1999; *Shugar et al.*, 2010]. Although, bedform dynamics are commonly attributed to the transport of sediment as bedload, observations in the field suggest that suspended sediment transport also plays an important role in bedform dynamics and geometry [*Kostaschuk et al.*, 2009]. Increased amounts of suspended sediment transport are believed to cause the low

symmetry ratios and low lee-slopes observed in the field [*Smith and McLean*, 1977; *Kostaschuk and Villard*, 1996b, 1999].

Knowledge on the effect of flow unsteadiness on the above described processes, caused e.g., by the regular reversal of the tidal currents in the coastal area, is scarce. Hierarchies of bedforms are observed frequently in tidal inlets and estuaries in the form of compound bedforms [e.g., *Dalrymple and Rhodes*, 1995; *Ernstsen et al.*, 2006; *Lefebvre et al.*, 2011]. Compound bedforms consist of large primary bedforms on which smaller secondary bedforms are superimposed. Due to their smaller sediment volume, secondary bedforms are able to adapt orientation on time-scales of tidal cycles while primary bedforms remain stably oriented in the net flow direction [*Dalrymple and Rhodes*, 1995; *Ernstsen et al.*, 2006; *Lefebvre et al.*, 2011]. As a result the primary bedform orientation is in temporal disequilibrium with the hydrodynamic forcing for half of the tidal cycle (**Figure 1.2**). In this case, form roughness is varyingly attributable to either secondary only, or secondary and primary bedform influence depending on the tidal phase (*Lefebvre et al.,* 2011, 2013a).

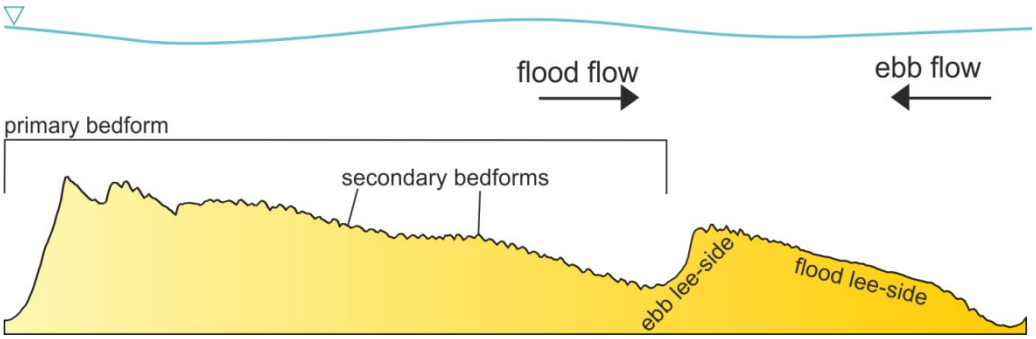

Figure 1.2. Terminology of ebb-oriented compound bedforms commonly found in tidal environments.

1.3. OBJECTIVES

Recent detailed field measurements examined the scale and frequency of macroturbulence and its coupling to sediment suspension above natural bedforms [*Best et al.*, 2010; *Shugar et al.*, 2010; *Bradley et al.*, 2013]. However, owing to the great variability of bedforms and environmental parameters found in nature, the current understanding is still too limited to enable adequate parameterization for application in regional-scale models [*Parsons and Best*, 2013].

Many open questions remain: When is flow separation considered permanent? What are the implications of intermittent separation? How do macroturbulent structures form? What determines the scale and frequency of macroturbulent structures? How can estimates of scale and frequency of macroturbulence be related to hydraulic roughness? What are the effects of flow unsteadiness? How is sediment entrained and transported in macroturbulent structures? What are the implications for bedform morphology and dynamics?

This thesis investigates macroturbulence production and coupling to suspended sediment transport above varying bedform geometries and hydrodynamic forcing. The specific objectives are:

- Assessment of the presence / absence of flow separation and shear layer characteristics downstream of bedforms with varying lee-slope angles
- Investigation of the occurrence and origin of macroturbulence above natural bedforms
- Estimation of the effect of flow unsteadiness and compound morphology on macroturbulence production
- Observation of the coupling of macroturbulence and suspended sediment transport
- Investigation of the implications of variable bedform geometry and flow unsteadiness on hydraulic roughness

1.4. THESIS OUTLINE

The doctoral thesis is arranged in a cumulative format. The following chapters consist of three scientific manuscripts concerned with a specific research project. The research projects subsequently evolved during the course of the thesis and are ordered chronologically.

Chapter 2 is based on a field studies and examines the regular occurrence of distinct clouds of sediment above very large tidally-influenced compound bedforms in the Elbe Estuary (Germany). The sediment-laden clouds occurring during accelerating ebb currents are linked to macroturbulent structures originating in the bedform lee-side. Results combine ship-surveys with lander-based hydro-acoustic measurements.

Chapter 3 investigates the influence of regular flow reversal above asymmetric bedforms on the production of macroturbulence and suspended sediment transport in a Danish tidal inlet. A combination of hydro-acoustic data from ship-based profiling and stationary moorings are presented. A scale-difference is observed of macroturbulence production and magnitude and suspended sediment transport between tidal phases.

Chapter 4 focusses on the effect of the bedform lee-slope on the turbulence and flow field in a detailed laboratory study conducted in the Environmental Fluid and Sediment Dynamics Laboratory (Simon Fraser University, Burnaby, CA). The laboratory data is combined with a 2DV numerical model. Shear layer, flow separation and wake characteristics for a number of bedform geometries are examined.

Chapter 5 is a synthesis of the findings in this study and concludes the thesis.

CHAPTER 2 - PAPER I

INTERMITTENT SUSPENSION AND TRANSPORT OF FINE SEDIMENT OVER NATURAL TIDAL BEDFORMS

Eva Kwoll[1], Christian Winter[1] and Marius Becker[1]

[1] MARUM-Center for Marine Environmental Sciences, University of Bremen, Germany

Based on a book chapter published in *Coherent Flow Structures at the Earth's Surface*, eds. J.G. Venditti, J.L. Best, M. Church and R.J. Hardy, Wiley-Blackwell in 2013.

ABSTRACT

In the tidal environment of the Elbe estuary (German North Sea coast) the intermittent suspension of sediment over large tidal bedforms is revealed by the periodic appearance of large (10 – 20 m diameter) sediment-laden clouds at the water surface. In this environment, two separately acting sedimentary regimes are identified: active ebb-directed tidal bedforms (1.5 - 4 m high, 50 - 100 m long, lee-side angles 10 – 15°) of medium to coarse sands, and a fine sediment load (< 170 μm) repeatedly forming an ephemeral fluid mud layer at low energy tidal stages in the bedform troughs. Hydro-acoustic and optical measurements reveal coherent flow structures forming in the lee of the bedforms to be linked to formation of the clouds, the upward transfer and maintenance in the water column. Turbidity cloud appearance is restricted to accelerating flow conditions and occurs only after a hydrodynamic threshold has been overcome. Around this time suspended sediment transport is governed by large coherent flow structures. Under maximum current velocities, although flow structures continue to prevail, suspended sediment transport appears to be decoupled from the initial flow structures, resulting in a homogenous sediment mixture. Estimates of the frequency of surface clouds and coupled flow structures are within the range of previously observed coherent flow structures in laboratory and field studies.

2.1. Introduction

The processes leading to the entrainment, transport and deposition of fine-grained sediment in estuarine environments are governed by complex feedback mechanisms between the hydrodynamic forcing, sediment characteristics and seabed topography. Previous studies documented the fundamental role of intermittent turbulent events on sediment entrainment and proposed coherent flow structures to be the principle mechanism involved in the vertical mixing of fluid momentum, temperature, nutrients and sediment [e.g., *Lapointe*, 1992, *Kostaschuk and Church*, 1993, *Venditti and Bennett*, 2000]. In the Elbe Estuary (German North Sea Coast) the intermittent nature of fine-grained, cohesive sediment transport is revealed by the appearance of large (10 – 20 m) sediment-laden clouds at the river surface. The occurrence of clouds is restricted to certain tidal stages and appears to be linked to the presence of boils, the surface expression of large low-velocity upward-tilting vortices originating near the seabed [*Matthes*, 1947, *Coleman*, 1969, *Jackson*, 1976, *Rood and Hickin*, 1989, *Babakaiff and Hickin*, 1996, *Winter et al*., 2007].

Boils are common features in river flows and the literature on boil origin and associated eruption frequencies is widespread: several researchers attribute boils to macroturbulent phenomena associated with roughness elements on the seabed: in dune fields with flow separation large vortices are believed to be generated at the brink point and the reattachment point of the separation streamline [e.g., *Kostaschuk and Church*, 1993, *Bennett and Best*, 1995, *Venditti and Bennett*, 2000] or from 'flapping' of the wake layer [e.g., *Nezu and Nakagawa*, 1993, *Best*, 2005a]. In case of low angle dunes and in absence of flow separation, it has been suggested that vortices originate at intermittent shear gradients in the dune lee [*Kostaschuk and Villard*, 1999, *Best et al.*, 2001, *Best and Kostaschuk*, 2002]. Furthermore, in the absence of bedforms, several authors have attributed boil producing turbulent motions to microturbulent boundary layer bursting phenomena [*Jackson*, 1976, *Yalin*, 1992].

Several studies report increased suspended sediment concentrations (SSC) in boil structures compared to the ambient flow [e.g., *Lapointe*, 1992, *Best*, 2005a, *Czuba et al.*, 2011]. However, it is still unclear which mechanisms promote entrainment of sediment from the seabed [*Coleman and Nikora*, 2011], what are the characteristics of the sediment entrained (both in terms of grain size and quantity) and how the interaction with the free surface may affect the dispersal of sediment transported upward within these structures [*Best*, 2005b]. Particularly in tidal environments, subject to strong velocity gradients and regular reversal of the flow, in-situ measurements of the turbulent flow and suspended sediment transport are rare, due to the difficulties encountered when measuring in the field. This study therefore aims at a high-resolution in-situ monitoring of processes involved in the formation of the turbidity clouds above a series of tidal bedforms. Focusing on the time scale of a tidal cycle will enable to get

process based insights into the generation mechanisms of clouds and their dependency on tidal flow conditions, the propagation of clouds to the surface, and the mechanisms maintaining the sediment in suspension and inside the confined structures. Our findings will add to the current understanding off short-term suspended sediment transport variability, vital in the attempts to predict sediment transport in such complex environments.

2.2. Field site and data acquisition

2.2.1. Setting

The Elbe River is the largest tidal river in Germany with a catchment area of 132,000 km^2 and an annual mean freshwater discharge of 720 m^3 s^{-1} [*Kerner*, 2007] into the German Bight. A spring tidal range of 4 m places the Elbe between the classifications of meso- and macro-tidal estuaries [*Kappenberg and Grabemann*, 2001]. Tides are semidiurnal with a distinct asymmetry towards ebb [*Kappenberg et al.*, 1995]. The study area is located 30 km upstream of the Elbe estuary mouth at the northern margin of a river bend (**Figure 2.1a**). At this location large compound tidal bedforms cover the seafloor in water depths of 10 – 30 m. Under average discharge conditions the study area is located in the reach of the turbidity maximum zone, which stretches approximately 30 km along the river, the midpoint situated circa 10 km further upstream [*Grabemann et al.*, 1995]. Annual mean concentrations of suspended matter in the Elbe are 0.035 g L^{-1} and can reach values 10-fold within the turbidity maximum zone [*Kappenberg and Grabemann*, 2001].

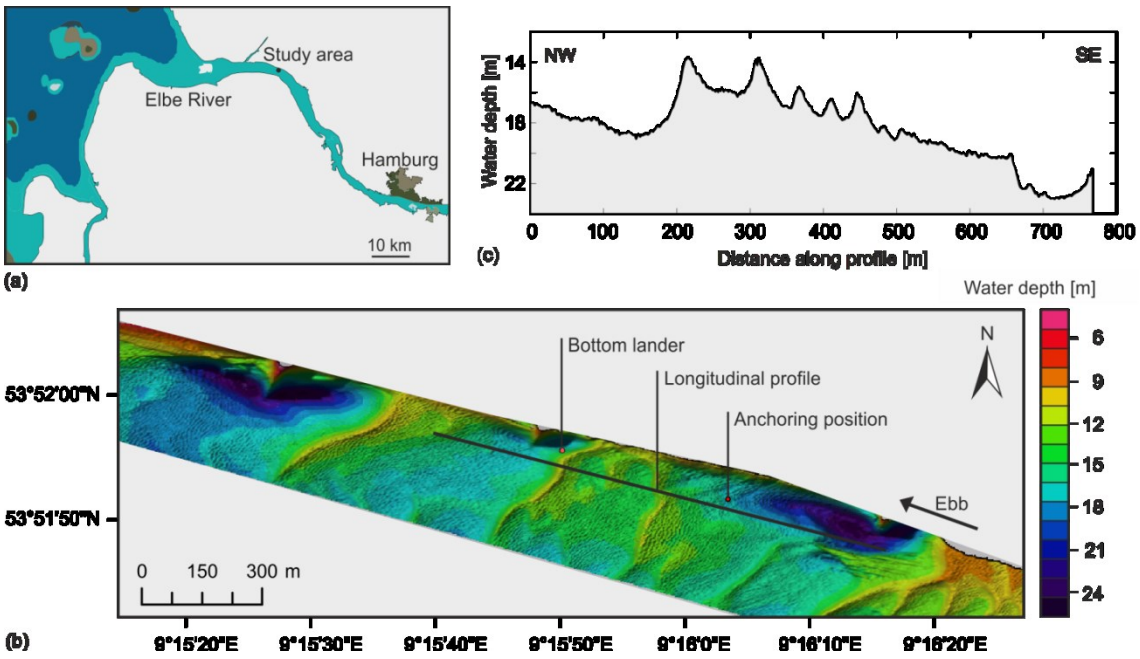

Figure 2.1. (a) The location of cloud monitoring in the Elbe Estuary, 30 km upstream the river mouth. (b) Bathymetry [m] in the study area. The location of the bottom lander, the anchoring position for June 23rd and the longitudinal transect are indicated. The large ebb-directed bedforms are on average 3 m high and 100 m long with lee-side angles of 10 - 15°. The topography is interspersed by large depressions associated with sluices at the river margin. (c) Vertical transect of the monitored longitudinal profile.

2.3. Field campaign

A field campaign was carried out in June 2010 combining optical and hydro-acoustic measuring techniques: equipped with a downward-looking acoustic Doppler current profiler (ADCP; 1200 kHz, TRDI workhorse), a bottom lander was deployed for five days, located in the upper lee-side close to the tidal bedform crest (**Figure 2.1b**). Additionally, data was collected on longitudinal transects along a series of tidal bedforms, using a downward-looking ADCP (600 kHz, TRDI workhorse) and a multibeam echo sounder (MBES; 455 kHz, SeaBat 8125 RESON). Covering a profile length of approximately 1 km, profiles were collected every 30 min during one 12.5 h tidal cycle. A single transect took between 10 and 15 minutes, during which the ship was navigated against the main current direction at low speed, perpendicular to the bedform crests. Surface sediments were taken by means of a Shipek grab sampler along the same transect.

During a second tidal cycle, stationary ship-borne measurements were conducted at anchor; the location is indicated in **Figure 2.1b**. In addition to the ship-borne ADCP, a multi-sensor probe was deployed at a constant water depth of 1.1 m recording turbidity, salinity and temperature variations at the water surface. In order to derive water samples for the calibration of ADCP backscatter and optical turbidity sensor data regarding suspended sediment concentration, the multi-sensor probe was in a third deployment veered to a water depth of 2 and 5 m every half hour for a tidal cycle to collect water samples (via pumping); meanwhile the ship-borne ADCP was continuously recording.

The ping rate of the ship-borne ADCP was set to 2.3 s, with a bin size of 0.5 m. Taking into account the deployment depth of 1.35 m and the blanking distance of 1.05 m, the first measurement was located in a depth of 2.4 m. The ADCP mounted on the bottom lander was deployed at a height of 2.5 m above the seabed. Considering a blanking distance of 0.6 m, the uppermost measurement was located at a height of 1.9 m above the seabed. Ping rate and cell size were 4 s and 0.1 m, respectively.

2.4. Data analysis methods

2.4.1. Sediment analysis

A total number of 32 bed samples and 46 water samples were collected during the field campaign. The bed samples and 34 water samples were analyzed for particle size distributions (PSD) by means of a Coulter Beckmann Laser Particle Sizer (laser Diffraction method) covering the range 0.04-2000 µm. It is noted that the PSD analysis was performed on dispersed material, i.e., flocs and aggregates were destroyed before processing. All water samples were filtered, dried, and weighted to derive suspended sediment concentrations.

2.4.2. Flow velocities

ADCP current velocity measurements were converted to earth coordinates [RD Instruments, 2008]. Ship borne ADCP data was geo-referenced using the onboard LRK GPS and corrected for ship speed using ADCP bottom track velocities. Then, streamwise (u) and spanwise (v) velocity components were determined by projecting current velocity vectors with respect to the ebb current direction.

2.4.3. Turbulence parameters

ADCP derived flow velocity profiles were analyzed to derive information on turbulence statistics throughout the water column [e.g., *Lu and Lueck*, 1999]. Streamwise (u') and vertical (w') velocity fluctuations were determined by subtracting instantaneous velocity values (u, w) from their time-averaged mean ($\overline{u}, \overline{w}$) at each depth. In order to include large-scale turbulent motions but to yield quasi-stationarity in respect to tidal variations an averaging window of 10 minutes was chosen [c.f., *Dyer*, 1997, *Soulsby*, 1980]. For stationary ADCP measurements, this implied averaging of 260 and 150 ensembles along equal bins for the ship-based and lander-based ADCP, respectively. In case of moving vessel ADCP transects, mean streamwise and vertical velocity at each depth (bin) were determined by spatiotemporal averaging of all ensemble measurements of one profile, assuming that during the profiling period of approximately 10 minutes no significant changes occurred in the overall tidal flow.

Streamwise and vertical velocity fluctuations were used to specify coherent fluctuation signatures in the flow field. Following quadrant analysis [*Lu and Willmarth*, 1973], velocity fluctuations for each bin were classified into a specific quadrant field: Q1 ($u'>0, w'>0$), Q2 ($u'<0, w'>0$), Q3 ($u'<0, w'<0$) and Q4 ($u'>0, w'<0$). Since velocity fluctuations in this study were derived not only from time- but also from spatially-averaged values, we differentiate the two methods by indexing a t for temporal and s for spatial consideration (e.g.,$Q1_t$ vs. $Q1_s$). In case of the stationary data, only velocity patterns meeting the condition $|u'w'| > 2\ u_{rms}\ w_{rms} = 0.001$ were considered, where *rms* is the root-mean square value, in order to distinguish low velocity fluctuations from events capable of suspended sediment [c.f., *Cellino and Lemmin*, 2004].

In the following, we refer to larger structures comprising several velocity measurements of one quadrant in the ADCP reading as coherent structures of common velocity signature or simply coherent flow structure.

2.4.4. ADCP backscatter and optical turbidity probe calibration

The ADCP echo intensity backscatter signal was calibrated to SSC profiles, using 34 water samples as described by Gartner [2004], Hill et al. [2003], Hoitink and Hoekstra [2005] and Kostaschuk et al. [2005]. Following Deines [1999], echo intensities recorded by the ADCP were

corrected for beam spreading and water absorption. The water absorption coefficient was calculated according to Ainslie and McColm [1998]. The backscatter intensity was further corrected for absorption due to suspended sediment, implementing the iterative algorithm described by Thorne et al. [1994] and applied, by Holdaway et al. [1999] on single-frequency hydroacoustic data. The sediment absorption coefficient was determined according to Urick [1948].

The CTD turbidity sensor (Seapoint OBS) on the multi-sensor probe was calibrated for SSC by using the same water samples and a linear regression model (SSC = 0.522 OBS + 3.7304; coefficient of determination R^2 = 0.818).

2.5. Results

2.5.1. Bedform dimensions

Large ebb-directed compound tidal bedforms characterized the sea bed topography at the field site in an approximate water depth of 17 m. Bedform dimensions along the longitudinal profile (**Figure 2.1c**) were estimated from MBES surveys. Primary bedforms were 1.5 – 4 m high with lengths of 50 - 100 m and lee-side angles varying between 10 - 15°. These primary bedforms were superimposed by smaller secondary bedforms with heights ranging between 0.3 – 0.8 m and lengths of 5 - 15 m.

2.5.2. Hydrodynamic and sedimentological characteristics

The tidal range during the observation period was 3.2 m. Maximum depth-averaged ebb currents were 1.4 m s^{-1}, while flood currents reached maximum values of 1.3 m s^{-1}. Increased freshwater discharge (1400 m^3 s^{-1} at Neu Darchau (130 km upstream), WSA Lauenburg) at the time of measurement relocated the turbidity maximum zone downstream of the field site, resulting in relatively low ambient suspended sediment concentrations.

Suspended sediment concentrations derived from 34 water samples in 2 and 5 m water depth ranged between 0.02 – 0.22 g L^{-1} throughout the tidal cycle, the minimum concentration occurring shortly after slack water. The samples showed only minor variation in terms of grain size distribution over the tidal cycle (c.f., exemplary curves in **Figure 2.2**). Sediment in suspension was generally smaller than 170 µm with a dominant mode between 40 – 60 µm (**Figure 2.2a**).

Particle sizes of bed sediments across the tidal bedform field ranged from 150-700 µm with median values of the uni-modal distribution lying between 336 and 546 µm (medium to coarse sands). Material from primary bedform troughs was characterized by a slight shift of the dominant mode towards finer material compared to bedform crest (c.f., exemplary curves in **Figure 2.2c**). For a short period after slack water a thin layer of fluid mud covered the sandy bed material in bedform troughs. Isolate grain size analysis of the fluid mud layer showed similar characteristics than the suspended sediments in the water samples (**Figure 2.2b**).

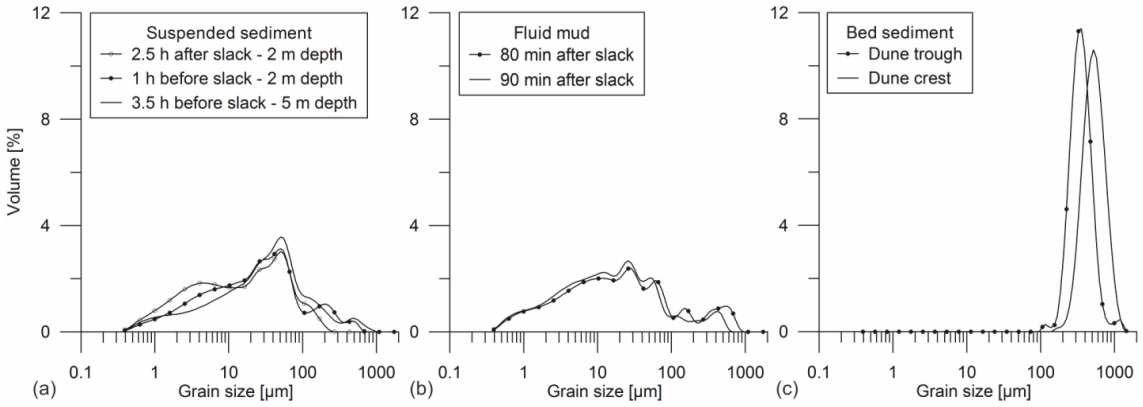

Figure 2.2. (a) Grain size distributions of suspended sediment from water samples, (b) of the fluid mud layer forming in the tidal bedform troughs shortly after slack water and (c) bed samples. The similarity of grain size distributions of fluid mud and sediment samples indicates that the source of the material suspended can be found in tidal bedform troughs.

2.5.3. Turbidity cloud description at the water surface

Turbidity clouds were visually observed at the water surface as circular features with a distinct brownish surface color at the onset of the accelerating tide, during the transition from flood to ebb, approximately 80 min after slack water. Cloud diameters varied between 10 - 20 m. The clouds were advected by the ambient flow and slowly increased in diameter. They partly merged to form larger structures, in which the original clouds were separated by thin bands of less turbid water. These characteristics were observable for up to 1 hour following the first cloud appearance.

The turbidity clouds showed upwelling characteristics, i.e., smooth patches of surface water, slightly elevated compared to the ambient water surface (**Figure 2.3**). Wind induced capillary waves refrained from propagating into the interior of the clouds but steepened and broke at the boundary of corresponding patches. The multi-sensor probe held at an approximate water depth of 1.1 m at the mooring position on June 23rd equipped with a CTD reveals distinct changes in temperature, salinity and suspended sediment concentration as clouds were advected past the sensors (**Figure 2.4**): abrupt increases in SSC (up to 0.25 g L^{-1}) are accompanied by decreases in temperature (up to 1 °C) and increases in salinity (up to 0.15).

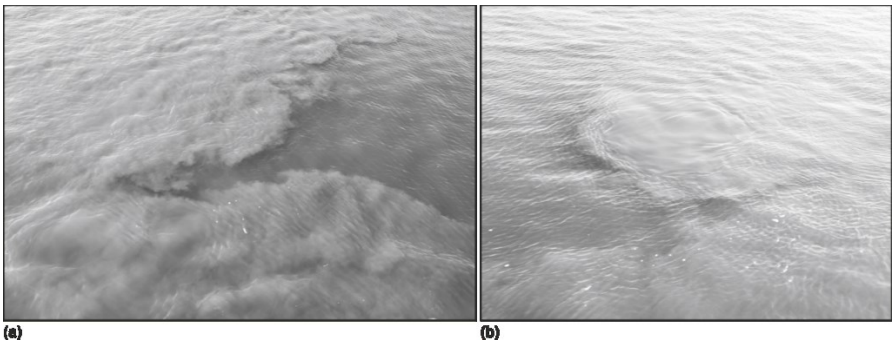

Figure 2.3. Turbidity clouds in the Elbe Estuary. (a) Clouds are clearly distinguishable from the surrounding clearer water by increased suspended sediment concentration (b) and topographic surface.

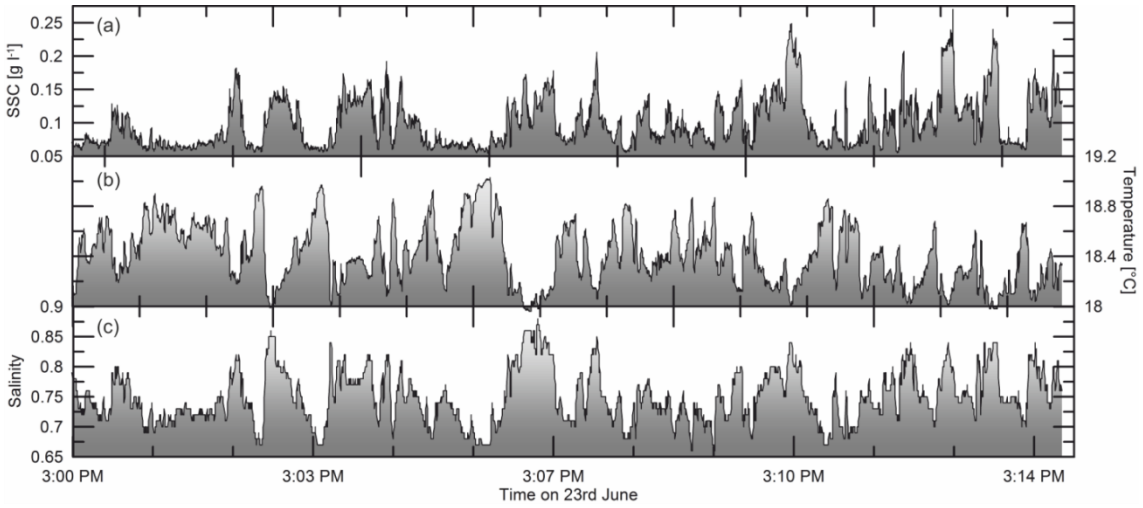

Figure 2.4. CTD record of period with clouds at the surface. (a) High SSC structures (increase of up to 0.075 g L^{-1}) are accompanied by (b) a drop in temperature (up to 1 °C) and (c) an increase in salinity (up to 0.15).

2.5.4. Turbidity cloud detection in the water column

Elongated structures of increased SSC appeared on calibrated ADCP backscatter profiles coinciding with cloud appearance on the water surface. **Figure 2.5a** depicts one of the profiles on June 22rd. The profile shows SSC distribution during accelerating ebb flow conditions (mean velocity of 1 m s^{-1}) 75 - 90 minutes after slack water. Structures of high SSC (up to 0. 3 g L^{-1}) are clearly distinguishable from the ambient water (average concentration below 0.05 g L^{-1}). Only a few structures extended down to the sea bed and were located at the stoss-side of the primary tidal bedforms.

2.5.5. Flow structure during cloud observation

The topographic forcing of the flow in the presence of tidal bedforms is shown by transects of ADCP flow velocity profiles (**Figure 2.5b-d**): streamwise velocity fluctuations (**Figure 2.5b**) showed accelerated flow over the stoss-side and the crest of the large compound bedforms and

decelerated flow in the lee-side throughout the entire water column, while vertical velocity fluctuations (**Figure 2.5c**) were positive over the stoss-side and crest and negative in the lee-side. The secondary bedforms exhibit a similar control on the flow, although the deceleration in the lee seems less pronounced and acceleration only affects the flow close to the bed. In general, the topographic forcing was evident over much of the water column and along the entire profile, apart from the range between meter 600 and meter 800, where areas of low streamwise velocity overlaid the acceleration over the stoss-side.

Common signatures of velocity fluctuations (**Figure 2.5d**) show coherent structures of accelerated upwelling flow ($Q1_s$ ($u'_s>0$, $w'_s>0$)) immediately coupled with areas of accelerated downwelling flow ($Q4_s$ ($u'_s>0$, $w'_s<0$)) at the crests of the primary tidal bedforms. Above the lee-side and troughs alternations of decelerated upward ($Q2_s$ ($u'_s<0$, $w'_s>0$)) and downward flow ($Q3_s$ ($u'_s<0$, $w'_s<0$)) prevailed. Over the stoss-sides of the primary bedforms the two coupled patterns coexist; a combination of $Q3_s$ /$Q2_s$ type structures in the upper water column and of $Q1_s$ /$Q4_s$ structures in the lower water column prevailed (c.f., meter 1200 – 1250).

2.5.6. Coherent flow and SSC structure variability on a tidal cycle

The occurrence of clouds during accelerating flow and the associated change in the flow structure was assessed, based on stationary ADCP measurements: the lander-based ADCP measured the near-bed water column in the upper lee of a large primary tidal bedform, while the vessel (ship-based ADCP) was moored above the mid-stoss-side (**Figure 2.1b**). Examples of flow structures and SSC dynamics in the entire water column are shown for a period of 1.5 h during accelerating ebb currents on June 23rd in **Figure 2.5e-h**, starting 50 min after slack water (13:40 UTC) (**Figure 2.5e**). Initially, SSC was at a minimum of less than 0.05 g L^{-1} except for the area 3 – 4 m above the seabed (**Figure 2.5f**). Around 15:00 UTC (80 min after slack water) a vertical pattern of SSC, alternating between low and higher SSC structures developed. This coincided with the first observation of clouds at the water surface. SSC increased further during accelerating ebb, the alternating pattern of high SSC and low SSC structures, however, prevailed. Simultaneously with the appearance of this vertical SSC pattern, the velocity fluctuations exceeded the threshold level to form vertical coherent structures with common velocity signatures (**Figure 2.5g**).

The near-bed velocity fluctuations, derived from the lander-based ADCP, support this observation: the first appearance of clouds coincided with the occurrence of coherent structures with common velocity signatures, occupying the entire profiling range of 1.9 m (**Figure 2.5h**). Coherent structures of $Q2_t$ ($u'_t<0$, $w'_t>0$) and $Q4_t$ ($u'_t>0$, $w'_t<0$) type signatures dominate, with periods of successive decelerated upwelling structures ranging between 60 – 150 s and a duration of single upwellings of 30 – 60 s.

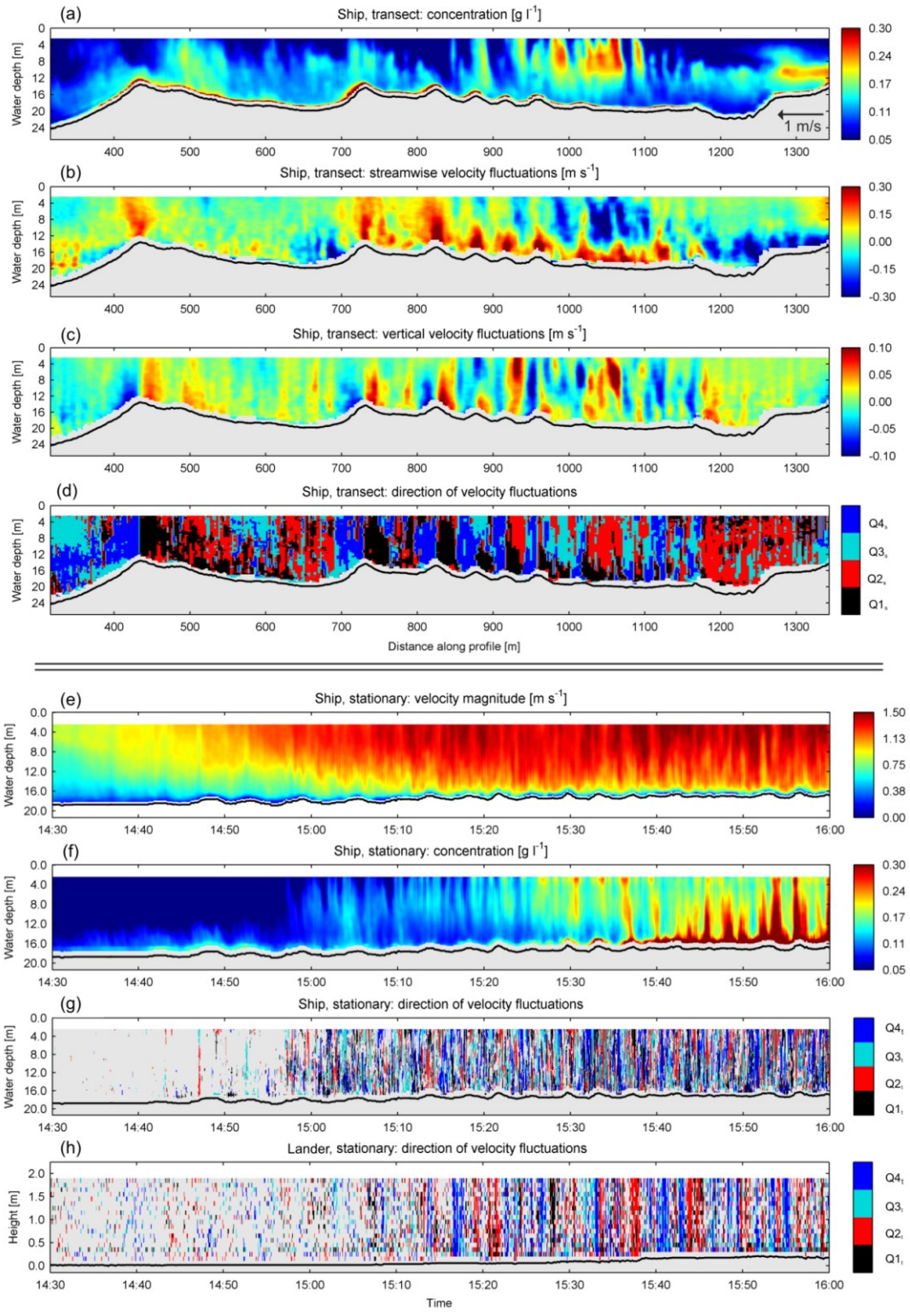

Figure 2.5. Longitudinal transect across bedforms: (a) Suspension clouds are clearly distinguished by increased SSC values over the profile forming columnar structures. (b) Streamwise velocity fluctuations [m s^{-1}] show accelerated flow over the bedform stoss and crest and flow deceleration in the bedform lee. (c) Vertical velocity fluctuations [m s^{-1}] indicate upward velocity over the stoss-side and crest and downward flow in the bedform lee. (d) Coupled $Q2_s$ /$Q3_s$ events are associated with the clouds. Stationary measurements by ship-borne ADCP (e-g) and lander ADCP (h): (e, f) Increased SSC in columnar structures around 15:00 UTC coinciding with near-bed velocities of 0.6 m s^{-1}. (g) Directional fluctuation analysis: velocity fluctuations reach above threshold and alternating common velocity signatures occupy the entire water column. (h) Near-bed measurements show alternations of $Q2_t$ and $Q4_t$ events above threshold to be most common. For more explanation see text.

2.6. Discussion

The observed compound tidal bedforms exert similar spatial control on the flow and on suspended sediment transport patterns as previously observed in laboratory studies [e.g., *McLean et al.*, 1994; *Bennett and Best*, 1995; *Venditti and Bennett*, 2000] and field measurements of bedforms under uni-directional currents [c.f., review by *Best*, 2005b]. The frequent changes in flow velocity and direction associated with the tides however, induce a temporal variability that is much more complex and significantly affects sediment transport in such environments [*Lefebvre et al.*, 2011]. In our efforts to create accurate predictors of suspended sediment transport for application in inlet maintenance strategies, this study on the intermittency of suspended sediment transport and the associated turbulent flow field contributes to our current knowledge on estuarine morphodynamics. The following will provide a discussion on the origin of the suspension clouds in the Elbe River, the reasons behind their restricted occurrence on a tidal cycle and the processes maintaining the clouds in the upper water column in the light of previous studies.

2.6.1. The origin of the suspension clouds

Frequency estimates of turbidity clouds and flow structures

Flow passing over a fluid body, which is restrained in its motion, tends to oscillate at a specific frequency causing the generation of turbulent structures with equal periodicity [*Levi*, 1983, *Kostaschuk and Church*, 1993, *Babakaiff and Hickin*, 1996]. It relates the specific frequency of turbulent production (*f)* to a characteristic length scale (*l)* and a characteristic velocity (*U*) by the Strouhal Number (*Sr = f l /U)* [*Strouhal*, 1878, *Levi*, 1983]. Depending on the seabed relief and scales of turbulence observed, several variations of the law have been proposed differing in length and velocity scales, i.e., flow depth scale or bedform scale. The characteristic velocity has been substituted e.g., by the free shear velocity, mean flow velocity or shear velocity, while the length scale has been defined as flow depth, separation zone length, or bedform height [e.g., *Rao et al.*, 1971, *Itakura and Kishi*, 1980, *Simpson*, 1989, *Kostaschuk and Church*, 1993, *Driver et al.*, 1987]. Venditti & Bauer [2005] summarized observed eddy frequencies in the lee-side of bedforms from field or laboratory measurements (authors cited therein) to derive a range of Strouhal Numbers characteristic for both flow depth scale and bedform scale. Accordingly, Strouhal Numbers based on mean flow velocity (U_b) and mean water depth (*h*) ranged between 0.19 - 0.6. Scaling mean flow velocity (U_b) and mean dune height (*H)* provided values between 0.05 - 0.25.

Turbulent structures specifically associated with flow separation are, characterized by distinct frequencies: Simpson [1989] proposed two scale relationships based on laboratory observations in order to differentiate contributions of macroturbulent phenomena associated with eddy

shedding ($f_v = 0.8\ U_0/x_r$) from wake flapping ($f_w < 0.1\ U_0/x_r$), where U_0 is the mean velocity upstream of the step and x_r is the mean length of the separation zone (e.g., $x_r = 4.25\ H$ [*Bennett and Best*, 1995]).

Application of the relations to the Elbe environment (h = 16.6 m, H = 3 m, $U_0 = U_b$ = 1.22 m s^{-1}) adopting the range of Strouhal Numbers proposed by Venditti and Bauer [2005] provides an expected frequency range of 0.013 - 0.04 Hz (scaled with water depth and mean velocity) and 0.019 - 0.09 Hz (scaled with bedform height and mean velocity) for macroturbulent structures in the Elbe River. The predicted frequencies for macroturbulence specifically associated with eddy shedding and wake flapping are f_v = 0.07 Hz and f_w < 0.009 Hz, respectively.

Near-bed detection of common velocity signatures in this study indicated that coherent flow structures capable of suspending sediment occur with a frequency of 0.007 – 0.017 Hz. A visual estimate of suspension cloud periodicity based on surface measurements of SSC on June 23rd yielded 30 – 200 s, with an average value of 69 s (0.014 Hz). Despite this rather crude estimation, the observed frequencies of both clouds and flow structures in the Elbe environment agree with predicted frequencies, if at the lower end, based on previously observed Strouhal Numbers. This indicates that surface clouds and associated boils originate from similar turbulent processes as described in previous studies. It is however due to measurement limitations, not possible to relate the occurrence of clouds to a particular turbulence-producing mechanism associated with the formation of a flow recirculation cell.

Observations in the field

The turbidity clouds in the upper water column are associated with an alternating pattern of up- and downward directed decelerating flow as revealed by observations of spatial SSC and flow structures. A similar velocity signature can be found in the bedform lee and trough, indicating the origin of the clouds at this location in the field of bedforms. Several studies have attributed boil producing vertical fluid motions to originate in the lee of bedforms related to separation of the flow [e.g., *Lapointe*, 1992, *Nezu and Nakagawa*, 1993, *Bennett and Best*, 1995, *Venditti and Bennett*, 2000, *Venditti and Bauer*, 2005]. In a laboratory analysis of turbulence structure and sediment transport over dunes, Bennett and Best [1995] found accelerated upward motions (Q2 events) along the separation zone layer and near flow reattachment. They attributed sediment entrainment and suspension in boils to the more energetic of these events. Decelerated downward motions were confined to the reattachment point, while inrushes of accelerated downward flow (Q4 events) were coupled with the sediment entraining upward fluid motions above the dune troughs. In the field, Shugar et al., [2010] correlated high SSC structures with near-bed areas of streamwise velocity deceleration over the crests and troughs of a large fluvial sand dune. The structures were inversely correlated with vertical velocities and linked to the vertical flux of fluid to the water surface.

Although the observed velocity characteristics associated with the turbidity clouds are similar, it cannot be determined in this study whether the low-velocity vortices associated with the Elbe turbidity clouds form due to flow separation processes. ADCP velocity measurements do not show any evidence of flow reversal in the lee of the large compound tidal bedforms. Lee-side angles of 10 – 15° fall in the range of angles for which it is still debated whether permanent flow reversal occurs in the field. Kostaschuk and Villard [1996b] suggested that flow separation may occur intermittently only for lee-side slopes of up to 19° while Paarlberg et al. [2009] observed permanent flow separation for laboratory dunes with lee angles >10°. The failure of detection might therefore be due to the ADCP's methodological limitation of measuring in the near bed bedform troughs [*Kostaschuk et al.*, 2005] or the absence of permanent flow separation. In the absence of permanent flow separation similar macroturbulent flow structures have been observed in the deceleration zone behind the crests of low angle dunes [*Kostaschuk and Villard*, 1999, *Best et al.*, 2001, *Best and Kostaschuk*, 2002]. Regardless of the formation, it is these upward motions that entrain material from the bedform troughs. The sediment is suspended and advected upward confined in the vertical flow structures. The observation of lower temperature and higher salinity, therefore higher density, of fluid within the clouds, indicating the origin of the water masses close to the seabed, support this conclusion. Further indications are the periodic existence of a fluid mud layer in the bedform troughs, the linked grain size distributions of the fluid mud and suspended sediment, and the similar nature of coherent structures in the bedform troughs and within the suspension clouds.

2.6.2. Hydrodynamic threshold for the occurrence of suspension clouds

The occurrence of turbidity clouds at the water surface of the Elbe is restricted to certain tidal stages exhibiting strong velocity gradients. Similarly, Matthes [1947] and Kostaschuk and Church [1993] observed a restriction of boils to rapid flow stages in fluvial environments. Rood and Hickin [1989] attributed the evidence of larger macroturbulence at the water surface to higher turbulent stresses during decelerating flows. Near-bed observations of turbulent structure under tidal flows in the laboratory [*Anwar*, 1981] and field [*Gordon*, 1975] had indicated that the accelerating and predominately the decelerating phase of the tide were characterized by higher turbulent intensities and enhanced sediment transport compared to maximum flow velocities. The constriction of the Elbe clouds to the accelerating stage of the tide is thus believed to be result of higher turbulence due to flow un-steadiness. Following maximum flow velocity, the now almost homogenous sediment mixture in the water column and the absence of significant amounts of fine material on the seabed is believed to prohibit any distinction of increased suspension during flow deceleration.

While coherent flow structures exist early during the tidal cycle, it requires a mean near-bed velocity of 0.6 m s^{-1} before sediment is brought into suspension by these structures. The strongest velocity fluctuations around this time are associated with the decelerated upward (Q2 type) and accelerated downward (Q4 type) flow structures providing the necessary turbulent shear stress to entrain sediment and to sustain material in suspension.

2.6.3. Suspension cloud sustainment in the water column

ADCP records and visual observations show the persistence of the suspended sediment and coherent flow structures. The advected confined shapes at the water surface sustain for up to 1 hour, a considerably longer period than previously reported [e.g., *Rood and Hickin*, 1989; *Babakaiff and Hickin*, 1996]. To our knowledge, it has also never been reported that suspension clouds associated with boils over dunes occupy much of the water colum (~8 m) with little inhomogeneity of SSC. In contrast, Shugar et al. [2010] observed a loss of energy and lateral spread as flow structures migrate upwards through the water column due to the increased velocity in the upper flow region and induced shear dispersion. Suspension and coherent flow structures have also been reported to show distinct advection angles of 20 – 25° [*Nezu and Nakagawa*, 1993, *Kostaschuk and Villard*, 1999, *Kostaschuk*, 2000], which were much less inclined in this study.

These deviations from previous descriptions are attributed to the well-mixed water column of the Elbe and the difference in transported matter entrained in such boils. Previous studies documented the ability of boils in entraining sandy material, whereas in this study, even under maximum flow conditions the grain size in suspension remains predominately in the mud-silt spectrum. Higher settling velocities in case of sandy material will lead to a faster deposition and fall-out from the confined fluid motion [*Matthes*, 1947]. Rood and Hickin [1989] observed the grain size distribution of sediment within boils to depend on the tidal stage and thus turbulent energy in the flow structures. In this study, at no point do we see changes in the grain size distribution of sediment in the water column. The sandy material of the compound bedforms is believed to be transported predominately as bedload transport. These findings suggest that the environment of the Elbe compound tidal bedforms is characterized by two apparently decoupled sedimentary regimes: grains smaller than 170 µm (main mode of about 50 µm) are transported predominately in suspension and form a fluid mud layer around slack water in the tidal bedform troughs. The active tidal bedforms on the seabed are composed of sand larger than 170 µm (main modes at 350 and 500 µm). The suspended fine sediment is believed to travel up to several kilometers within the coherent flow structures. It is the large compound tidal bedforms, themselves products of the interaction of flow and coarser sediment that provide the mechanisms and controls on the fine sediment budget of the Elbe.

2.7. Conclusion

The mobile bed sediment of the Elbe estuary can be regarded as a dynamic two component system: one component consists of the sandy bed material (~500 µm) which, under the influence of tidal currents, river discharge and macroturbulence, forms the ebb-directed primary and smaller secondary bedforms in focus in this study. The second component is made out of fine material (~50 µm) which, under the influence of tidal currents, periodically settles towards the ground to form a fluid mud layer in the bedform troughs or is transported in suspension in the form of distinct clouds.

This study made use of hydro-acoustic and optical measuring techniques to gain insights into the governing processes involved in the cyclic transport behavior of this latter component. Although ADCP measurements due to sensor configuration and resolution achievable are somewhat limited [c.f., *Kostaschuk et al*., 2005], general patterns of macroturbulence associated with the clouds can be observed. In order to derive a more detailed view on the origin of tidal bedform-related turbulence and turbulent motions associated with the suspension clouds long after their formation however, high frequency measurements of simultaneous 3D velocity and SSC fluctuations are necessary.

The following provides a conceptual model of the governing processes:

- Suspended sediment in the water column is at its minimum ca. one hour after slack water. Formerly suspended sediment has settled and accumulated in form of a fluid mud layer in the bedform troughs.

- As the tidal currents accelerate, the flow over the bedforms is altered to characteristic flow patterns controlled by topography: flow acceleration above the stoss-side and deceleration in the dune lee. Coherent structures evolve with distinguishable patterns of upwelling and downwelling fluid motions. Alternating low-velocity upward and downward structures at the troughs entrain fine material and transport the clouds into the upper water column, once a turbulent energetic threshold is overcome.

- Low-velocity up- and downwelling fluid motions maintain suspended sediments in a confined structure and induce an upward directed momentum, resulting in suspended sediments and water of higher-density to be transported towards the water surface. The low-velocity fluid motions persist and maintain the clouds at the water surface.

- As the tidal flow accelerates the clouds disperse and then merge to form a homogenous suspended sediment distribution.

- After slack water, the suspended fine sediments settle and form the fluid mud layer, as observed in the bedform troughs.

Acknowledgements

We acknowledge the comments of an anonymous reviewer and editor on an earlier stage of the manuscript. We thank the captain and crew of FK Senckenberg and the research institute Senckenberg am Meer for the ship time provided. Thanks are extended to Christian Maushake and Dierk Sellhorn from Bundesanstalt für Wasserbau (BAW) for technical support during the field survey. Inka Meyer performed the PSD analysis. Markus Benninghoff helped with the preparation of the sediment samples. This research was funded through the DFG-Research Center/Cluster of Excellence „The Ocean in the Earth System“.

WITH OR AGAINST THE TIDE:

THE INFLUENCE OF BEDFORM ASYMMETRY ON THE FORMATION OF MACROTURBULENCE AND SUSPENDED SEDIMENT PATTERNS

Eva Kwoll[1], Marius Becker[1] and Christian Winter[1],

[1] MARUM-Center for Marine Environmental Sciences, University of Bremen, Germany

Manuscript under review for publication in *Water Resources Research*

ABSTRACT

This study examines the formation and dynamics of suspended sediment patterns coupled to mean flow and turbulence in the Danish Knudedyb tidal inlet. At this location, very large primary bedforms remain ebb-oriented during a tidal cycle while smaller superimposed bedforms reverse direction with each tidal phase. Thus, primary bedforms are aligned with the flow during one tidal phase and opposed in the other. Hydro-acoustic in-situ observations show pronounced differences in suspended sediment transport patterns between tidal phases. When flow and primary bedform orientation are aligned, water-depth-scale macroturbulence develops along the flow separation zones, governing sediment suspension and transport. Flow separation and macroturbulence associated with the primary bedforms are absent when flow and bedform orientation are opposed. Then, suspended sediment transport is governed by turbulence arising from the superimposed secondary bedforms. Transport capabilities are limited by the steep flow-facing flank and the adverse pressure gradient of the downstream hydraulic lee-side.

3.1. Introduction

Flow transverse, sub-aqueous bedforms develop through the interaction of the hydrodynamic forcing with the mobile sandy bed. Although studied intensively, several morphodynamic processes associated with the mutual adjustment of bedform morphology, the flow structure and sediment transport remain unclear [c.f., reviews by *Best*, 2005b; *Parsons and Best*, 2013; *Venditti*, 2013]. This is attributable to the complex and variable physical settings in which bedforms occur in fluvial or coastal environments.

Sediment transport and resulting morphological adaptations are governed by turbulence arising from the interaction of the fluid phase with the sediment grains and the bedform-induced form roughness. The morphological adaptation of bedforms often lags behind changes in fluid forcing if flow changes at timescales smaller than required for equilibrium adaptation [*Kostaschuk and Best*, 2005; *Martin and Jerolmack*, 2013]. A prominent example of such morphological hysteresis is found in coastal settings: bedforms are often of asymmetric shape with a quasi-stable orientation towards a dominant direction, despite the presence of continuously reversing tidal currents [e.g., *Ernstsen et al.*, 2006; *Lefebvre et al.*, 2011]. This implies that the orientation of bedforms and tidal currents are opposed for a great proportion of the tidal cycle.

Previous research has mainly focused on asymmetric, angle-of-repose bedforms classified as dunes or ripples [*Ashley*, 1990] aligned with steady, uni-directional flows [*Best*, 2005b; *Coleman and Nikora*, 2011; *Venditti*, 2013 and references therein]. More recently, low-angle, symmetric dunes have received increasing attention [e.g., *Best et al.*, 2001; *Best and Kostaschuk*, 2002; *Kostaschuk et al.*, 2009]. In the uni-directional case, topographically-induced pressure variations result in the following time-averaged flow features: flow separation occurs at the crest in the presence of a strong adverse pressure gradient. The separated shear layer reattaches 4 - 6 bedform heights (H) [*Venditti*, 2013] downstream and an internal boundary layer develops with increasing vertical extent towards the next crest. Flow in the immediate lee bordered by the separated shear layer is highly turbulent with periodic flow reversal and an associated wake region extending from the point of separation downstream towards the next crest. Wake region and internal boundary layer interact. Above symmetric, low-angle dunes flow separation occurs intermittent only or is absent in which case the bedform lee is characterized by a decelerating wall-bound shear layer.

Turbulence production within the flow separation zone dominates over boundary layer turbulence [*Nelson et al.*, 1993], and is organized into coherent flow structures that are observed throughout the entire water depth [e.g., *Kostaschuk and Church*, 1993; *Nezu and Nakagawa*, 1993; *Best*, 2005a]. Detailed laboratory investigations and numerical studies on the origin and topology of these macroturbulent structures have shown that there is a topological difference

between vortices originating in the separated shear layer and vortices observed at or downstream of reattachment [*Kadota and Nezu*, 1999; *Stoesser et al.*, 2008; *Omidyeganeh and Piomelli*, 2011; *Chang and Constantinescu*, 2013]. At any time the separated shear layer consists of spanwise vortices, referred to as roller structures or vortex tubes that are formed at the point of separation and along the shear layer due to Kelvin-Helmholtz instabilities. Rollers follow a path along the shear layer but periodic excursions into the inner separation zone or outer flow region associated with 'flapping' of the shear layer have been observed [*Simpson*, 1989; *Schmeeckle et al.*, 1999]. These low-frequency events and the upward propagation of rollers are one of the mechanisms proposed for the frequent occurrence of boils at the water surface downstream of bedform crests [*Bennett and Best*, 1995; *Babakaiff and Hickin*, 1996; *Venditti and Bennett*, 2000; *Grigoriadis et al.*, 2009; *Omidyeganeh and Piomelli*, 2011]. Other studies suggest that boils originate from hairpin-shaped streamwise oriented vortices developing downstream of the reattachment point [*Nezu and Nakagawa*, 1993; *Best*, 2005a; *Stoesser et al.*, 2008; *Chang and Constantinescu*, 2013]. However, the exact mechanisms behind this vortex transformation from the separation zone to reattachment are still being discussed [*Stoesser et al.*, 2008; *Chang and Constantinescu*, 2013]. In the absence of a separated shear layer over low-angle dunes, macroturbulence production has been attributed to Kelvin-Helmholtz type instabilities occurring due to high velocity gradients in the deceleration zone or intermittent flow separation [*Best and Kostaschuk*, 2002].

Macroturbulence above bedforms has received considerable attention for two reasons: Firstly, the production of turbulence has important effects on hydraulic roughness [*Grant and Madsen*, 1982; *Lefebvre et al.*, 2013a]. Secondly, though not unrelated, studies showed that sediment entrainment and transport in suspension above bedforms is governed by these macroturbulent structures [*Kostaschuk and Church*, 1993; Lapointe, 1992; *Kostaschuk and Villard*, 1996; *Shugar et al.*, 2010; *Kwoll et al.*, *2013*]. Sediment–laden streamwise vortices arising from the zone of reattachment are commonly referred to as kolks [sensu *Matthes*, 1947]. Several studies have shown however, that spanwise-vortices arising from the shear layer might be a preferable mechanism to entrain sediments that surpassed the crest near the bed into the water column [*Kostaschuk and Villard*, 1999; *Schmeeckle et al.*, 1999].

Understanding the occurrence and generation of such macroturbulent structures and associated suspended sediment transport is essential for a process-based understanding and prediction of overall sedimentary budgets in environments where bedforms are present. The present study examines macroturbulence and suspended sediment concentration (SSC) variability above asymmetric bedforms aligned with or against the tide based on in-situ data. We present detailed time-averaged flow characteristics for each tidal phase derived through repetitive ship-borne

ADCP transects. We focus on the instantaneous flow field, examining the scale, inferred origin and linkage to sediment suspension of macroturbulent structures.

3.2. Study area

The Wadden Sea comprises several tidal basins located along the Dutch, German and Danish coastline, separated from the adjacent North Sea by groups of barrier islands and spits. The exchange of North Sea waters with the basins is confined to the tidal inlets between the barriers. In a broad sense, the inlets consist of a deeper channel and shoals associated with ebb and flood tidal deltas, swash bars and other smaller scale sedimentary features. Here one of these inlets, the Knudedyb, located in the Danish part of the Wadden Sea was chosen as a study site (**Figure 3.1**). In this sheltered environment, strong semi-diurnal tidal currents are the primary hydrodynamic forcing on the sandy seabed.

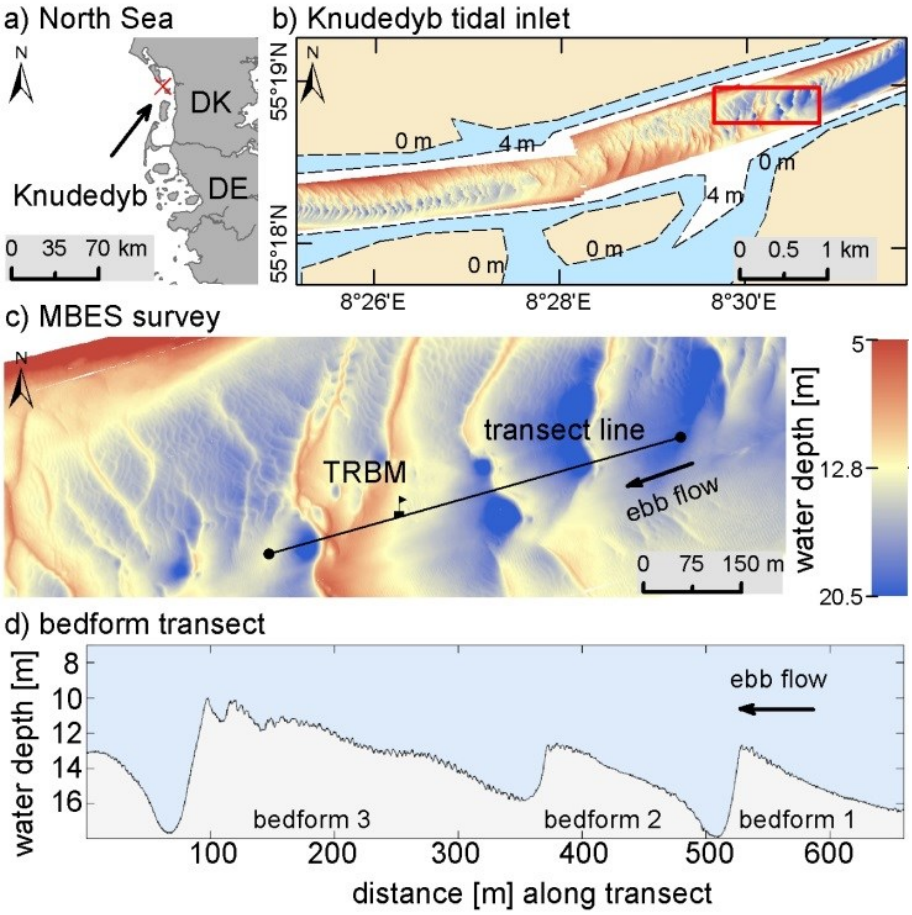

Figure 3.1. The study site in the Knudedyb tidal inlet in the Danish Wadden Sea (a). (b) The channel is 8.5 km long and 1 km wide. (c + d) Primary bedforms are ebb-oriented and superimposed by smaller secondary bedforms. Ship transect and location of the TRBM ADCP are indicated in (c).

The inlet channel is 8.5 km long and 1 km wide and covered by large to very large asymmetric compound bedforms previously observed by Lefebvre et al. [2013a]. Compound bedforms in

the central channel are made up of sediments with mean values of 0.3 – 0.7 mm [*Svenson et al.*, 2009] and vary in height between 3 – 8 m and lengths of 150 – 290 m. The primary bedforms are permanently oriented in the dominating ebb current direction with a gentle, long slope (~2°) facing the ebb flow (hereafter referred to as the bedform stoss-side) and a short, steep slope (16 - 20°) directed away from the ebb flow (hereafter referred to as the bedform lee-side). Smaller secondary bedforms are superimposed on the primary bedforms (heights 0.15 – 0.3 m; lengths 3 – 6 m) and reverse direction with each phase. A detailed morphological study by Ernstsen et al. [2006] addresses a tidal inlet of very similar setting ~15 km north of Knudedyb and will be used as a reference for morphological adaptation of the compound bedform field on the time-scale of a tidal cycle.

3.3. Data collection and analysis

3.3.1. Field campaign

A field campaign was launched in November 2008 carrying out repetitive shipborne longitudinal transects across three compound bedforms in the tidal channel area (transect line in **Figure 3.1c**). The 620 m long transects were navigated during one flood/ebb cycle, resulting in a total number of 27 longitudinal transects. Transects took on average 10 min to complete and were navigated against the tidal current direction (average vessel speed of 1.25 m s^{-1}). A downward-looking acoustic Doppler current profiler (ADCP; 1200 kHz, TRDI workhorse) was mounted on the ship to monitor profiles of the flow velocity and acoustic backscatter, geo-referenced by the onboard LRK GPS. ADCP flow velocities were corrected for vessel speed by ADCP bottom tracking. The ping rate of the ship-borne ADCP was set to 2.4 s, with a vertical bin size of 0.5 m. Considering deployment depth and blanking distance, the first measurement was located in a depth of 2.93 m. Simultaneously, an upward-looking ADCP (600 kHz, TRDI workhorse) was installed on the mid-stoss of the largest compound bedform (bedform 3) for three tidal cycles in a trawl-resistant, bottom-mounted (TRBM) frame (Location in **Figure 3.1c**). The lowest reading of the TRBM ADCP was located 1.57 m above the seabed. Ping rate and bin size were 1 s and 0.25 m, respectively.

3.3.2. Acoustic backscatter calibration

At varying water depths, 89 water samples were collected with a pump system and subsequently filtered, dried and weighed to derive suspended sediment concentration (SSC). ADCP backscatter signal was calibrated applying the method of Gartner [2004]. Following Deines [1999], echo intensities recorded by the ADCP were corrected for beam spreading and water absorption. The water absorption coefficient was calculated according to Ainslie and McColm [1998]. The backscatter intensity was further corrected for absorption due to suspended sediment, implementing the iterative algorithm described by Thorne et al. [1994] and applied,

by Holdaway et al. [1999] on single-frequency hydro-acoustic data. The sediment absorption coefficient was determined according to Urick [1948].

3.3.3. STATIONARY TRBM ADCP

Three-dimensional velocity data were extracted from the TRBM ADCP and rotated to derive streamwise (*u)* and spanwise (*v)* velocity component in respect to the main tidal current direction during each tidal phase.

Fluctuations of streamwise velocity (u_t*')* and vertical velocity (w_t*')* were derived by subtracting a 10 min time-average [*Soulsby*, 1980; *Dyer*, 1997] from the instantaneous values along equal depth bins:

$$x'_t = x_t - \bar{x}_t, \quad (3.1)$$

with

$$\bar{x}_t = I^{-1} \sum_{i=1}^{I} x_i \quad (3.2)$$

where ($I = 600$) is the number of ensembles and (x) may be substituted by either quantity (u) and (w). The suffix (t) and horizontal overbar hereafter denote time-averaging.

Conditional sorting of velocity data into four quadrants making up the streamwise and vertical velocity (Quadrant analysis) [*Lu and Willmarth*, 1973] has traditionally been applied for analysis of the origin and dynamics of microturbulent coherent flow structures such as occurring in turbulent boundary layers [*Antonia*, 1981; *Adrian*, 2007]. Recently, quadrant analysis has been increasingly applied for velocity measurements with much coarser resolution spanning the entire water column [*Bradley*, 2012; *Kwoll et al.*, *2013*]. In these applications, a coherent flow structure is no longer defined as a single strong velocity excursion but rather as a temporal cluster of velocity measurements characterized by fluid motion of the same quadrant. In this study, quadrant analysis was applied to the velocity fluctuations derived in Equation (4.1) classifying into: $Q1_t$ ($u'_t>0$, $w'_t>0$), $Q2_t$ ($u'_t<0$, $w'_t>0$), $Q3_t$ ($u'_t<0$, $w'_t<0$) and $Q4_t$ ($u'_t>0$, $w'_t<0$).

Pattern identification in suspended sediment

Patterns in SSC profiles with significantly higher than average SSC were identified as follows: Firstly, a time series of SSC fluctuations (c'_t) was determined analogue to velocity fluctuations in Equation (4.1) and (4.2). Adjacent measurements in the vertical and temporal of (c'_t) above a threshold were identified and grouped. Different thresholds were applied for the ebb ($c'_t >$ 0.0027 g L^{-1}) and flood phase ($c'_t >$ 0.0017 g L^{-1}), based on the standard deviation of (c'_t) during each phase. In order to remove small fluctuations and single events, all structures containing less than 50 ADCP bins were discarded. Hereafter, we will refer to patterns identified via this algorithm as suspension structures. The horizontal extent of a suspension structure was defined as the product of the depth-averaged current velocity and the duration, during which the structure was observed. The frequency of recurrence was determined from the time lag between two successive structures.

Ship-based ADCP transects

13 ship-based ADCP transects were collected during the flood and 14 during the ebb period in intervals of approximately 30 min. The velocity data were corrected for pitch and roll, orthogonally projected onto a single transect line and rotated so that the streamwise velocity component was aligned with the main flow direction in each tidal phase. Flow velocity and SSC profiles were interpolated onto a regular grid with a vertical resolution of 0.25 m (the bin size)

and 1 m in the horizontal. The profiles were then analyzed as transect-average of each phase or single instantaneous measurements.

Temporally averaged flow fields above the bedforms for each tidal phase were derived by averaging the corresponding transects at each grid point:

$$\tilde{x} = N^{-1} \sum_{n=1}^{N} x_n \,, \qquad (3.3)$$

where (*N)* is the number of transects during the flood ($N = 13$) and during the ebb ($N = 14$). (*x)* may be substituted by either quantity (*u)*, (*w)* or *(c);* the tilde hereafter refers to transect-averaged values.

Deviations of the streamwise velocity from a spatial mean in single transects and the transect-average were determined:

$$x'_s = x_s - \langle x_s \rangle \quad (3.4)$$

where

$$\langle x_s \rangle = S^{-1} \sum_{s=1}^{S} x_s \,, \quad (3.5)$$

is the spatial mean along equal heights above the seabed normalized by the total water depth, which is considered to be an approximation of mean flow streamlines. (S) is the number of ensembles in each transect (S = 619) and (x) is substitutable by (u), (w), (c), ($\tilde{u}$), ($\tilde{w}$) and ($\tilde{c}$). Suffix (s) hereafter denotes averaging in space.

Quadrant maps were prepared subjecting streamwise and vertical velocity deviations to quadrant analysis [*Bradley*, 2012; *Kwoll et al.*, *2013*]: ($Q1_s$ ($u'_s>0$, $w'_s>0$), $Q2_s$ ($u'_s<0$, $w'_s>0$), $Q3_s$ ($u'_s<0$, $w'_s<0$) and $Q4_s$ ($u'_s>0$, $w'_s<0$)). Spatial quadrant maps thus depict coherent flow deviations above the observed bedform field distinguishable from the ambient flow field.

3.4. Results

The semi-diurnal tidal variability in water level, flow and suspended sediment concentration (SSC) with characteristic asymmetries between flood and ebb are shown based on depth-averaged TRBM ADCP data and depth-averaged ship ADCP measurements of each transect (**Figure 3.2**). Flow is towards the WSW during the ebb phase (duration 6.6 h) reaching magnitudes of up to 1.5 m s^{-1} while weaker currents with maximum velocities around 1 m s^{-1} towards the NEE prevail during the flood (duration 6 h) . Depth-averaged SSC is smallest (0.04 g L^{-1}) at flood slack water and generally follows the tidal current velocity, with maximum values of 0.15 g L^{-1} at the time of maximum ebb current velocity. SSC at ebb slack water does not fall below 0.07 g L^{-1}. Maximum concentrations during the flood reach up to 0.08 g L^{-1}.

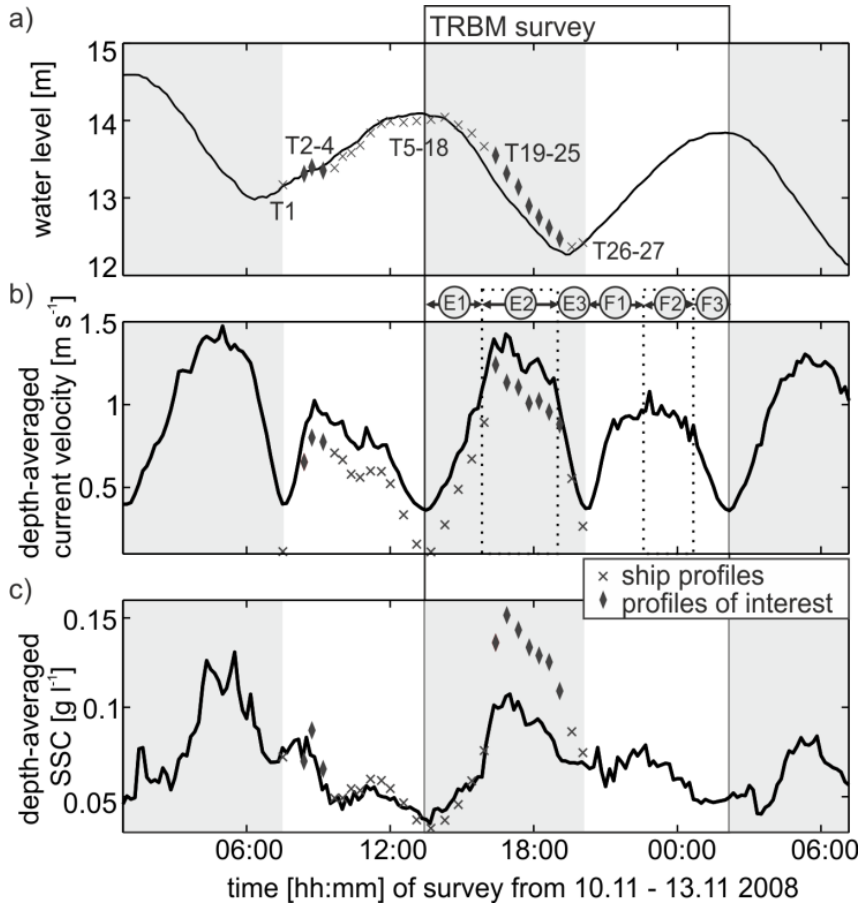

Figure 3.2. Tidal characteristics at the survey site during the measuring period from TRBM ADCP. (a) Water level [m], (b) depth-averaged current velocity [m s^{-1}] and (c) depth-averaged SSC [g L^{-1}] for two tidal cycles. The grey box indicates the period of the TRBM survey analyzed; grey shadings differentiate ebb tidal stages. Times of ship profiles are indicated (x); selected profiles shown below are indicated by diamonds.

3.4.1. Transect-averaged flow field

The transect-averaged velocity magnitude ($U = (\tilde{u}^2 + \tilde{w}^2)^{0.5}$) during the ebb reveals the topographically forced flow acceleration above the bedform stoss-sides (horizontal extent of

100 - 230 m) and flow expansion and deceleration in the steep bedform lee (extents of 25 – 40 m) (**Figure 3.3a**). Regarding velocity components, **Figure 3.3b** displays the deviation of the streamwise velocity component from the spatially-averaged velocity profile ($\tilde{u}'_s$). The greatest magnitudes of deviations occur above the bedform lee-sides and are associated with decelerated flow. Negative streamwise velocities are detected downstream of bedform 3 along 40% of the lee-side at most 3.5 m above the bed. Average streamwise velocity magnitude of these measurements is -0.08 m s^{-1} (7% of maximum streamwise velocity). Spatial deviations of the vertical velocity component ($\tilde{w}'_s$) display downward directed flow in the bedform lee-side and overall upward directed flow above the bedform stoss (**Figure 3.3c**). Again, deviations from the spatially-averaged profile are largest in the bedform lee. The greatest magnitude of upward flow is located just upstream of the crest and in localized areas along the stoss-side.

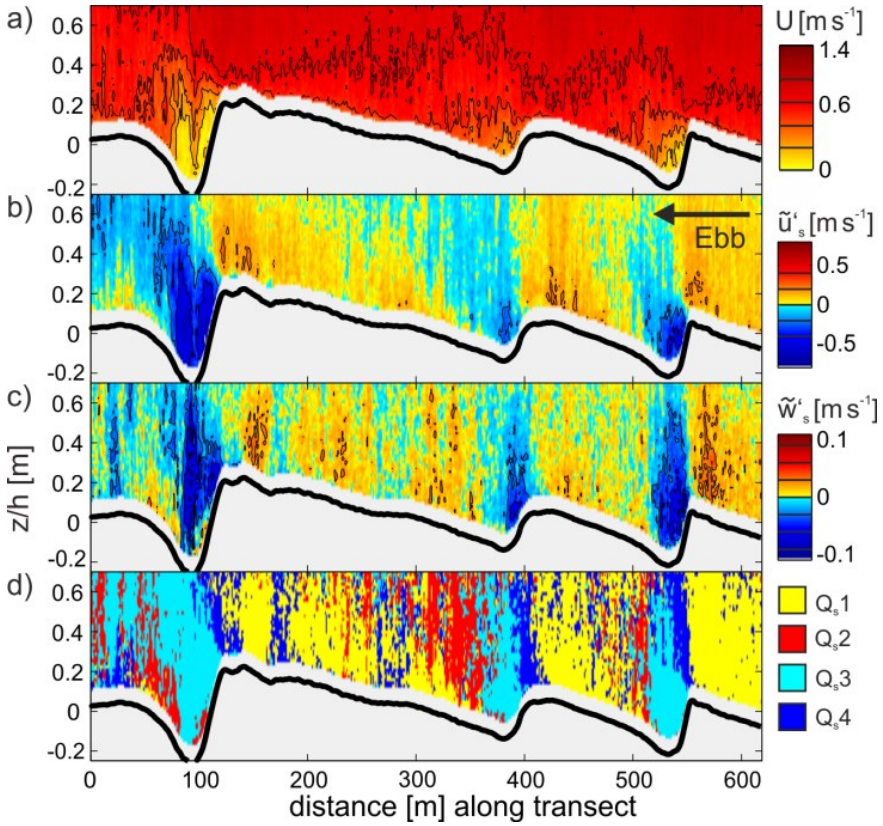

Figure 3.3. Transect-averaged flow field characteristics during the ebb phase. (a) Velocity magnitude U [m s^{-1}], (b) streamwise velocity deviation $\tilde{u}'_s$ [m s^{-1}], (c) vertical velocity deviation $\tilde{w}'_s$[m s^{-1}], (d) quadrant distribution based on vertical and streamwise velocity deviation.

Hereafter, directional trends in average fluid motion derived through quadrant analysis are referred to as quadrants. Quadrant maps of transect-averaged velocity components are depicted in **Figure 3.3d**. Flow above the bedform mid-stoss to the crest is characterized by mostly accelerated upward flow ($Q1_s$) with interspersed downward flow ($Q4_s$). At the crest a transition occurs from $Q4_s$ to decelerated downward flow ($Q3_s$), which characterizes the entire lee-side and trough. Above the lower stoss, decelerated upward flow ($Q2_s$) dominates. Further

downstream flow patterns are highly variable, result from one transect to the next and little stationary conformance.

During the flood phase (**Figure 3.4a**), topographic forcing induces rapid flow acceleration over the short, steep bedform lee-side and moderate deceleration over the gentle-sloping bedform stoss. The calculated deviations ($\tilde{u}'_s$) from the spatially-averaged profile of streamwise velocity (**Figure 3.4b**) differ only minor from the pattern described during the ebb. No flow reversal is observed during the flood. Decelerated flow occurs over the lower stoss-side/trough towards the crest. Accelerated flow occurs from the crest towards the mid-stoss. Highest magnitudes of deviations are associated with the faster-than-average flow above the crest. Flow is upward above the bedform lee-sides (**Figure 3.4c**) and mostly downward with occasional upward flow above the bedform stoss-sides. Greatest magnitude of deviation ($\tilde{w}'_s$) is associated with the upward flow above the bedform lee.

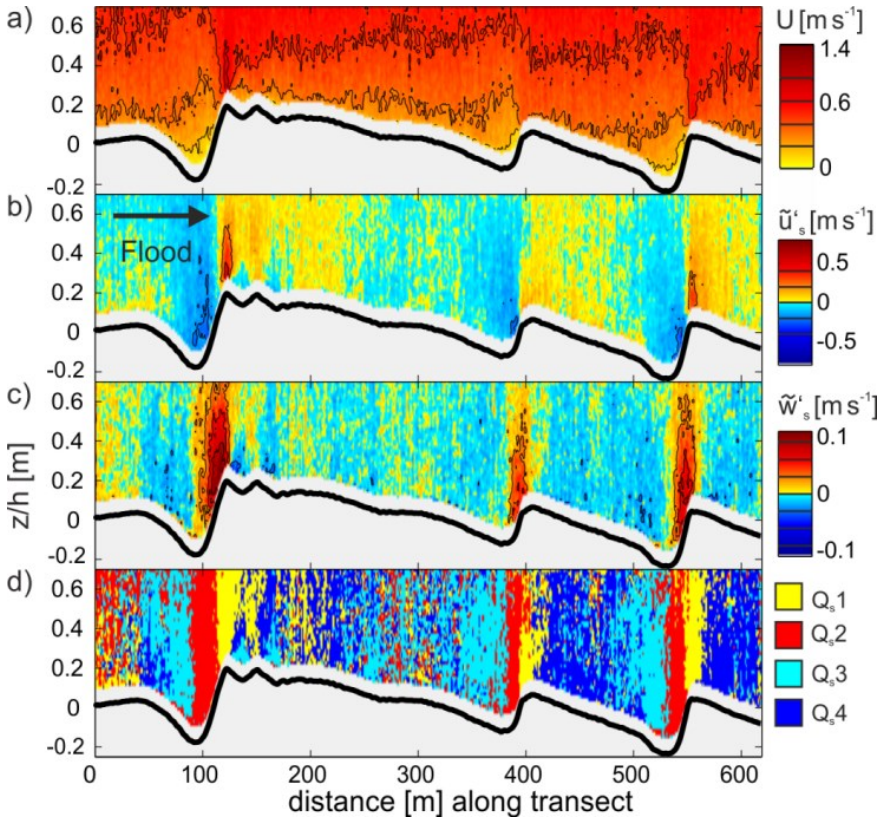

Figure 3.4. Transect-averaged flow field characteristics during the flood phase. (a) Velocity magnitude U [m s^{-1}], (b) streamwise velocity deviation $\tilde{u}'_s$ [m s^{-1}], (c) vertical velocity deviation $\tilde{w}'_s$[m s-1], (d) quadrant distribution based on vertical and streamwise velocity.

Since streamwise deviations are similar for the ebb and flood, quadrant variability is mainly controlled by the vertical velocity component. The flood quadrant map is depicted in **Figure 3.4d**. The upper bedform stoss-side is characterized by alternating patterns of accelerated up- and downward flow ($Q1_s$ and $Q4_s$) that transitions into decelerated downward flow ($Q3_s$) above

the lower stoss downstream towards the trough. Decelerated upward flow ($Q2_s$) dominates the steep bedform lee-side.

3.4.2. Transect-averaged SSC distribution

Transect-averaged suspended sediment concentrations ($\tilde{c}$) for the ebb phase are shown in **Figure 3.5a**. Generally, SSCs decrease with height above the bed. The highest near-bed concentrations are observed above the bedform crests, lee-sides and troughs. Sediment concentrations higher in the water column vary in the order of 0.03 g L^{-1} depending on the location in the bedform field; sediment concentrations increase in ebb flow direction along the stoss-side toward the crest.

Local horizontal (q_u) and vertical sediment fluxes (q_w) are determined as the product of suspended sediment concentration ($\tilde{c}$) and transect-averaged streamwise velocity ($\tilde{u}$) or vertical velocity ($\tilde{w}$), respectively. During ebb, horizontal sediment flux on average increases downstream of bedform troughs towards the crest in the entire water column coupled to the streamwise velocity field (**Figure 3.5b**). A minimum of horizontal flux occurs above the bedform troughs, in areas extending vertically for about half of the water column. Vertical sediment flux reaches overall highest magnitudes in these areas and is downward-directed (**Figure 3.5c**). Most of the bedform stoss-side is characterized by upward vertical flux.

Transect-averaged suspended sediment concentrations ($\tilde{c}$) during the flood phase (**Figure 3.5d**) similarly show a general decrease with height above the bed. Highest near-bed concentrations occur in the bedform troughs, above the steep bedform lee-sides and at the crests. The spatial variability in SSC in the upper water column is less pronounced than during the ebb (± 0.003 g L^{-1}) and independent of location in the bedform field.

Maximum horizontal sediment flux during the flood is observed above the crests and minima in the adjacent area above the troughs (**Figure 3.5e**). Highest vertical sediment flux is upward directed and located above the steep bedform flank and the crest (**Figure 3.5f**). Smaller magnitude downward vertical flux prevails for most of the remaining part of the bedform stoss downstream towards the troughs.

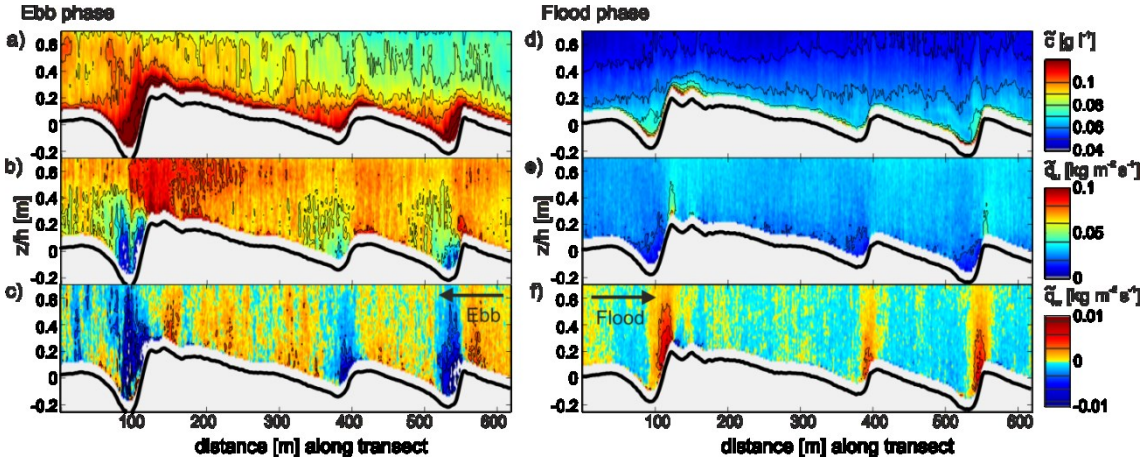

Figure 3.5. Transect-averaged suspended sediment concentration patterns for the flood (a – c) and ebb phase (d – f). (a, d) Suspended sediment concentration $\tilde{c}$ [g L^{-1}], (b, e) horizontal sediment flux q_u [kg s^{-1} m^{-2}] and (c, f) vertical sediment flux q_w [kg s^{-1} m^{-2}].

3.4.3. TIDAL VARIABILITY

Temporal variations in suspended sediment concentrations during the tidal cycle are examined at fixed positions in the bedform field. SSC from each transect was extracted for a position above the lower stoss, mid-stoss, crest and trough of the three bedforms at equal heights above the seabed (z = 2 m) (**Figure 3.6**). For all time series of SSC considered, noticeable temporal variations during the flood are limited to three transects (T2, T3 and T4, 08:20 – 09:15 (**Figure 3.2**)). The remaining flood transects show an almost equal distribution ($\pm$ 0.02 g L^{-1}) of suspended sediment concentration. During the ebb, SSC time series show greatest variability for transects T19 - T25 (16:20 – 19:30).

Spatially, maximum SSC of the flood tide occur during T3 (08:45) above bedform troughs. During the ebb phase, T19 (16:20) marks an abrupt increase in SSC in all time series. SSC in the bedform troughs is highest during this period, followed after by SSC at the crests.

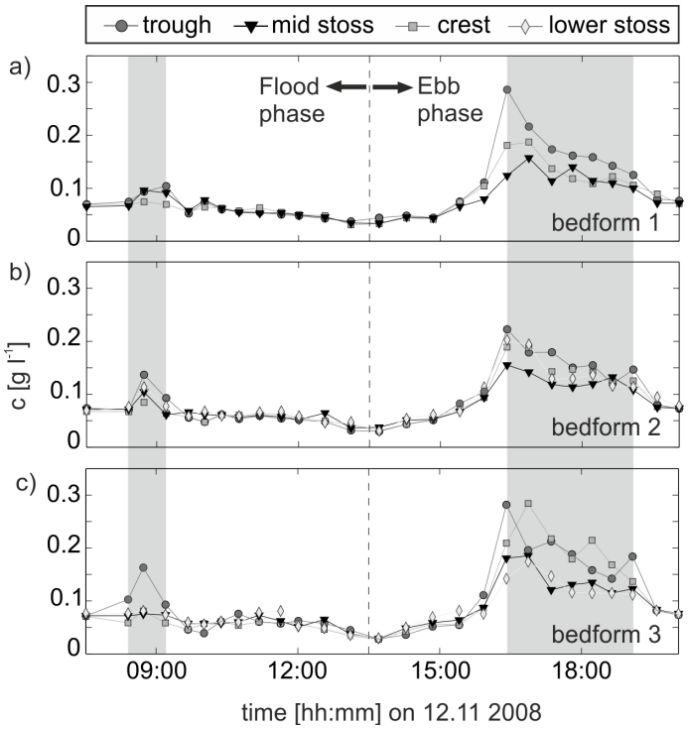

Figure 3.6. Suspended sediment concentration c [g L^{-1}] extracted at fixed locations from ship-based ADCP transects for flood and ebb phase at equal heights above the bed (z = 2 m). Color-coding refers to location in respect to the bedform field. (a) bedform 1; (b) bedform 2 and (c) bedform 3 (**Figure 3.1**). Time periods with strong topographic variability in SSC are shaded in grey.

Transects T3 and T19 with highest suspended sediment concentrations and greatest spatial variability in the corresponding tidal phase are shown in **Figure 3.7**, displaying SSC deviations from a spatial mean (c'_s) and the corresponding quadrant distribution map above bedform 3.

During the ebb phase, more than average suspended sediment occurs at the bedform crest and in the area above the trough extending downstream and into the upper water column. Higher than average SSC occurs also in patches above the bedform stoss-side. Generally, SSCs are higher in the presence of $Q2_s$/$Q3_s$ fluid motion. Structures of this type of fluid motion occur repeatedly downstream of the bedform trough with increasing vertical extent. Compared to the transect-averaged quadrant map (**Figure 3.3d**), instantaneous velocity measurements classified as $Q2_s$ occur further along the stoss-side.

During flood conditions, higher than average sediment concentrations occur above the lower bedform stoss and downstream towards the steep bedform lee. Sediment concentrations downstream of the crest are smaller than average. The quadrant map derived from instantaneous velocity measurement closely resembles the transect-averaged map in **Figure 3.4d**. Apart from the area above the steep bedform flank, $Q2_s$ motion is restricted to the lower stoss-side and of smaller scale than $Q2_s$ structures observed during the ebb.

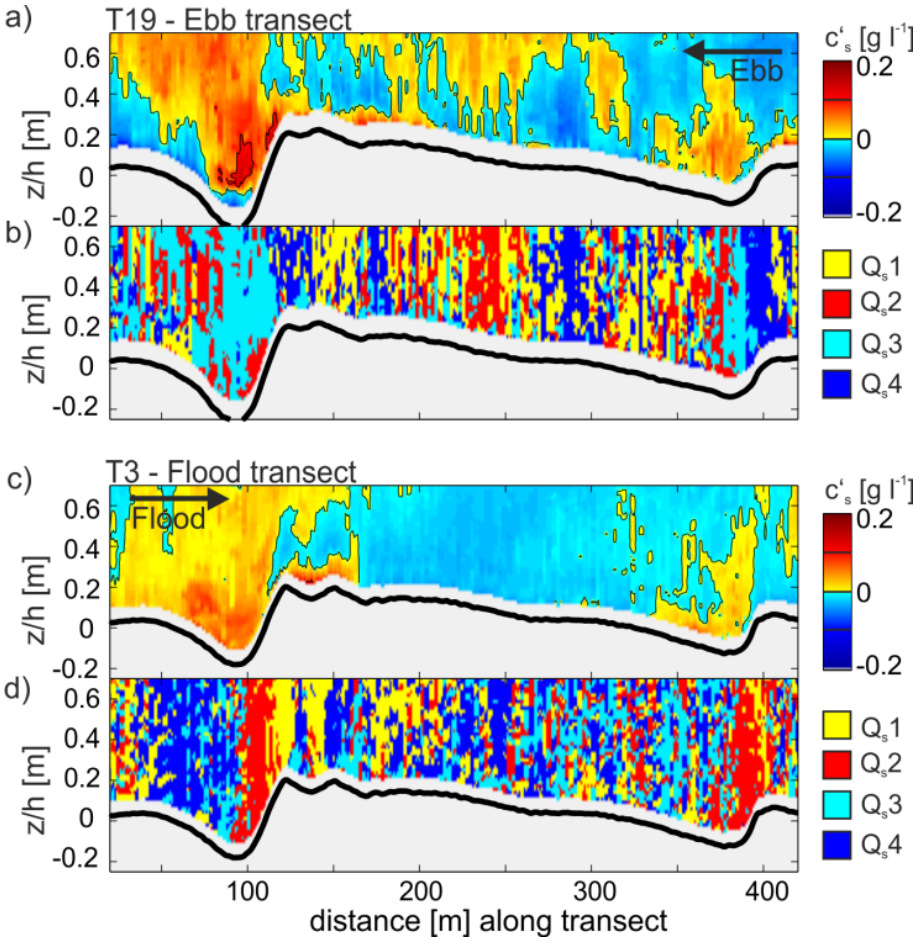

Figure 3.7. Selected ADCP transects during maximum ebb (a, b) and maximum flood flow condition (c, d). (a, c) Deviation of suspended sediment concentration c'$_s$ [g L^{-1}] from the spatial mean; (b, d) quadrant distribution above bedform 3.

3.4.4. Coupling of suspension patterns and the instantaneous flow field

The high tidal variability of suspended sediment transport is further examined by means of the stationary upward-looking TRBM ADCP located on the mid-stoss of bedform 3 (**Figure 3.1**). Sediment carried in suspension at this location is at times organized in distinct patterns, hereafter referred to as suspension structures. These suspension structures were particularly prominent when examining the fluctuation of SSC (c'_t) from a time-averaged mean.

Based on the observed SSC distribution and prevailing flow characteristics three stages are differentiated for the ebb phase: stage E1 (13:30 – 15:55) coincides with the period of accelerating currents, stage E2 (15:55 – 19:10) with the plateau of maximum velocities (> 1 m s^{-1}) and a sudden increase in depth-averaged SSC (by 0.033 g L^{-1}) and stage E3 (19:10 – 20:10) with decelerating flow and steady depth-averaged SSC values of 0.07 g L^{-1} (**Figure 3.2**).

During stage E1 (**Figure 3.8a**), well defined structures occur in the mid water column for about 150 s (corresponding to a horizontal extent of more than 100 m). In stage E2 (**Figure 3.8b**)

regular, columnar structures are observed, stretching over the entire water column, hereafter referred to as water-depth-scale structures (horizontal extent 20 – 40 m). Suspension structures of stage E2 appear simultaneously with an increase in clustering of quadrants. On visual inspection, ($Q2_t$) (slower-than-average upward flow) is predominately associated with suspension structures; while the area between structures is characterized by fluid motion of ($Q4_t$) (faster-than-average downward flow) (**Figure 3.8c**). Suspension structures disappear shortly before ebb slack water (stage 3, **Figure 3.8d**) and only scattered sediment clouds remain in the upper water column.

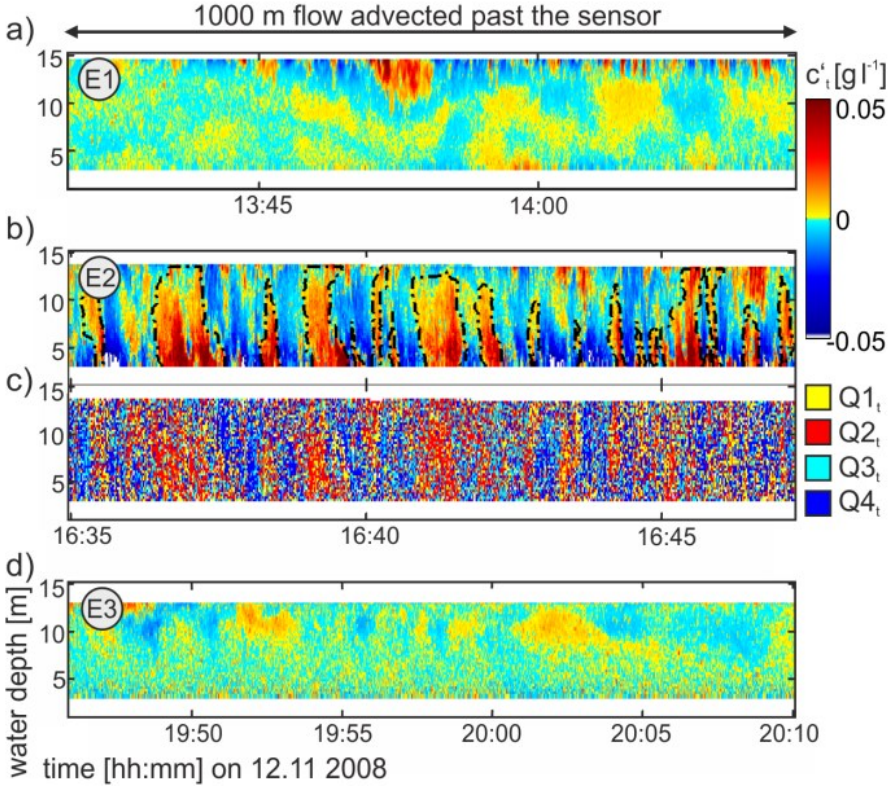

Figure 3.8. Stationary observation of SSC by TRBM ADCP during the ebb. (a) Snapshot of c'$_t$ [g L^{-1}] during stage E1, (b) c'$_t$ [g L^{-1}] of stage E2, (c) quadrant distribution for stage E2 and (d) c'$_t$ [g L^{-1}] stage E3. Each time period represent 1000 m of flow advected past the sensor. Structures detected via the algorithm are outlined in (b).

The differentiation into characteristic stages for the flood period (**Figure 3.9**) is not as straight forward as for the ebb phase. Stage F1 (20:10 – 22:45) coincides with the period of accelerating currents and the beginning of the first half of the maximum velocity plateau, stage F2 (22:45 – 00:35) with the second half of the maximum velocity plateau and stage F3 (00:35 – 02:10) with decelerating currents (**Figure 3.2**).

Stage F1 is marked by advection of few very large (300 – 500 m extent) water-depth-scale structures around 1 – 2 km apart as shown exemplarily in **Figure 3.9a**. Columnar structures appear in stage F2 (**Figure 3.9b**), quite irregular with significant variability in the horizontal

extent (20 – 300 m) and less pronounced SSC dominance compared to the ambient flow. No clustering of quadrants in the stationary flow measurements is observed during the entire flood period (**Figure 3.9c**). Similarly to the ebb, stage 3 consists of scattered suspension structures (**Figure 3.9d**).

The simultaneous measurements conducted with the ship-based ADCP enable the examination of the flow and sediment concentration field above the bedforms during the TRBM ADCP observation period. Stage E2 and F2 coincide with the time period of largest sediment concentrations and spatial variations measured in ADCP transects during each tidal phase (**Figure 3.6**). **Figure 3.7a, b** therefore displays an instantaneous view across the bedforms during stage E2 of the ebb and **Figure 3.7c, d** during stage F2 of the flood period. Coupled structures of higher than average sediment concentration and clustering of ($Q2_s$) above the mid-stoss in the ebb transect are believed to represent suspension structures detected in the TRBM ADCP data. The flood transect displays a minimum of suspended sediment above the mid-stoss and coupling to quadrants of fluid motion is not possible.

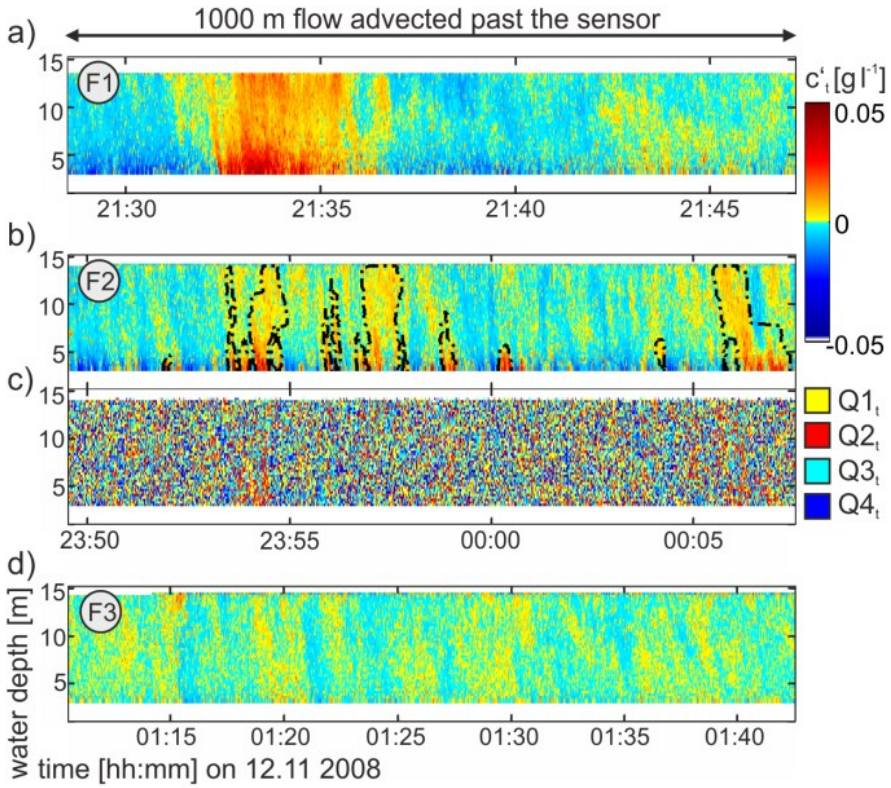

Figure 3.9. Stationary observation of SSC by TRBM ADCP during the flood. (a) Snapshot of c'$_t$ [g L^{-1}] during stage F1, (b) c'$_t$ [g L^{-1}] of stage F2, (c) quadrant distribution for stage F2 and (d) c'$_t$ [g L^{-1}] stage F3. Each time period represent 1000 m of flow advected past the sensor. Structures detected via the algorithm are outlined in (b).

The visual inspection of suspension structures above is complemented by the algorithmic structure detection as described in **section 3.3.1**. Generally, more suspension structures are

detected during the ebb than during the flood (252 and 88, respectively). For both tidal phases suspension structures are detected less frequent (periods 100 – 500 s) under accelerating tidal flows but frequencies remain high throughout the maximum velocity plateau (30 – 60 s), far into decelerating flows. With a few exemptions at the beginning of the flood, water-depth-scale structures are restricted to times of strong currents. During the ebb, the average sediment concentration within structures is highest under maximum current velocities (max. 0.2 g L^{-1}). However, during the flood, low-frequency, very large structures occurring under accelerating flow often contain more sediment (max. 0.14 g L^{-1}) than structures under maximum flood current velocity (0.1 g L^{-1}). The average duration of suspension structures during E2 is 25 s translating to horizontal extents of 31 m. The average period between structures during this period is 47 s (0.044 Hz).

Hydrodynamic signature of suspension structures

For each single ADCP bin determined to be part of a suspension structure, quadrant analysis is applied (**section 3.3**). Quadrant dominance of one structure is assessed. Quadrant dominance implies that most of the velocity measurements during the passing of one structure fall into that quadrant. In the following, focus is laid on structures detected during stages E2 and F2. Initial observations are confirmed: 73% of the structures detected during E2 are dominated by ($Q2_t$). During F2 of the flood no clear prominence of one quadrant exists: 27% are dominated by ($Q1_t$), 32% by ($Q2_t$) and 27% by ($Q3_t$). **Figure 3.10** displays a histogram for the horizontal extent of all structures detected during the ebb stage E2 and flood stage F2, grey-shades indicating the dominant quadrant. There is no relationship between quadrant dominance and the horizontal extent of a structure.

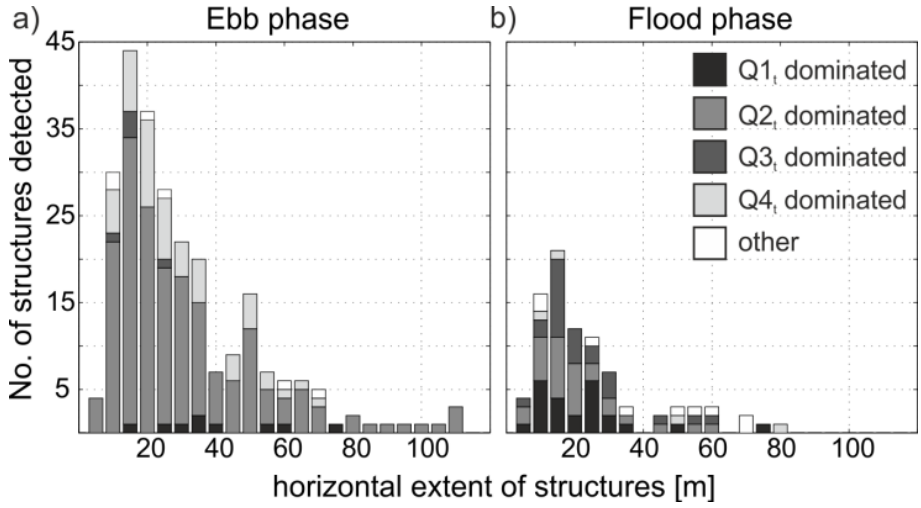

Figure 3.10. Quadrant dominance and the horizontal extend of suspension structures detected in TRBM data during (a) the ebb and (b) the flood. Quadrant dominance implies that most of the velocity measurements during the passing of one structure fall into that quadrant; the category 'other' is used when no quadrant dominated.

3.5. Discussion

Suspended sediment transport over bedform fields in natural environments occurs in patterns varying distinctively with flow direction and relative bedform orientation. The data presented here address the topographically-forced flow acceleration and deceleration and macroturbulent structures evolving in the presence of strong velocity gradients. In the following, we will (1) discuss the time-averaged flow features above the bedforms during the flood and ebb phase, (2) inspect the likely origin and characteristics of macroturbulence in the bedform field and (3) examine the suspended sediment characteristics above the bedform mid-stoss in the light of (1) and (2).

3.5.1. Time-averaged flow field

Flow in direction of bedform orientation

Under alignment of bedform orientation and flow direction (here: ebb phase, **Figure 3.11a**) the flow field exhibits time-averaged flow features commonly observed above asymmetric bedforms [*Best*, 2005b; *Coleman and Nikora*, 2011; *Venditti*, 2013]. Decelerated downward flow characterizes the bedform lee-sides 6 - 8 *H* downstream of the crest. Evidence of flow separation is given by the measured negative streamwise velocity in the bedform lee of the largest bedform. Lee-side regions show the greatest deviations from the spatially-averaged velocity profile (**Figure 3.3**). Since lee-side slope angles are comparable for all three bedforms (16 - 20°), flow separation likely occurs downstream of the smaller primary bedforms as well, but cannot be observed due to the limited measurement capabilities of the ADCP near the bed [*Kostaschuk et al.*, 2005]. Similar problems were encountered in the field in a previous study on the Knudedyb bedforms by Lefebvre et al. [2013a]. Their linked 2DV numerical modeling study however, showed separation cells downstream of all primary bedforms observed here with a streamwise extent of 5.7 – 6.2 *H* [*Lefebvre et al.*, 2013b]; agreeing with estimates based on the parameterization by Paarlberg [2007] (**Figure 3.11a**).

Flow against the bedform orientation

The flow field differs from the classic observations in equilibrium flows when flow and bedform orientation are opposed (here: flood phase; **Figure 3.11b**). The gentle bedform stoss-sides (< 2°) act as the temporary lee while the steep flow-facing sides form a positive step in topography. Flow separation processes associated with positive steps in topography involve the formation of a flow separation cell upstream of the step and immediately downstream of the leading edge [*Largeau and Moriniere*, 2006; *Abdalla et al.*, 2009; *Ren and Wu*, 2011]. However, no evidence of flow reversal was found in our ADCP measurements. The absence of flow separation and reversal in front of the steep flank is attributed to the relatively low angle of

the flank compared to positive step experiments (often 90°) and the smoothed transition from the trough towards the flank. Instead, the steep flank induces a pronounced upward flow, which extends throughout the entire water column (**Figure 3.4d**). Velocity profiles in this region show the greatest deviation from the spatially-averaged profile (**Figure 3.4e**). This upwelling likely has stationary water surface expressions (boils) in close vicinity to the bedform crests, although we can provide no evidence from our data. Downstream of this pronounced upwelling, overall flow deceleration due to the adverse pressure gradient is weak and no flow recirculation is established.

On a much smaller scale, Lefebvre et al. [2013a] found evidence of local, intermittent flow reversal downstream of the small crestal dune of bedform 3, which is attributed to the ongoing 'remolding' of the crests [*Martinius and Van den Berg*, 2011; *Becker et al.*, 2013] during the flood period. In the adjacent Grådyb tidal inlet, Ernstsen et al. [2006] described the formation of a 'flood cap' at the bedform crests. Such morphological alterations are believed to increase the sharpness of the leading edge and favor flow separation. The estimated extent of this flow separation cell based on the average flood bedform profile is indicated in **Figure 3.11b** [*Paarlberg et al.*, 2007]. The predicted extent is beyond the measurement capabilities of the ship ADCP and small compared to the primary bedform scale. This applies also for flow recirculation cells forming in the lee of the superimposed secondary bedforms.

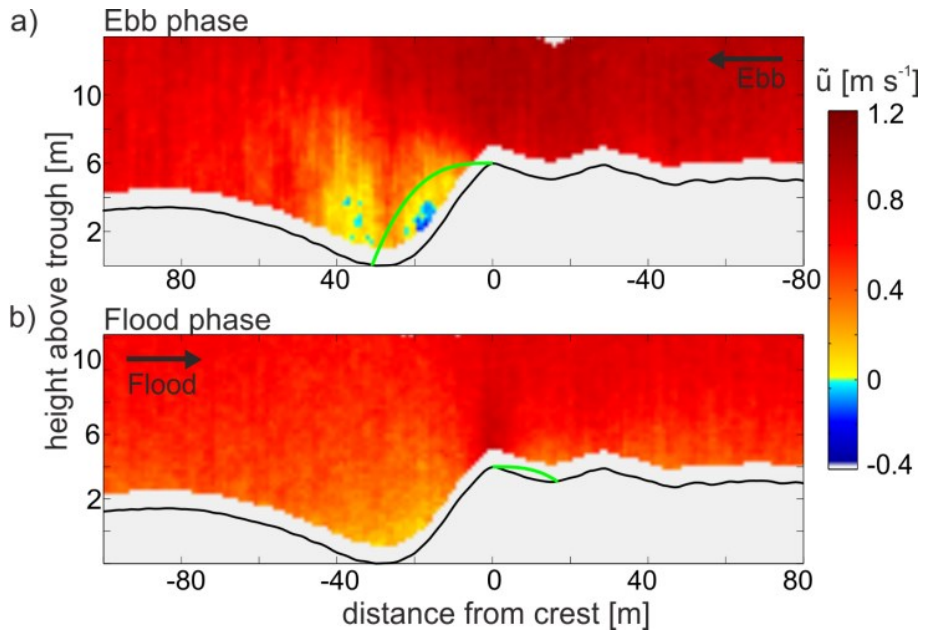

Figure 3.11. Transect-averaged streamwise velocity ($\tilde{u}$) [m s^{-1}] for ebb (a) and flood phase (b) at the largest bedform surveyed. The green line represents the parameterization of the flow separation line as proposed by Paarlberg et al., [2007].

3.5.2. Production of macroturbulence

Macroturbulence during the ebb

During most of the ebb phase, water-depth-scale coherent flow structures are observed in the stationary TRBM readings. These are revealed by confined clustering of ($Q2_t$) events, thus representing local upward motion of relatively slower flow entities advected by the mean flow (**Figure 3.8c**). These structures occur with an average period of 22 s and an average horizontal extent of 33 m.

The production of these coherent flow structures can be related to processes occurring in the flow separation zone of the primary bedforms. This is supported by the observation of decelerated upward flow structures ($Q2_s$) repeatedly occurring from the lower bedform stoss towards the crest in ADCP transects (**Figure 3.7a**). These structures occur in similar dimensions and frequencies as ($Q2_t$) structures in TRBM readings. The observed frequencies of macroturbulent structures above the mid-stoss side furthermore support the application of the modified Strouhal Law [*Strouhal*, 1878; *Levi*, 1983] for prediction of frequencies (f) of macroturbulence production in the presence of bedforms:

$$f = Sr\, U_b\, H^{-1} \qquad (3.6)$$

where H = 6 m is the bedform height, U_b = 1.2 m s^{-1} is the average flow velocity and Sr = 0.05 – 0.25 is a range of Strouhal numbers compiled by Venditti and Bauer [2005]. The majority of structures detected fall within the predicted frequency range of macroturbulence production due to the primary bedform (**Figure 3.12**). 8.7% occur with a smaller frequency than predicted, while 17.5 % occur with a higher frequency.

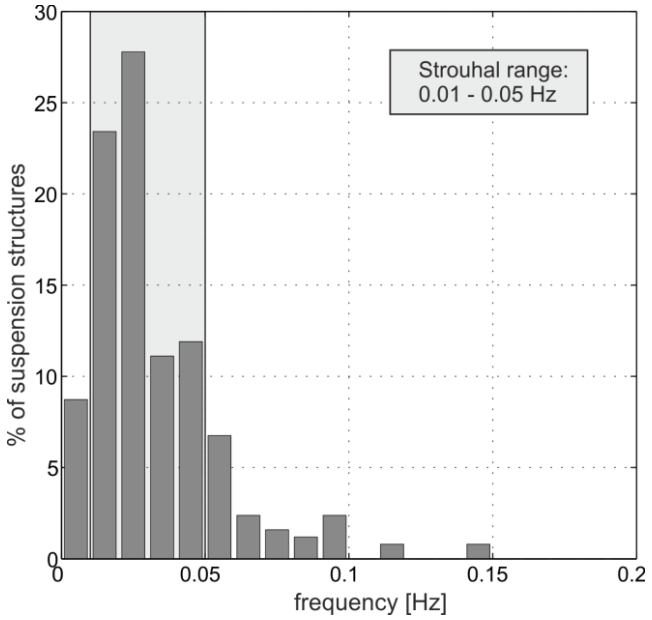

Figure 3.12. Frequency [Hz] of flow structures detected during the ebb velocity plateau (stage E2). The predicted range of frequencies (0.013 – 0.067 Hz) based on the Strouhal relationship (shaded box).

Regarding the mechanism of macroturbulence production in the flow separation cell, our observations suggest that upward directed flow structures appear downstream of the flow separation cell (**Figure 3.7a**). No upward flow is observed in the vicinity of the crest that would link the flow structures to the spanwise rollers shed immediately at the crest such as observed by Grigoriadis et al. [2009] and Omidyeganeh and Piomelli [2011]. Instead, the water-depth-scale structures observed here appear to be related to streamwise instabilities that grow in size past reattachment as described by e.g., Best [2005a] and Stoesser [2008].

Macroturbulence during the flood

Macroturbulence production during the flood period differs significantly from the ebb. Water-depth-scale flow structures are not observed in the TRBM ADCP readings. Furthermore, observations in ADCP ship transects indicate that upward decelerated flow structures occurring at the lower stoss during the flood never reach the extent of the flow structures during the ebb. The growth of the flow structures during the ebb might therefore be strongly influenced by the presence of a favorable pressure gradient above the bedform stoss, while the adverse pressure gradient during the flood suppresses vortex growth.

Previous indications for a difference in scale of macroturbulence production between flood and ebb phase have been given from estimates of hydraulic roughness above sub-aqueous bedforms. Turbulence production in bottom boundary layers involves the transfer of flow momentum to turbulent scales resulting in an increase of hydraulic roughness. Through the disintegration of overlapping boundary layers from a spatially-averaged velocity profile, estimates of specific roughness elements, such as grain or form roughness lengths, are made [*Smith and McLean*, 1977]. Above bedforms in uni-directional flows, the primary contributor to hydraulic roughness is macroturbulence originating in the zone of flow separation and therefore turbulence arising from the boundary layer associated with the largest form roughness [*Nelson et al.*, 1993]. In case of unsteady, tidal flow above compound bedforms in the Knudedyb, Lefebvre et al. [2013a] found significantly larger hydraulic roughness when flow and primary bedform orientation are in alignment. Primary ebb-oriented bedforms with superimposed secondary bedforms were active contributors to overall roughness during the ebb, while only the secondary bedforms played a role during the flood period.

Thus, we conjecture that during the flood a turbulent boundary layer associated with primary bedforms is absent and turbulence production is predominately associated with the boundary layer due to secondary bedforms that reverse orientation with each tidal phase. Since their dimensions are significantly smaller, the scale of macroturbulence is expected to be significantly smaller [*Fernandez et al.*, 2006].

Strouhal predictions based on primary bedform dimensions are not applicable during the flood period. The frequency range of macroturbulence predicted for superimposed secondary bedforms (H = 0.2 m, U_b = 0.9 m s^{-1}) is 0.225 – 1.125 Hz. This range of frequencies is close to the measurement frequency of the ADCP (0.434 Hz) and thus beyond the scale of flow structures we resolve in this study.

3.5.3. Suspended sediment dynamics

Macroturbulent suspended sediment transport during the ebb

Distinct suspended sediment patterns are observed in TRBM ADCP data during the ebb period (**Figure 3.8**). These appear sporadically at the beginning of the ebb period with relative low suspended sediment concentration. They are believed to be features arising from initial outwash of material settled during slack water from the tidal flats.

Regular suspension structures develop past a velocity threshold, coinciding with the occurrence of macroturbulent flow structures arising in the flow separation zone (**Figure 3.8b, c**). The transition occurs 2.3 h into the ebb once a depth-averaged current velocity of 1 m s^{-1} is exceeded (**Figure 3.2**). The threshold varies depending on bedform geometry and sedimentary

characteristics. In the Elbe estuary e.g., sediment-laden macroturbulence above compound bedforms appears past a velocity threshold of 0.6 m s^{-1} [*Kwoll et al.*, *2013*].

Furthermore, the threshold coincides with an increase in depth-averaged suspended sediment concentration, suggesting that continuous macroturbulence production is required and most effective for sediment suspension and continuous transport. The turbulence intensities associated with the bedform-generated macroturbulence appear to be larger than the previously observed enhanced intensities during greatest flow unsteadiness [*Gordon*, 1975; *Anwar*, 1981]. Furthermore, sediment-laden macroturbulence prevails longer than observed in the Elbe study by Kwoll et al., [*2013*] indicating that macroturbulence governs suspended sediment transport for most of the ebb cycle.

Two mechanisms are thought to be responsible for the coupling between high sediment concentration and macroturbulent flow structures: Firstly, sediment trapped within the separation zone is ejected through periodic expulsion of fluid during shear layer destabilization as observed by Schmeeckle et al. [1999]. A proportion of the sediment surpassing the crest settles towards the bed as indicated by the observed downward sediment flux and high sediment concentrations close to the bed above the bedform troughs (**Figure 3.5**). Estimated values of percentage of suspended load transported over the crest that is deposited in the lee range between 17 – 56% for lee-side slopes of 8 – 22° [*Kostaschuk et al.*, 2009]. Through this mechanism sediment is therefore thought to be resuspended into the outer flow provided the turbulence intensity associated with the flow structures is large enough.

The second mechanism involves the active entrainment of sediment along the bedform stoss-sides by coherent flow structures. Ejection events associated with streamwise vortices occurring downstream of reattachment are capable of lifting significant amounts of sediment in the outer flow region in sediment-laden kolks [e.g., *Kostaschuk and Church*, 1993]. We see, however, no evidence for suspension of material surpassing the crest into the outer flow by eddies shed at the separation point as described by Kostaschuk and Villard [1999] or Schmeeckle et al. [1999].

In viewpoint of morphological alterations, Ernstsen et al. [2006] found increased erosion from troughs toward the crests during accelerating ebb flow and sediment accretion from crest to troughs towards slack water in the Grådyb inlet. A similar pattern was observed by Kostaschuk and Best [2005] in the Fraser river. Under decelerating conditions, the average sediment concentration within flow structures in Knudedyb decreases, suggesting a decline in turbulence intensity and settling of sediment. Much of this material is deposited in the bedform lee thus contributing to bedform migration similar to observations by Kostaschuk et al., [2009]. Towards ebb slack water the macroturbulence diminishes.

Suspended sediment transport during the flood

The lag between flow velocity and suspended sediment concentration inherited from the ebb phase significantly influences sediment dynamics during the beginning of the flood phase. A similar characteristic can be inferred from the work of Stark et al. [2011] at this site, who found higher sediment deposition in the bedform field following the decelerating flood phase than around low slack water. As a consequence, large, sporadic pulses of sediment at the beginning of the flood period are swept over the bedform field, independently of any active suspension from the bed.

Active suspension of sediment is limited during the flood period. Flow structures are of a smaller scale and associated with secondary bedforms. Upward vertical sediment flux is solely observed above the steep flank associated with the rapid flow acceleration and convergence toward the crest (**Figure 3.5**). Near-bed sediment concentrations are largest in these areas, though little sediment is observed in the upper half of the water column.

In the Grådyb inlet, Ernstsen et al. [2006] observed little overall patterns in erosion and accretion during the flood period. Initial accretion characterized the steep flow-facing flank partially due to continuous settling of material under weak flood currents partially due to beginning erosion on the lower lee-side of the bedform. With pronounced flow acceleration and increased water depth a transition to erosion at the flank was observed, attributed to increased bed-load transport towards the crest and partial suspension of bed-load material. This was supported by simultaneous measurement of accretion at the bedform crest resulting in the 'remolding' of the crestal dune [*Martinius and Van den Berg*, 2011; *Becker et al.*, 2013].

These observations agree with our findings and suggest that the obstacle provided by the steep flank of the primary bedforms hinders suspension beyond the crest. Sediment transport on the stoss-side of the primary bedforms is believed to be associated with local entrainment and changes in orientation and downstream migration of the secondary bedforms. The general downward flux in the entire water column immediately downstream of the crest under the adverse pressure gradient hinders transportation beyond the scale of primary bedforms, resulting in an overall stable bed during the flood phase.

3.6. Conclusions

This study examines the production and dynamics of macroturbulent flow structures and associated suspended sediment transport patterns over asymmetric compound bedforms in a tidal channel. The magnitude and characteristics of sediment transport in suspension varies depending on the tidal flow direction:

When flow direction and bedform orientation are aligned (here: ebb phase), flow separation occurs at the crests of the primary bedforms and induces a recirculation cell at the steep lee slope (**Figure 3.11a**). Suspended sediment concentrations are high within the flow separation zone due to trapping of sediment by high turbulent intensities (**Figure 3.7a**). Water-depth-scale macroturbulent flow structures originate downstream of the flow separation cell and govern suspended sediment transport through (1) expulsion of sediment-laden fluid into the outer flow region during shear layer destabilization and/or (2) entrainment of sediment by ejections associated with streamwise vortices downstream of reattachment. The onset of sediment-laden macroturbulence production occurs after greatest flow acceleration at the beginning of the ebb phase and lasts until shortly before slack water. The frequency of macroturbulence production is predictable by adaptation of the Strouhal law.

If flow direction and bedform orientation are opposed (here: flood phase), the gentle-sloping bedform stoss-side serves as the temporary hydraulic lee-side. A strong upward directed jet is formed due to the steep flow-facing side (**Figure 3.4**). Flow separation and associated macroturbulence are absent. Suspended sediment transport is governed by the interaction of sediment remaining in suspension from the previous ebb phase and suspension due to turbulence associated with smaller secondary bedforms that reverse direction with each phase. Little sediment surpasses the steep flow-facing flank of the primary bedform limiting transporting capabilities to primary bedform length.

Acknowledgements

We thank the captain and crew of FK Senckenberg and the research institute Senckenberg am Meer for the ship time provided. Thanks are extended to C. Maushake and D. Sellhorn from Bundesanstalt für Wasserbau (BAW) for technical support during the field survey. This research was funded through the DFG-Research Center/Cluster of Excellence „The Ocean in the Earth System“.

INFLUENCE OF THE DUNE LEE-SLOPE ON FLOW AND TURBULENCE CHARACTERISTICS

Eva Kwoll[1], Jeremy G. Venditti[2], Alice Lefebvre[1], Ryan Bradley[2] and Christian Winter[1]

[1] MARUM-Center for Marine Environmental Sciences, University of Bremen, Germany

[2] Simon Fraser University, Burnaby, BC, Canada

Manuscript in preparation for submission to *Journal of Geophysical Research*

ABSTRACT

A prominent control on the flow field over subaqueous dunes is the slope of the downstream lee-side of the dunes. While most previous work has focused on steep, asymmetric angle-of-repose dunes (lee-slopes ~30°), little is known about lower angle dunes (< 14°). It has been shown that the prominent zone of flow separation and reversal in the lee of steep dunes is present intermittently or absent in the case of low angle dunes. Here, we examine the changes in the flow and turbulence field leading to low-angle dunes in a combined laboratory and numerical model investigation. Three sets of fixed dunes with lee-side slope angles of 10°, 20° and 30° were separately installed in a 12 m-long and 1 m-wide flume and subjected to a set of constant flows 0.20 m deep. Flow stages were scaled to the laboratory setup characterizing suspension-dominated transport conditions. Measurements include (1) high-frequency profiles measured with a Laser Doppler Velocimeter and (2) Particle Image Velocimetry (PIV) of the flow field over one of the experimental dunes. Furthermore, a 2DV non-hydrostatic numerical model (Delft 3D) was used to simulate the flow field over the three dune configurations. Results show that the size of the flow recirculation cell decreases with lower lee-slopes and is absent above the 10° dune configuration. Despite the variations in the size and presence of the flow recirculation cell, a layer of high vertical gradient in streamwise velocity, extending from the brink point downstream, was observed in all cases. The magnitude of turbulence intensities, Reynolds shear stress and turbulent kinetic energy inside the wake decreases with lee-slopes, while the vertical extent of the turbulent wake is independent of dune lee-slope. Form roughness decreases for lower lee-slopes; which suggest that roughness estimates based on dune height might be misleading.

4.1. INTRODUCTION

In the alluvial and coastal environments, bedforms take on a variety of shapes and scales as they form through the interaction of the mobile sandy bed and turbulent flow field. Large bedforms that interact with the flow field across the entire water depth are referred to as dunes. Dunes in particular have been subject to extensive research due to their significance in controlling hydraulic roughness [e.g., *Ogink*, 1988; *Julien et al.*, 2002; *Bartholdy et al.*, 2010; *Paarlberg et al.*, 2010] and sediment transport [*Engelund and Fredsoe*, 1982; *Gomez et al.*, 1989; *Lapointe*, 1992; *Kostaschuk and Villard*, 1996b]. A morphological difference has been noted between dunes forming under laboratory conditions and observed dunes in natural environment. While laboratory dunes often assume an asymmetric shape with a steep angle-of-repose lee-side of ~30^{o} [e.g., *Nelson et al.*, 1993; *Bennett and Best*, 1995; *Venditti and Bennett*, 2000; *Wren et al.*, 2007], natural dunes typically have lower angle leeside slopes (< 14°) and often a more symmetric shape [*Smith and McLean*, 1977; *Kostaschuk and Villard*, 1996b, 1999; *Roden*, 1998; *Carling et al.*, 2000a; *Sukhodolov et al.*, 2006]. For example the mean lee-slope compiled from the geometric properties of 1400 dunes in the Jamuna River, Bangladesh was 8.4° [*Roden*, 1998; *Best et al.*, 2007].

The causes behind the differences in morphology between low and steep angle dunes are not fully understood. It has been suggested that increased transport of sediment in suspension may lead to increased deposition in the dune lee, leading to a decrease of the lee-slope [*Smith and McLean*, 1977; *Kostaschuk and Villard*, 1996b; *Kostaschuk et al.*, 2009]. Similarly, dune morphology is altered during the transition towards upper stage plane bed conditions due to the increased presence of suspended sediment transport [*Saunderson and Lockett*, 1983; *Bridge and Best*, 1988]. During the transition, flatter dune morphologies have been attributed to damping of macro-turbulence under high suspended sediment concentrations [*Bridge and Best*, 1988]. Another related mechanism that has been observed is the suppression of macroturbulence by high clay concentrations, which flattens dune morphology [*Wan and Wang*, 1994; *Baas and Best*, 2008]. On the other hand, low lee angles have also been observed for isolated dunes in bed-load dominated environments [*Carling et al.*, 2000a; *Sukhodolov et al.*, 2006]. Here, supply rate to the lee is limited by migrating superimposed dunes that may lead to erosion of the brink point and accretion on the dune stoss.

The prominent control exerted by the lee-slope on the turbulent flow field above dunes is the presence or absence of flow separation and flow reversal in the dune lee [*Smith and McLean*, 1977; *Kostaschuk and Villard*, 1996b; *Carling et al.*, 2000b; *Sukhodolov et al.*, 2006]. In the lee of dunes with lee angles close to the angle of repose (25-30°) a well described recirculation cell exists, caused by the rapid flow expansion and deceleration downstream of the topographical step [e.g., *Bennett and Best*, 1995; *Venditti and Bennett*, 2000; *Venditti*, 2007]. A separated

shear layer borders the recirculation cell and reattaches 4-5 dune heights (*H*) downstream. An internal boundary layer (IBL) develops with increasing vertical extent towards the crest and is affected by the flow acceleration above the dune stoss. High turbulence production along the shear layer and at flow reattachment causes a momentum deficit that is advected in a wake structure. The IBL and overlying wake increasingly interact with downstream distance. Turbulence production in the flow separation region involves the generation of large macroturbulent vortices that may translate to the water surface as boils [*Matthes*, 1947; *Jackson*, 1976] and govern suspended sediment transport above dunes [*Lapointe*, 1992; *Kostaschuk and Church*, 1993; *Venditti and Bennett*, 2000].

Above low-angle dunes, flow deceleration in the dune lee is less pronounced and flow separation is absent or intermittent [e.g., *Roden*, 1998; *Carling et al.*, 2000b; *Best and Kostaschuk*, 2002]. However, studies have shown that macroturbulence production and the formation of a wake layer also occurs above low-angle dunes [*Best and Kostaschuk*, 2002; *Sukhodolov et al.*, 2006]. The exact mechanisms behind this however, are still unclear. Best and Kostaschuk [2002] studied flow over laboratory low-angle (lower lee-slope = 14°) dunes. They showed that a flow deceleration zone replaced the region of permanent flow separation in the dune lee and a smaller zone of intermittent flow reversal occurred for 4% of the time. Velocity differential in shear layers bordering this deceleration zone were smaller than downstream of dunes with permanent flow separation. They attributed turbulence production to eddy generation along this shear layer.

Here, we explore the flow over bedforms with a wider range of lee-slopes in an attempt to discover the changes in the flow field that occur, leading to low angle dunes. We focus on the effect of the dune lee-slope on time-averaged flow and turbulence characteristics using observations of flow over fixed laboratory dune geometries and numerical simulations. We address the following questions: (1) how do numerical model investigations compare to laboratory measurements in examining the time-averaged flow and turbulence field? (2) In a time-averaged sense, what are the characteristics of flow separation for varying dune lee-slopes? (3) How does the magnitude of turbulence production change with varying lee-slopes and effects wake layer characteristics? (4) What impact can be expected on the hydraulic roughness of low-angle dune?

4.2. Methods

4.2.1. Experimental Procedure

Laboratory experiments were conducted at the Environmental Fluid and Sediment Dynamics Laboratory at the Simon Fraser University, Canada. A glass-sided flume, 15 m long, 1 m wide and 0.6 m deep, equipped with a recirculating pump (flows up to 0.2 $m^3 s^{-1}$) and adjustable slope (-0.5 to 2.0%) was used.

Transport stage scaling

At present, no clear hydraulic scaling has been demonstrated for low and high angle dunes, i.e. both dune configurations occur at the same Froude and Reynolds numbers. However, observations of natural dune morphologies and associated transport regimes indicate that low angle dunes are more frequent in environments with dominance of suspended sediment transport [e.g., *Smith and McLean*, 1977; *Kostaschuk and Villard*, 1996b]. Here, we adopt a scaling for our experiments where the Froude, Reynolds and grain Reynolds numbers are lower regime, fully turbulent and hydraulically rough, respectively, and focus on matching the transport stage (T) between field conditions and our experiments. Transport stage (T) is defined as the ratio of the dimensionless shear stress (τ_*) - the Shields number - and its critical value for sediment entrainment (τ_{*cr}) [*Yalin*, 1972; *Church*, 2006; *Lin and Venditti*, 2013]. The Shields number is defined as

$$\tau_* = \frac{hS\rho_w}{D(\rho_s - \rho_w)}, \qquad (4.1)$$

where (h) is the water depth (S) is the water surface slope, (D) the grain diameter and (ρ_w) and (ρ_s) are water and sediment density, respectively.

In rivers, a bedload dominated environment occurs when $0.01 < \tau_* < 0.1$, a mixed transport stage occurs when $0.1 < \tau_* < 1$ and a suspension dominated condition occurs when $\tau_* > 1$ [*Dade and Friend*, 1998; *Church*, 2006; *Lin and Venditti*, 2013]. Based on this, Lin and Venditti [2013] used $T > 33$ as the appropriate threshold for suspension-dominated environments.

In our experiments, we use a Shields number of 1, a critical Shields number of 0.03 and corresponding $T = 33$, at the threshold between a mixed and suspension-dominated conditions. For a mobile bed, this would cause high suspended bed material fluxes, while remaining in the subcritical, lower stage regime in which dunes occur. The resulting flow conditions are summarized in **Table 4.1**.

Dune Design

The prototype dunes were designed based on a collection of morphological characteristics of natural dunes in riverine and estuarine (Elbe and Fraser river) environments. Average lee-slopes of reported dunes are around 12°. In both environments, variations in dune heights (H), lengths (L) and water depths (h) are approximated by the well-known relationships of Allen [1982] and Flemming [1988].

The prototype dunes were therefore designed by selecting an appropriate dune aspect ratio (H/L) and in accordance with relationships of Allen [1982] and Flemming [1988]. The aspect ratio was chosen based on the relationship of aspect ratio and transport stage examined by Yalin [1972] and revisited by Lin and Venditti [2013]. Following the transport stage scaling for T = 33, an aspect ratio of 0.033 was chosen. Dune heights and lengths were 0.03 m and 0.9 m, respectively, in water depths of 0.2 m (**Table 4.1**). The field data suggest an increase in dune aspect ratio with lee-slope angle (**Figure 4.1**); for means of comparison however, the aspect ratio is kept constant.

In addition, field observations suggest that natural bedform morphologies often exhibit a gentle rounded crest, sloping downward towards a sharp break (brink point) and a steep slope (lee-slope) towards the bedform trough [e.g., *Parsons et al.*, 2005; *Kostaschuk et al.*, 2009]. To approximate this phenomenon in the experimental dunes, the brink points are located midway between dune crest and downstream trough at equal heights for all three setups. This ensured a decrease in asymmetry towards more symmetrical shapes for lower lee-slope angles, as observed from field data [*Best*, 2005b; *Venditti*, 2013]. The resulting templates of the experimental dunes are shown in **Figure 4.2.**

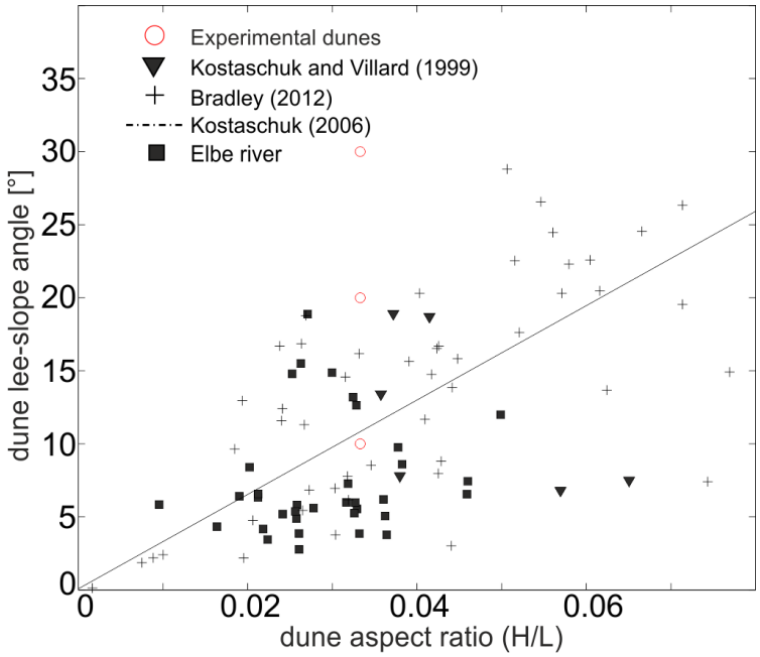

Figure 4.1. Dune aspect ratio vs. lee-slope angle of natural dunes from the Elbe and Fraser River [*Kostaschuk and Villard*, 1999; *Bradley*, 2012] and prediction based on linear relationship by Kostaschuk [2006]. The experimental dunes of this study are indicated (red circle).

Dunes were carved out of high-density styrofoam to mm-precision. The dunes were coated with a thin layer (~1 – 1.5 D_{50}) of fine sandy sediment (D_{50} = 160 µm) to provide natural grain roughness. Each bed set-up was made up of 10 dunes, covering a 9 m long working section.

Table 4.1. Experimental flow and dune characteristics.

Parameter	**Unit**	**Value**
Transport stage (T)	-	33
Critical Shields shear stress (τ_{*cr})	-	0.03
Non-dimensional shear stress for suspension dominated environment (τ_{*})	-	1
Slope (S)	-	0.00132
Mean flow velocity (U)	[m s^{-1}]	0.61991
Froude Number (Fr)	-	0.44257
Reynolds Number (Re)	-	1.24 E+05
Grain diameter ($D = D_{50}$)	[mm]	0.16
Water depth (h)	[m]	0.2
Dune height (H)	[m]	0.03
Dune length (L)	[m]	0.9
Dune aspect ratio (H/L)	-	0.033
Dune lee-slope	[°]	10, 20, 30

4.2.2. Data collection

All measurements were carried out near the flume centerline above the 7th dune for each of the three dune configurations. At-a-point velocity measurements were obtained across the measurement dune with a 6W TSI Laser Doppler Velocimeter (LDV). The flow was seeded with 10 μm, neutrally buoyant glass particles to achieve data rates of >300 Hz. Vertical profiles composed of 60 s time series measurements of streamwise (u), cross-stream (v) and vertical (w) velocity were measured. The data were validated internally through the TSI FlowSizer Software [*TSI Incorporated*, 2005] resulting in approximately 960 valid measurements per time series. The probe head was tilted by 3° in order to obtain measurements of all three components within mm of the bed. The density of measurements is shown in **Figure 4.2**. The data were resampled to provide eventime measurements at 16 Hz and despiked using a method of Goring and Nikora [2002].

High resolution Particle Image Velocimetry (PIV) was also performed to derive instantaneous images of the entire velocity field. An Argon Laser (50 Joules) was used to produce a ~1 mm thick light sheet approximately 30 cm away from the flume side wall, illuminating the seeded flow across the 7th dune. In order to avoid distortions due to water surface activity, the laser sheet was directed through a Plexiglas surface that was 1 m long and 5 cm wide positioned at the water surface. Double frame images were collected at 100 Hz, using a SpeedSense 9500 Camera (1600 x 2400 pixel). Three sets of images were collected moving the camera in streamwise direction with a small overlap between frames (**Figure 4.2**). Calibration of the images was achieved by capturing the image of a ruler and determination of the scale factor through the Dynamic Studio Software (Version 3.20) [*Dantec Dynamcis*, 2011]. Exposure time was set to 2079 μs and the time between double frames set to 4153 μs. Based on considering the rule of thumb of 25% travel time in between images, an interrogation area of 64 x 32 pixels was chosen for analysis. The resulting vertical resolution was 2 mm and the horizontal resolution was 4 mm. A total of 1400 images were captured for each camera position. Prior to the velocity computations, the quality of PIV images was improved by applying light balancing and mean intensity subtraction [*Dantec Dynamcis*, 2011]. Adaptive Correlation was performed to determine the instantaneous flow fields. Specifications include the use of deforming windows, quality check of velocity estimates based on the 5 x 5 median neighborhood validation and central differencing in velocity computations [*Dantec Dynamcis*, 2011]. The settings are based on a sensitivity analysis using the LDV data.

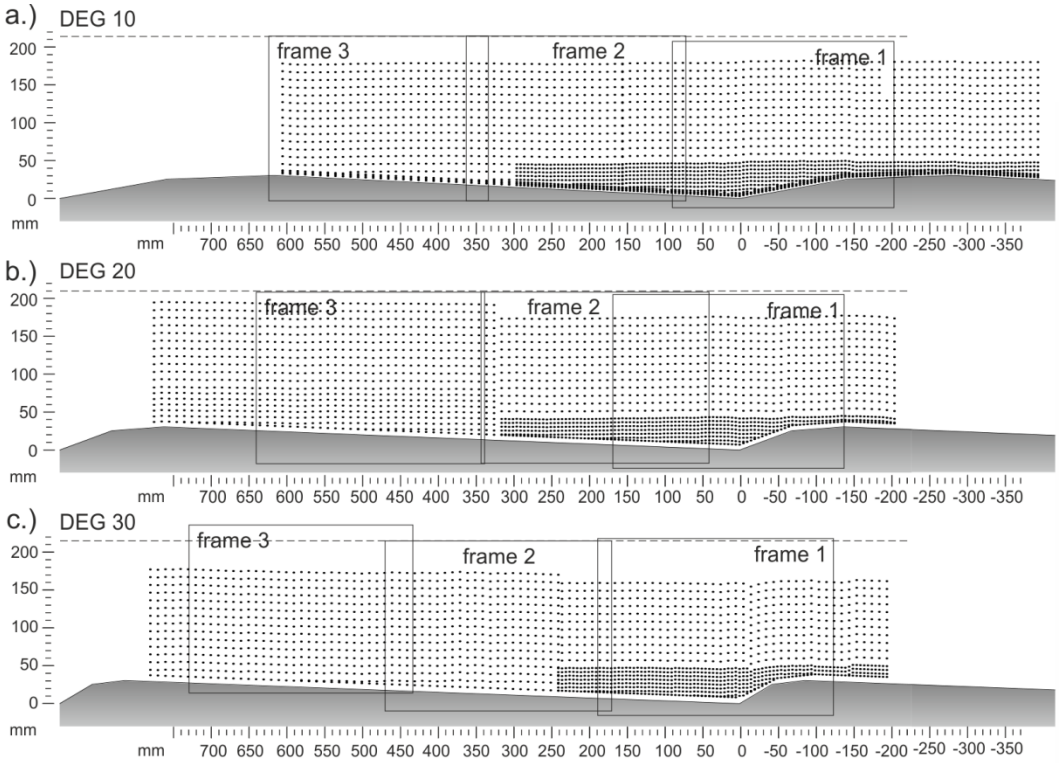

Figure 4.2. Experimental dune design and LDV data collection points and PIV image frames for all three bed setups of the 10° dunes (a), the 20° (b) and the 30° dunes (c).

4.2.3. 2DV NUMERICAL MODEL

A two-dimensional vertical (2DV) numerical model was setup using the open-source Delft3D-FLOW modeling system [*Deltares*, 2011]. The numerical model solves the Reynolds-averaged Navier-Stokes equations through a turbulence closure scheme. The model was set up using a k-ε turbulence closure model and the non-hydrostatic module. The model has been previously calibrated and validated against laboratory measurements and was shown to correctly reproduce flow over dunes, in particular hydrodynamics within the flow separation zone [*Lefebvre et al*., sub.].

All simulations were performed on a plane Cartesian model grid discretizing the fixed bed with 10 identical dunes based on the dune prototype used in the laboratory. Open boundary conditions were prescribed at the upstream end as a constant velocity in a vertical logarithmic profile and at the downstream end as a constant water level of 0 m. The bed resistance was defined as a uniform roughness length (z_0). A horizontal grid size of 6 mm and a layer thickness of 1 mm between trough and crest, increasing to 1.5 cm within the water column were chosen in order to ensure a high resolution within the flow separation zone [*Lefebvre et al*., sub.]. A timestep of 5 10^{-5} sec, a uniform background horizontal viscosity of 10^{-5} m^2 s^{-1} and vertical viscosity of 0 m^2 s^{-1} were used.

A sensitivity analysis and model calibration was carried out. The best comparison between model and lab measurements was found using z_0 = 0.002 m and the results were not sensitive to variations in background horizontal viscosity between 10^{-4} and 10^{-6} m^2 s^{-1}.

4.2.4. Data analysis methods

Due to the approach of the numerical model in solving the Reynolds-averaged Navier-Stokes equations through a turbulence closure scheme, the model output consists of time-averaged flow and turbulence parameters, namely time-averaged streamwise velocity component ($\bar{u}$), vertical velocity component ($\bar{w}$) and 2-dimensional turbulent kinetic energy (TKE_{uw}). From the laboratory measurements these quantities are computed for each time series of instantaneous velocity measurements for each location of the LDV and interrogation area of PIV via

$$\bar{u} = N^{-1} \sum_{n=1}^{N} u_i \quad (4.2),$$

$$\bar{w} = N^{-1} \sum_{n=1}^{N} w_i \quad (4.3),$$

$$TKE_{uw} = {}^{1}/_{2}\, \rho_w (\overline{u'^2} + \overline{w'^2}) \quad (4.4)$$

where (u_i) and (w_i) are the instantaneous velocities, $u' = u_i - \bar{u}$ and $w' = w_i - \bar{w}$ are velocity fluctuations, (ρ_w) is the density of water and (N) is number of measurements at each point.

The root-mean-square value of streamwise (u_{rms}) and vertical velocity (w_{rms})

$$\mathrm{u_{rms}} = (\mathrm{N}^{-1} \sum_{\mathrm{n=1}}^{\mathrm{N}} (\mathrm{u_i} - \bar{\mathrm{u}})^2)^{0.5} \quad (4.5),$$

$$w_{rms} = (N^{-1} \sum_{n=1}^{N} (w_i - \bar{w})^2)^{0.5} \quad (4.6)$$

and were determined for the laboratory data. Reynolds shear stress was computed from

$$\tau_{uw} = -\rho_w \overline{u'w'} = -\rho_w \mathrm{N}^{-1} \sum_{\mathrm{n=1}}^{\mathrm{N}} (\mathrm{u_i} - \bar{\mathrm{u}})(\mathrm{w_i} - \bar{\mathrm{w}}) \quad (4.7).$$

4.3. Results

4.3.1. Time-averaged flow field

Contour plots of the time-averaged streamwise velocity component for all experiments are shown in **Figure 4.3**. Common features of the flow are evident for all three beds: flow

acceleration above the gentle sloping stoss-side and flow deceleration following the step in topography. Largest streamwise velocities occur above the dune crests, the lowest streamwise velocities close to the bed above the dune troughs. The degree of deceleration decreases with lee-slopes. Negative streamwise velocities, commonly used as an indicator of flow separation, are predicted by the 2DV numerical model in the lee of the 20° and 30° dunes. Laboratory measurements indicate reversed flow in the lee of the 30° dune only.

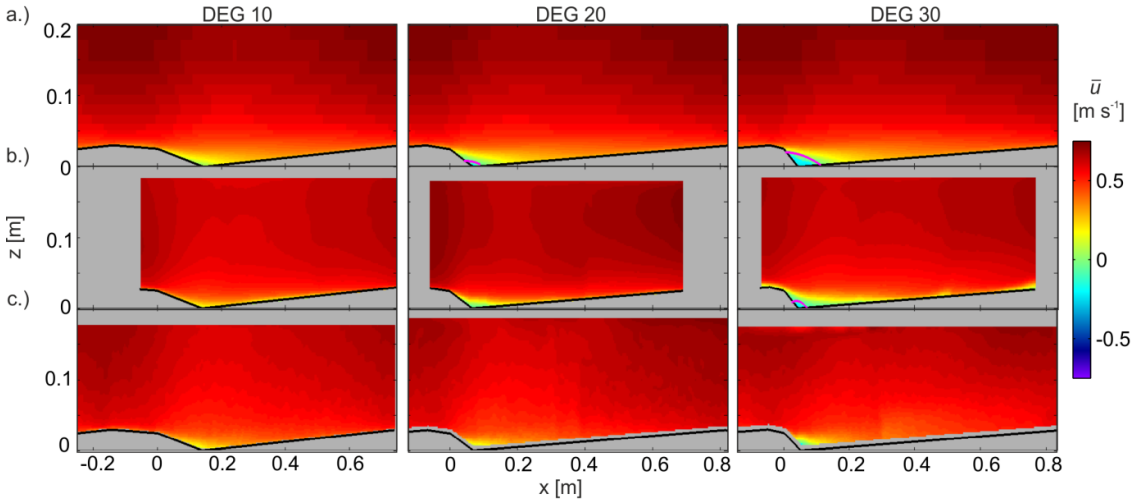

Figure 4.3. Time-averaged streamwise velocity ($\bar{u}$) [m s^{-1}] above the three bed set-ups from (a) 2DV numerical model, (b) PIV measurements and (c) LDV measurements. Lee-side slopes increase from left panel to right panel (10°, 20° and 30°). Estimated extents of the flow separation zone [*Paarlberg et al.*, 2007; *Lefebvre et al.*, sub.] are indicated where applicable.

Vertical velocities are negative in the area downstream of the dune crests and for approximately 0.2 m downstream of the brink point above all lee-slopes (**Figure 4.4**). The vertical extent of these patches is variable for each bed, but generally does not extend over the entire water column. The maximum negative velocity over all three beds is located just downstream of the brink point above the lee-slope. Modeled vertical velocities in this area are higher than measured values. All three approaches show that negative vertical velocities are highest above the 20° dunes (LDV: -0.07 m s^{-1}) and lowest above the 30° dunes (LDV: -0.05 m s^{-1}). Negative vertical velocities are also present in the upper 5 cm of the water column in model predictions and LDV measurements, but remain positive in PIV data. Confined areas of positive vertical velocities occur in the areas associated with negative streamwise velocity downstream of the 20° and 30° dune. Vertical velocity is positive above the stoss in the lower water column, decreasing with height above bed and increasing downstream towards the crest. The greatest magnitudes in these areas are reached above the 10° bed (LDV: 0.035 m s^{-1}).

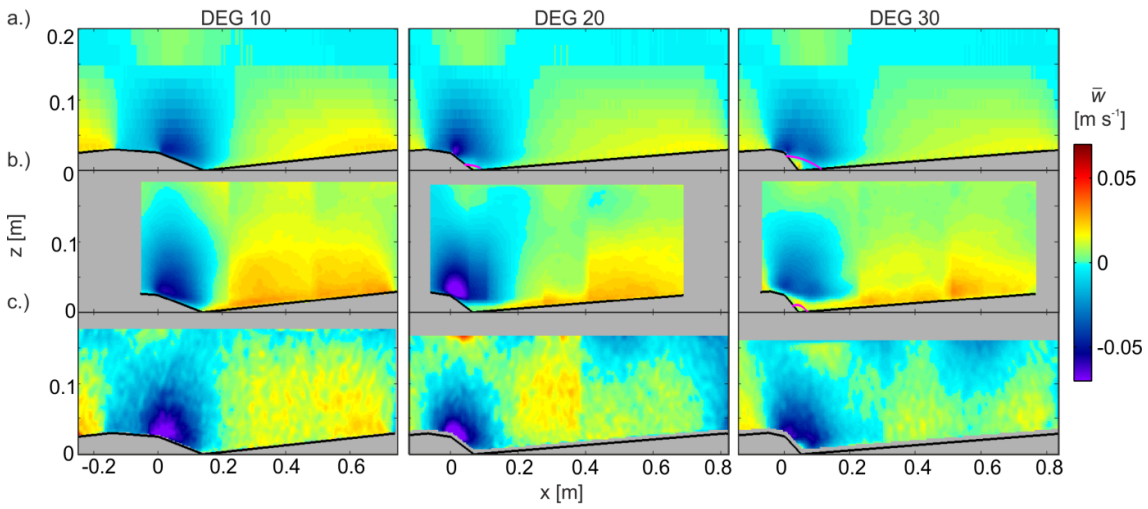

Figure 4.4. Time-averaged vertical velocity ($\bar{w}$) [m s^{-1}] above the three bed set-ups from (a) 2DV model, (b) PIV measurements and (c) LDV measurements. Lee-side slopes increase from left panel to right panel (10°, 20° and 30°). Estimated extents of the flow separation zone [*Paarlberg et al.*, 2007; *Lefebvre et al.*, sub.] are indicated were applicable.

4.3.2. Extent of the flow separation zone

The position of the flow separation line, marking the extent of the flow separation zone, was calculated following the method of Paarlberg et al. [2007] and Lefebvre et al. [sub.]. It was defined as the height above the bed at which the integral of the velocity between the bed and this particular height is zero. The flow separation lines are indicated in **Figure 4.3** and **Figure 4.4**, provided negative velocities were detected and numerous enough (negative velocities found on at least 4 profiles) to yield conclusive results. A zoom into the area downstream of the brink point is given in **Figure 4.5**. PIV, LDV and modeled velocity profiles in the dune lee are shown for the three lee-slopes. Furthermore, where applicable, the flow separation line is drawn and the zero-velocity line, enclosing the area of negative streamwise velocity.

No flow separation zone is detected over the 10° dunes in both laboratory measurements and model simulation results (**Figure 4.5a**). The profiles show that the model consistently underpredicts streamwise velocity in this region by ~0.05 m s^{-1} compared to the LDV measurements. Close to the bed along the lower stoss side, PIV measurements show a marked decrease in streamwise velocity that is not captured in the modeled data.

In case of the 20° dunes (**Figure 4.5b**), the model predicts a small zone of flow separation (FSZ) at the toe of the dune, with a vertical extent of 0.3 H and downstream extent of 2.2 H. The separation point is located at a distance of 1.9 H downstream of the brink point; the point of reattachment is located x = 4.1 H. The maximum upstream velocity is -0.058 m s^{-1} (9.5% of average $\bar{u}$). No sign of flow reversal is found in the laboratory measurements. This might be due to the difficulties of measuring very close to the bed and the small extent of the FSZ or due to

the absence of a FSZ in the flume. Deviations between PIV and LDV measurements are largest for this dune configuration. PIV streamwise velocities are up to 0.07 m s^{-1} higher than LDV measurements and possibly fail to detect the small magnitude reversed flow at the dune toe.

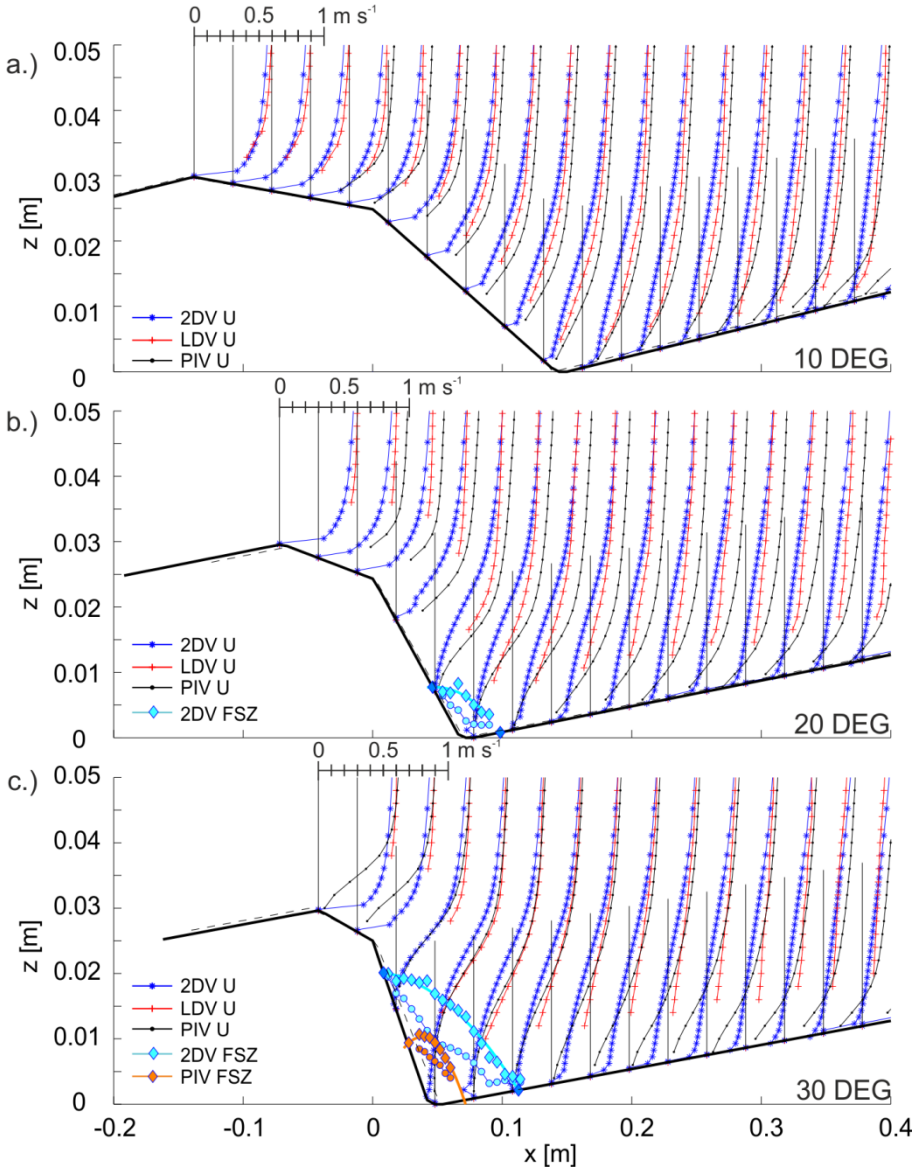

Figure 4.5. Flow field characteristics in the dune lee of (a) the 10° dune, (b) the 20° dune and (c) the 30° dune from PIV measurements, LDV measurement and 2DV numerical model. The flow separation line (diamonds) and zero-velocity line (circles) are indicated were detected.

Above the 30° dunes (**Figure 4.5c**), the modeled flow separation zone initiates below the brink point (z = 0.8 H) and extends 4.1 H (x = 4.4 H) downstream. Negative velocities within the flow separation zone reach magnitudes of -0.08 m s^{-1} (13% of average $\overline{u}$). Maximum negative velocities detected by the PIV and LDV are -0.003 and -0.004 m s^{-1}, respectively. The vertical and horizontal extent of the flow separation zone calculated from the PIV data is about half of that predicted by the model (z = 0.4 H; x = 2.8 H). The data points of the LDV close to the bed are too few to calculate a flow separation line. The agreement between PIV and LDV velocity

profiles is very good in the dune lee, indicating the absence of sufficient negative velocities in the LDV is mainly due to the lack of measurements close to the bed. The model might therefore be overestimating the extent of the FSZ.

4.3.3. TIME-AVERAGED TURBULENCE STRUCTURE

Horizontal and vertical turbulence intensities are proportional to the root-mean-square value of streamwise (u_{rms}) and vertical velocity (w_{rms}). **Figure 4.6** shows (u_{rms}), (w_{rms}) and (τ_{uw}) for the PIV data. Data from each dune configuration were overlain at the brink point and vertical profiles extracted. All profiles show elevated (u_{rms}), (w_{rms}) and (τ_{uw}) values in a zone extending from the brink point towards the downstream crest in the lower water column, marking the extent of the wake layer. Turbulence intensities and shear stresses are small immediately above the lee-slope and below the separation line. Maximum (u_{rms}) and (w_{rms}) in the shear layer above the 30° dunes are 1.5 times higher than above the 10° and 20° dunes. Shear stresses are twice as high over the steepest dune compared to the 10° and 20° dunes, with less pronounced differences. The effect of the upstream wake is evident by a small increase in turbulence parameters particularly in the 30° profiles.

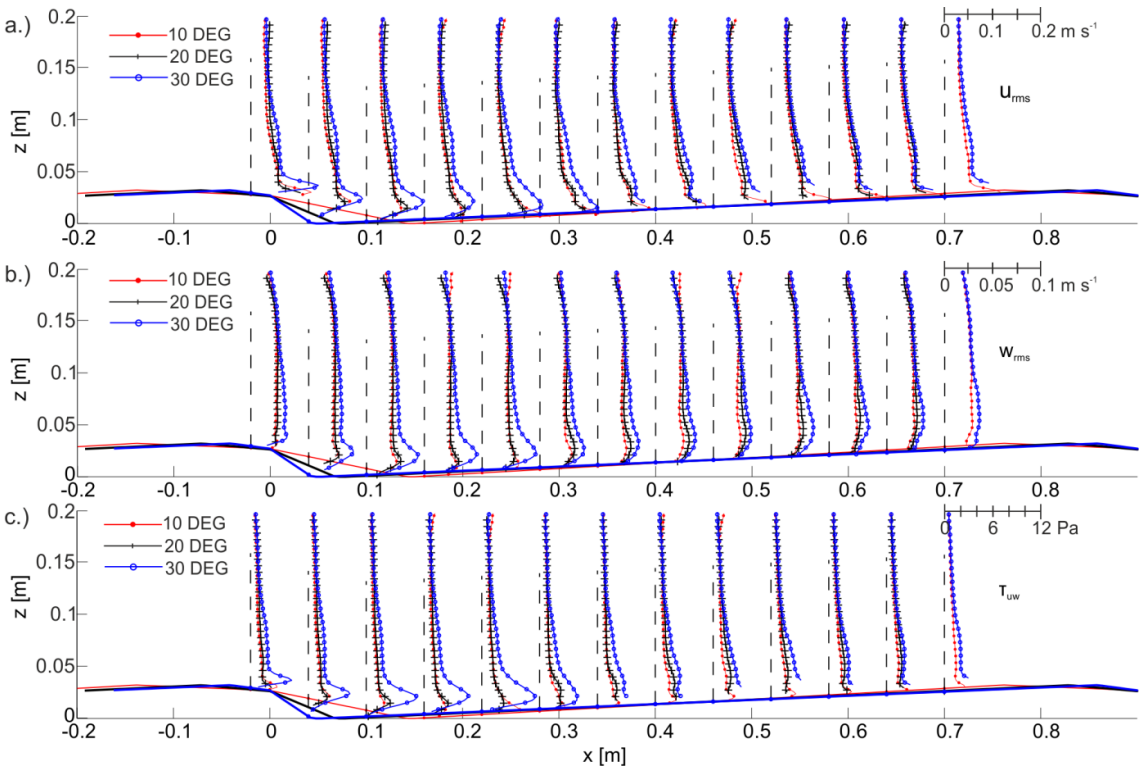

Figure 4.6. Vertical profiles of root-mean-square values of (a) streamwise velocity (u_{rms}) [m s^{-1}] and (b) vertical velocity (w_{rms}) [m s^{-1}] and (c) Reynolds shear stress (τ_{uw}) [Pa] from PIV measurements for all dune configurations.

Contours of (TKE_{uw}) for all experiments similarly show elevated values along the shear layer in the dune lee and in the downstream wake (**Figure 4.7**). (TKE_{uw}) measured by the PIV consistently gives smaller values (up to 2 Pa) than LDV and 2DV model simulations. (TKE_{uw}) is examined in detail to derive wake characteristics as dependent on the lee slope. Whereas otherwise noted, statistics are derived from the model output.

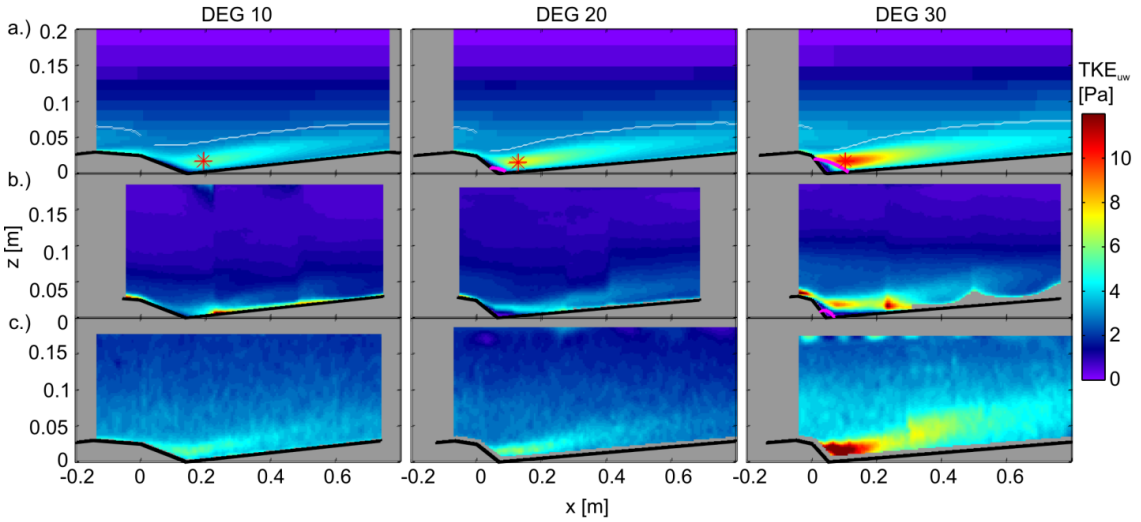

Figure 4.7. Turbulent kinetic energy (TKE_{uw}) from (a) 2DV model and (b) and PIV and (c) LDV for the three dune configurations (left to right: 10°, 20° and 30° lee-slope. The vertical extent of the wake is indicated by white line (see definition in text) and the location of maximum (TKE_{uw}) is indicated by a red asterisk in (a).

Overall (TKE_{uw}) is largest downstream of the 30° dune and decreases with lower lee-slope, indicating higher levels of turbulence in the wake of the steeper dune. The location of maximum (TKE_{uw}) in respect to the brink point is shifted downstream with lower lee-slopes (4.1 H, 5 H and 7.7 H for 30°, 20° and 10°, respectively), but nearly the same in respect to the dune trough (2.16 H, 2.16 H and 1.92 H for 30°, 20° and 10°, respectively). Maximum (TKE_{uw}) above the 10° dune is 54% of the maximum (TKE_{uw}) for the 30° dune. Maximum (TKE_{uw}) for the 20° dune is 71% of that above the 30° dune. Inside the wake (TKE_{uw}) decreases from a maximum inside the center outward.

The vertical extent of the wake was defined as the height above the bed at which the vertical profile of (TKE_{uw}) adapts a linear form towards the water surface and is marked in **Figure 4.7** and **Figure 4.8**. For all dune configurations the effect of the upstream wake is evident by an inflection of the (TKE_{uw}) profiles. The vertical extent of the wake for all experiments shows no marked differences; the influence of the upstream wake on the (TKE_{uw}) profiles however, is evident further downstream over the steeper dune. This suggest that the higher level of energy present in the wake of the steeper dunes significantly influences the turbulence structure of the downstream dune, while the effect in the vertical seems similar for all dune configurations.

At a distance downstream, (TKE_{uw}) values close to the bed increase marking the development of the IBL on the downstream stoss side. The location where the (TKE_{uw}) in the IBL overcomes the (TKE_{uw}) in the overlying wake occurs further downstream for the steeper dune due to the overall higher turbulence in the wake (26.6 *H*, 22.3 *H*, 21.1 *H* from brink for 30°, 20° and 10° dunes, respectively). Similarly to turbulence intensities and Reynolds shear stress, reduced (TKE_{uw}) occurs immediately above the dune lee-slopes. Interestingly, the small zone of increased (TKE_{uw}) extending from the dune brink point is independent on the location and presence of the separation point, which was shown to be situated below the brink point in the previous section.

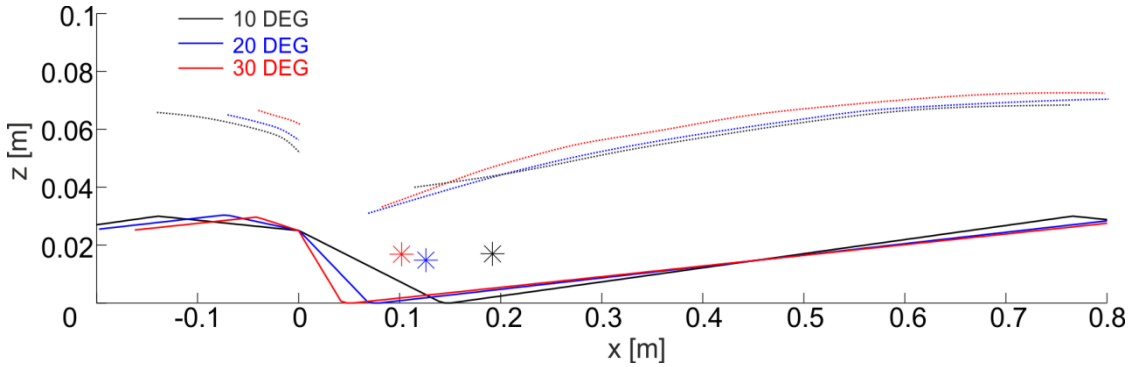

Figure 4.8. Extent of the wake downstream of the dunes and location of maximum turbulent kinetic energy in the dune lee-side for all experiments. Asterisks mark the location of maximum (TKE_{uw}) and thin lines depict the vertical extent of the wake along the dune as estimated from the 2DV model. Color-coding marks the 10° (black), 20° (blue) and 30°(red) dunes.

4.4. Discussion

4.4.1. Evaluation of the combined PIV, LDV and 2DV model approach

The above described results demonstrate the remarkable agreement of the three approaches (PIV, LDV and 2DV model) in determining some of the time-averaged flow and turbulence quantities associated with dunes of varying lee-slopes. However, there are also subtle differences; these differences are linked to each of the approaches current limitations.

Regarding the 2DV modeling approach there are two main limitations. Firstly, the Delft3D model solves the Reynolds-averaged Navier-Stokes (RANS) equations through a turbulence closure scheme. This entails that a parameterizations is used to model turbulence. The various scales of turbulent motions, such as the macroturbulence observed downstream of dunes [*Jackson*, 1976; *Babakaiff and Hickin*, 1996; *Best*, 2005a], are not resolved. Previous studies suggested that RANS models show inaccuracies regarding turbulence quantities [*Stoesser et al.*, 2008]. However, previous applications have shown that the model performs well in examining the characteristics of flow separation zones and wake layer downstream of dunes, provided a careful calibration was undertaken [*Lefebvre et al.*, sub.]. A detailed sensitivity study was therefore carried out beforehand (not shown), calibrating the model against the laboratory data while varying the grain roughness and eddy viscosity.

The second limitation is based on the choice of a 2-dimensional model domain. This implies that any variations in spanwise velocity are neglected. Secondary circulation associated with 3-dimensional bedforms was shown to influence flow and turbulence characteristics above bedforms [*Maddux et al.*, 2003; *Parsons et al.*, 2005; *Venditti*, 2007]. The presence of secondary circulation in our laboratory measurements might therefore possibly cause deviations between modeled and measured velocities.

Regarding the laboratory measurements, some difficulties were encountered during processing. At some locations (e.g., close to the bed at the lower stoss) LDV and PIV measurements show deviations greater or of the same order as modeled values. Time series of vertical velocities of the LDV measurements for the 10° and 20° dunes proved to contain a high level of noise after preprocessing, an issue that requires further attention. PIV images close to the bed also showed high fluctuations in single velocity measurements, possibly due to the high light reflection close to the bed. Furthermore, some inconsistencies still remain at the margins of combined PIV frames and LDV measurement sections.

Considering these issues, the agreement between both measuring techniques and the model for the streamwise and vertical velocity component and TKE_{uw} are considered satisfactory.

4.4.2. Flow separation and shear layer characteristics

Flow separation is caused by the pressure differential and resulting velocity gradient downstream of dune crests. Calculation of the vertical gradient of time-averaged streamwise velocity ($d\bar{u}\ dz^{-1}$) was performed by fitting a third-order polynomial to the modeled velocity data (**Figure 4.9a-c**). High velocity gradients occur above the slope leading from the crest to the brink point and are of similar magnitude for the three dune configuration. Following the step in topography at the brink point, this region of high velocity gradient is detached from the bed, the gradient decreasing outward from its center located just downstream of the brink point. The velocity gradient at the brink is of similar magnitude for the 10° and 20° dunes, but slightly higher for the 30° dunes. The inclination of the region of high velocity gradient downstream of the dune brink is increasing with lower lee-slopes above our dune configurations. This results in high velocity gradients very close to the bed above the 10° dunes and furthest from the bed for the 30° dunes. At approximately $x = 10\ H$ increasing velocity gradients close to the bed denote the development of the IBL.

Our results suggest that a shear layer develops downstream of the brink point with similar characteristics for all lee-slopes observed here, departing from a classical wall-bound shear layer. The development of a 'free' shear layer downstream of angle-of-repose dunes is well-known [*Nelson et al.*, 1993; *Bennett and Best*, 1995; *Venditti and Bennett*, 2000; *Wren et al.*, 2007]. High velocity gradients, possibly initiating an internal shear layer, have also been observed downstream of low-angle dunes [*Best and Kostaschuk*, 2002; *Sukhodolov et al.*, 2006]. Previous studies have suggested that use of flow reversal and the establishment of a flow recirculaton cell as an indicator of departure from wall-bound flow, might not be aplicable for natural dunes with lower lee-slopes [*Maddux et al.*, 2003; *Sukhodolov et al.*, 2006]. Instead, the development of a new wall-bound layer (IBL) on the downstream stoss, is believed to be indicative [*Sukhodolov et al.*, 2006]. Above the 10° dunes in our study, velocity gradients close to the bed decrease significantly downstream of the dune trough, and increase once the IBL is established.

A flow seapration zone, defined by the extent of the flow recirculation cell, is estabished when flow in the region enclosed by the shear layer and the bed decelerates sufficiently. Above the 10° dunes the region of high velocity gradient is situated immediately above the bed, flow deceleration is small. Above the 20° dunes, a small zone of flow recirculation develops at the foot of the dune, beneath the region of high velocity gradients. In case of the 30° dunes, the shear layer is less inclined and the recirculation cell develops a short distance below the brink point.

The inclination of the shear layer appears to depend on the bed slope leading from the dune crest to the brink point. This has been acknowledged in previous studies who found a dependency of the length of the flow separation zone on the local bed slope [*Paarlberg et al.*, 2007]. The highest bed slope at the brink point (6.6°) occurs for the 30° dunes. For natural dunes this slope decreases with lee-slope, as is commonly observed by a rounding of the area around the dune crest [e.g., *Villard and Kostaschuk*, 1998]. In such cases the simultaneous decrease in bed slope at the crest and on the lee-side is therefore thought responsible for the progressive convergence of shear layer and bed slope, thereby reducing recirculation cell development.

It shall be noted, that the above described shear layer and flow recirculation cell characteristics are derived from time-averaged data only. Previous studies have shown that flow reversal can also occur intermittently [*Carling et al.*, 2000b; *Best and Kostaschuk*, 2002] and that the shear layer is highly dynamic [*Nezu and Nakagawa*, 1993; *Schmeeckle et al.*, 1999].

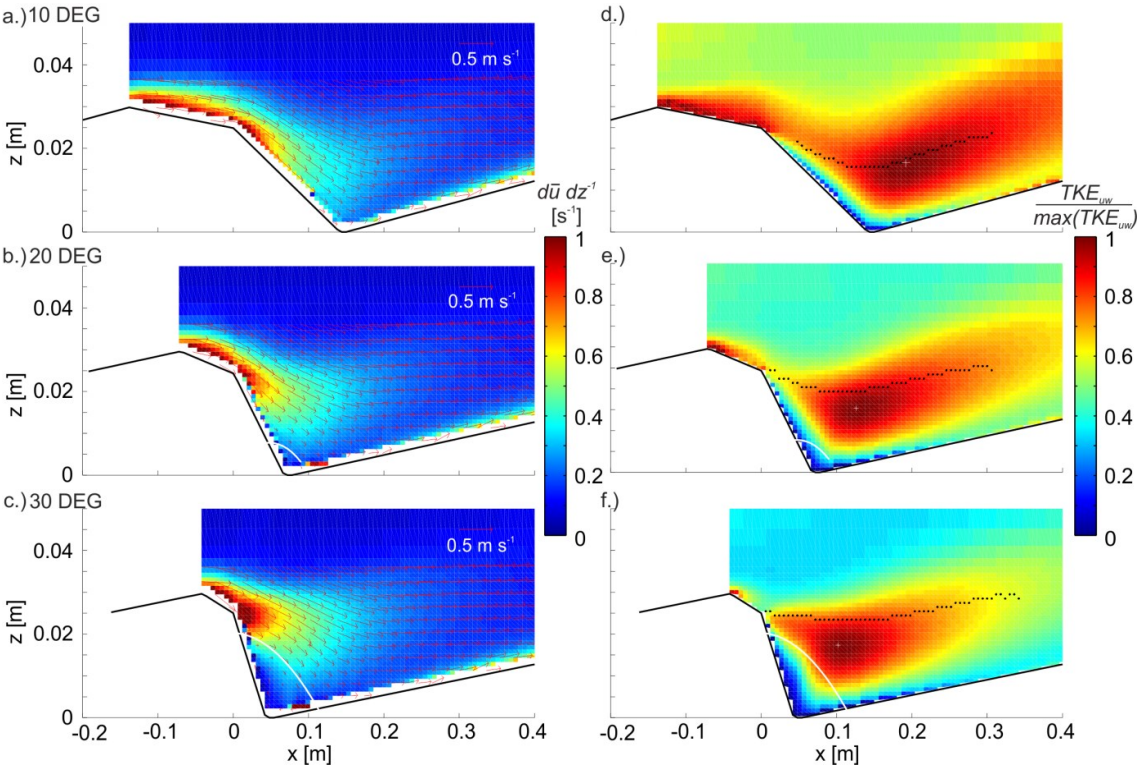

Figure 4.9. Vertical velocity gradient of modeled time-averaged streamwise velocity ($d\bar{u}\ dz^{-1}$) [s^{-1}] for (a) 10° dune, (b) 20° dune and (c) 30° dune. Normalized TKE_{uw} downstream of (d) 10° dune, (b) 20° dune and (c) 30° dune. The extent of the recirculation cell [*Paarlberg et al.*, 2007] is shown where present (white line). Arrows in (a-c) display velocity magnitude and direction. Black line in (d-f) shows the location of maximum velocity gradient.

4.4.3. Turbulence production

The high velocity gradient downstream of the dune brink point leads to the production of turbulence along the shear layer. This causes a momentum defect as well as high turbulence

intensity and shear stresses to be advected downstream in the wake above all dune configurations. The magnitudes of turbulence intensities, Reynolds shear stresses and overall turbulent kinetic energy are highest above the 30° dunes in the presence of permanent flow reversal. Lowest turbulence parameters occur in the absence of permanent flow reversal. **Figure 4.9d-f** displays the turbulent kinetic energy normalized by its maximum value (TKE_{uw} $\max(TKE_{uw})^{-1}$) for each dune configuration. Furthermore, the extent of the recirculation cell and the position of the maximum velocity gradient downstream of the brinkpoint are indicated. The region of highest turbulent kinetic energy above the 10° dunes follows the highest velocity gradient and decreases outward. With increasing size of the flow recirculation cell, the region of highest energy is situated lower beneath the line marking the highest velocity gradient. This suggests that with increasing lee-slope the presence of flow reversal significantly alters the turbulence generation along the shear layer.

Previous studies have shown that the wake downstream of bedforms with low lee-slopes is characterized by lower levels of turbulence compared to angle-of-repose dunes [*Sukhodolov et al.*, 2006; *Best and Kostaschuk*, 2002]. While turbulence production in the later case is attributed to flow separation processes, above low-angle dunes turbulence production has been attributed to intermittent flow separation and/or vortex generation similar to plane-mixing layer turbulence generation [*Best and Kostaschuk*, 2002]. Though we cannot comment on the intermittency of flow separation, our results confirm that in the absence of a permanent recirculation cell, turbulence is generated in the area of highest velocity gradient. This turbulence production differs from turbulence produced in boundary-layer flows. In the presence of permanent flow recirculation, turbulence generated in regions of high velocity gradient is believed to interact with the flow in the recirculation cell and the bed in the region of flow reattachment resulting in significantly enhanced turbulence levels for steeper dunes.

Interestingly, the vertical extent of the wake is similar for all 3 dune configurations, indicating that the degree of influence of the form-induced flow region onto the outer flow in a time-averaged sense is independent of the overall turbulence level within the wake. However, the horizontal extent of the wake is greater for steeper lee-slopes and causes the appearance of a stacked-wake flow structure [*Sukhodolov et al.*, 2006]. This implies that turbulent kinetic energy is dissipated more rapidly in the vertical direction for dunes with steeper lee-slopes. Possible reasons for this might be an enhanced interaction of larger scale vortices with each other or the developing internal boundary layer or increased upward translation of vortices to dissipate as boils [e.g., *Matthes*, 1947; *Jackson*, 1976; *Best*, 2005a] at the surface. However, this cannot be confirmed in our time-averaged observations.

4.4.4. Impact of the lee-slope on hydraulic roughness

Dunes respond to the flow as roughness elements, increasing the drag exerted by the bed on the overlying flow [e.g., *Einstein and Barbarossa*, 1952; *Vanoni and Brooks*, 1957; *Engelund and Hansen*, 1967]. Drag implies the expenditure of mean flow momentum for turbulence production, which for dunes is mostly associated with flow separation in the dune lee [*Huthoff*, 2012]. Form roughness was shown to depend on dune morphology, i.e. dune height, aspect ratio and shape. These factors are commonly used to predict form roughness through empirical formulations [e.g., *van Rijn*, 1993; *Bartholdy et al.*, 2010]. The effect of the lee-slope therein is included in the parameterization of dune shape. Ogink [1988] as cited by van Rijn [1993] observed a reduction of form roughness for lower lee-slopes. He concluded that the flow separation process and energy expenditure was less important above mild lee-slopes than for dunes with steeper slopes.

Estimates of hydraulic roughness were derived from the modeled velocity data through application of the depth-slope product: The total shear stress (τ_T) and shear velocity (u_*) are computed via

$$\tau_T = \rho_w g\, h\, S \qquad (4.8)$$

$$u_* = (\tau_T\, \rho_w^{-1})^{0.5} \qquad (4.9)$$

Where S is the energy slope calculated from a linear fit through the water surface elevation [*Lefebvre et al*., sub.]. Roughness height (k_s) is related to the depth-averaged velocity (U) via the Manning Chèzy coefficient

$$U\,(h\,S)^{-0.5} = C = 25\,(h\,k_s^{-1})^{1/6} \qquad (4.10)$$

and roughness length (z_0) is related to roughness height (k_s) via $z_0 = 30^{-1}\, k_s$ [*van Rijn*, 1993].

Furthermore, total shear stress was determined by fitting log-linear segments to the spatially-averaged velocity profiles [*Smith and McLean*, 1977; *Kostaschuk and Villard*, 1996b; *Villard and Kostaschuk*, 1998; *Lefebvre et al.*, 2013a]. In this method, it is assumed that the spatially-averaged velocity profile in the outer flow layer follows a logarithmic velocity distribution representing the effect of combined grain and form roughness that can be approximated by the Kármán-Prandl Law of the Wall:

$$\bar{u}(z) = \frac{u_*}{\kappa} ln \frac{z}{z_0} \qquad (4.11)$$

where (z) is the height above bed and (κ) is the von Kármán constant (0.41). Spatially-averaged velocity profiles were derived by averaging the modeled time-averaged velocity ($\bar{u}$) over lines of equal height above the bed (z) normalized by the total water depth (h) (**Figure 4.10**). Iterative regression was performed to determine the best fit and converging height of log-linear

segments. Results show that the velocity profiles above all three dunes are best described by two log-linear segments converging at a normalized height of z_c = 0.08 – 0.09. This location coincides with the maximum of (TKE_{uw}) and (τ_{uw}) determined from modeled and measured data.

Table 4.2 summarizes the total shear stress, shear velocity, roughness height and length derived for the three dune designs (Suffix DSP denotes derivation through the depth-slope product) and total shear stress, shear velocity and roughness length together with the coefficient of determination and statistical errors [*Wilkinson*, 1984] associated with the application of the Law of the Wall (LoW).

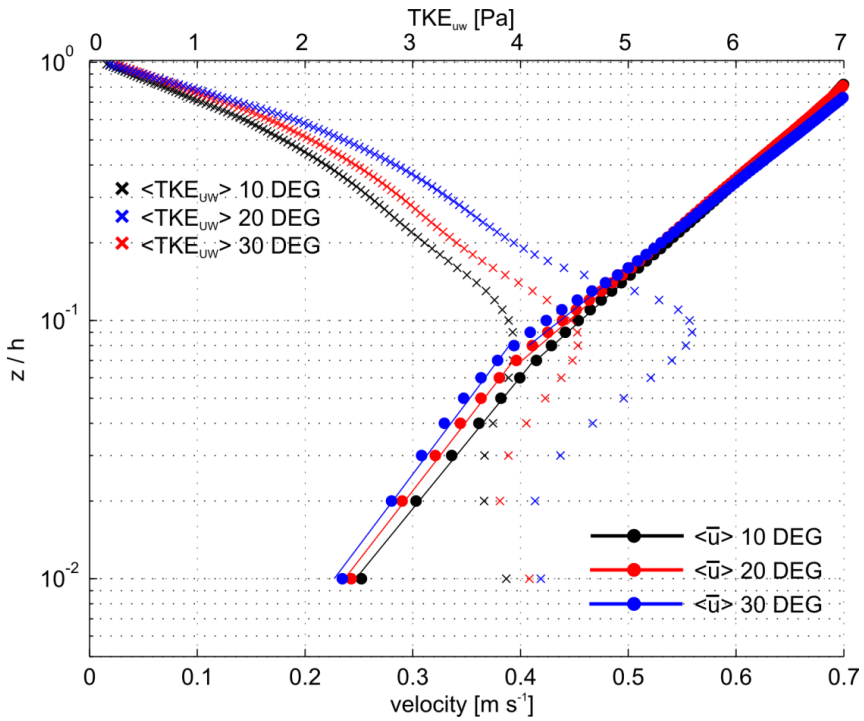

Figure 4.10. Spatially-averaged velocity profiles across the measurement dune from modeled time-averaged velocity. The best fit regression lies at z/h = 0.08 for the 10° and 20° dunes and at z/h = 0.09 for the 30° dune and coincides with the maximum in the spatially-averaged (TKE_{uw}) profile.

Both methods show an increase in hydraulic roughness parameters with increasing lee-slope. Shear stresses estimated by the depth-slope-product are ~75%, roughness length and height are ~35% of that determined by the spatially-averaged velocity profiles. McLean et al. [1999] indicated difficulties in the application of the LoW-method in the presence of stacked-wake flows, such as present here. Nevertheless, the spatially-averaged profiles indicate that a kink in the velocity profile occurs approximately at the same height above the bed for all 3 dune shapes. These results agree with our findings that the vertical extent of the wake and thus form-induced roughness layer is independent of the lee-slope. Smith and McLean [1977] found a larger upper log segment for dunes with low lee-slope, which were also smaller in height. Wake extent might therefore dependent on dune height.

Table 4.2. Estimated total shear stress (τ_T) [Pa], shear velocity (u_*) [m s^{-1}], roughness length (z_0) [m] and roughness height (k_s) [m] derived through the depth slope product (*DSP*) and spatially-averaged velocity profile (*LoW*). Statistical errors and coefficient of determination (R^2) for LoW estimates are given.

	10 DEG		20 DEG		30 DEG	
	DSP	LoW (R^2 = 0.9990) z_c = 0.08	DSP	LoW (R^2 = 0.9991) z_c = 0.08	DSP	LoW (R^2 = 0.9985) z_c = 0.09
τ_T [Pa]	1.6162	2.1623	1.8224	2.3814	1.9963	2.7668
u_* [m s^{-1}]	0.0402	0.0465	0.0427	0.0488	0.0447	0.0526
(*error*)		*(0.0003)*		*(0.00029)*		*(0.00042)*
z0 [m]	0.00014	0.00040	0.000203	0.00053	0.00026	0.00073
(*error*)		*(0.00002)*		*(0.00002)*		*(0.00004)*
k_s [m]	0.0042	0.0120	0.0061	0.0159	0.0079	0.0237

Huthoff [2012] related the hydraulic roughness above dunes to the size of the wake and integral turbulence scale within. His formulation was based on the observation that the integral length scale of turbulence above dunes with a lee-slope of 30° scales with dune height and water depth [*Venditti and Bennett*, 2000]. Our results suggest that, while the extent of the wake scales with dune height, integral turbulence scales decreases with decreasing lee-slope. This conclusion is supported by the work of Best and Kostaschuk [2002] who suggested smaller scales of turbulence production above low-angle dunes.

4.5. Conclusions

A combined laboratory study and numerical modeling application was used to investigate the mean flow and turbulence parameters of dunes with varying lee-slope angles. The results indicate that intermediate lee-slopes (10-20°) are characterized by transitional flow features leading to differences in flow and turbulence features above angle-of-repose and low-angle dunes.

- A permanent flow recirculation cell was observed downstream of the 30° dunes. In case of the 20° dunes the model predicts a permanent recirculation cell, smaller in extent compared to the 30° dunes, located at the dune toe. There is no flow reversal evident in the laboratory data. A permanent flow recirculation cell is absent for the 10° dunes.

- A layer of strong velocity gradient exists downstream of the dune brink point regardless of the angle of the lee-slope. The curvature of the layer is believed to depend on the slope of the bed at the brink point. For 30° dunes this layer is located some distance away from the bed and a permanent flow recirculation cell forms on the lee-slope. For smaller lee-slopes, the shear layer approaches the bed, thereby decreasing the size of the flow recirculation cell until it disappears.

- Turbulence production in the shear layer induces a wake that is advected downstream. The vertical wake extent is independent of the lee-slope, but possibly dependent on dune height. The level of turbulent kinetic energy, Reynolds stresses and turbulence intensities within the wake decreases with lee-slope. This is attributed to a difference in scale of turbulence produced along the shear layer in the dune lee, caused by a decrease in flow unsteadiness as the shear layer approaches the lee-slope. An internal boundary layer develops downstream of the dune stoss marking the reappearance of wall-bound shear flow.

- Hydraulic roughness decreases with decreasing lee-slope. This is related to a decrease in turbulence production and therefore energy expenditure downstream of dunes with lower lee-slopes. Estimates of hydraulic roughness based on the vertical extent of the wake or dune height might be misleading.

CHAPTER 5 - SYNTHESIS AND CONCLUSION

5.1. SHORT SUMMARY

The aim of this thesis was to investigate the formation and occurrence of macroturbulent flow structures and their coupling to suspended sediment transport downstream of natural bedforms. The research is based on field surveys combining ship-based observations and lander-based moorings using acoustic Doppler current profilers and optical measurement probes. In addition, a laboratory flume study over fixed bedforms was carried out and combined with a 2DV numerical model.

In **Chapter 2** the frequent occurrence of large (10-20 m) sediment-laden clouds at the water surface of the Elbe Estuary was examined. These clouds occur during accelerating ebb currents and were found to be linked to macroturbulent structures originating in the lee-side of compound bedforms at the river bed. Our estimates of cloud frequency are within the range of previous data on macroturbulence characteristics associated with turbulence production from flow separation zones downstream of bedforms. Sediment transport in this environment can be characterized by two separated systems: (1) bed-load transport of sandy material (~500 μm) that controls the geometry and dynamics of compound bedforms and (2) cyclic transport of a fine sediment mode (~50 μm) characterized by intermittent suspension through macroturbulence and deposition in bedform troughs around slack water.

The temporal restriction of the Elbe suspension clouds to a particular tidal stages led to the investigation of the effect of (1) tide-induced flow-reversal above asymmetric bedforms and (2) bedform superimposition on the production of macroturbulence and coupling to suspended sediment transport. In **Chapter 3**, data from a field campaign to a tidal inlet in the Danish Wadden Sea are shown. Here, water-depth scale macroturbulence develops above the primary bedforms and governs suspended sediment transport when the mean tidal current direction and bedform orientation are aligned. Generation of macroturbulence is associated with the development of flow separation zones in the steep leeside (16 - 20°) of the primary bedform. When tidal current and bedform orientation are opposed, water-depth scale macroturbulence is absent due to the low velocity gradient above the now gentle-sloping hydraulic lee-side (~2°) and absence of flow separation. Turbulence generation is attributed to the smaller superimposed secondary bedforms that reverse direction with each tidal phase.

As the bedform lee-slope was shown to be an intrinsic parameter regarding flow and macroturbulence above bedforms, further investigation on this matter is presented in **Chapter 4**. A laboratory study combined with a 2DV numerical model examines the influence of the

bedform lee-slope on the time-averaged flow field, turbulence and hydraulic roughness. Three fixed bedform prototypes of different geometries were prepared with lee-slopes of 10°, 20° and 30°. Results show that strong velocity gradients produce a shear layer even in the absence of flow separation in the lee-side of bedforms with low lee-angle. Turbulence produced along the shear layer is advected in form of a downstream wake in case of all three bedform configurations. The vertical extent of the wake is independent of the lee-slope. Turbulent kinetic energy, Reynolds stresses and turbulence intensities within the wake structure decrease with decreasing lee-slope, therefore causing smaller hydraulic roughness for lower lee-slopes.

5.2. Conclusions

This thesis has exemplified the use of multiple research approaches in examining the relationship between bedform morphology, macroturbulence and suspended sediment transport. The work has highlighted important differences in these phenomena due to the variety of bedform morphologies and range of transport conditions occurring in natural environments. It has furthermore demonstrated how laboratory and numerical investigations can be successfully applied to complement field measurements. In general, this study stresses the need to further study suspended sediment transport processes in unsteady, turbulent flow regimes. In the following our findings are presented, based on the objectives laid out in the introduction.

(1) Presence / absence of flow separation and shear layer characteristics downstream of bedforms

Both Elbe and Knudedyb compound bedforms have lee-slopes below 20° and fall in the intermediate range of lee-slopes for which it is unknown whether flow separation occurs at all, only intermittently, or whether it can be considered permanent. Evidence of flow separation in the form of flow reversal was solely found downstream of the largest bedforms in the Knudedyb tidal inlet. The laboratory study suggests that flow separation zones might be present but decrease in size for intermediate lee-slope angles. We have shown that flow separation might not be initiated at the bedform brink point, but might solely be present on the lower lee-slope. The zones of flow reversal might therefore be smaller than expected and located close to the bed, rendering their detection in the field even more difficult.

The laboratory flume study showed that a shear layer is present also in the absence of flow separation and is in all cases initiated at the dune brink point. Turbulence is produced along this layer and is observed downstream of the bedform in form of macroturbulent structures in case of both field studies, in the Elbe and the Knudedyb tidal inlet. Our findings suggest that predictions of turbulence production and hydraulic roughness should be based on the rate of flow expansion and therefore velocity gradient downstream of bedforms rather than estimates of flow separation.

(2) Occurrence and origin of macroturbulence above natural bedforms and
(3) Effect of flow unsteadiness and compound morphology on macroturbulence production

The occurrence of water depth-scale macroturbulence above compound bedforms is restricted to tidal stages when tidal current direction and primary bedform orientation are aligned. Furthermore, in the Elbe Estuary and in the Knudedyb tidal inlet, a velocity threshold needs to

be overcome marking the appearance of macroturbulence during the accelerating ebb tide. Our results demonstrate that flow unsteadiness has important effects on macroturbulence production. Such flow unsteadiness is not only present in tidal environments but also during floods.

The origin of macroturbulence was shown to be located in the bedform lee-side in the region of high velocity gradients. In both field studies, observed macroturbulent frequencies fall into the Strouhal range of previously observed macroturbulence above bedforms associated with flow separation zones. However, we have shown that scale and frequency of macroturbulence depends on bedform geometry, particularly the bedform lee-slope. Currently, accurate predictions for this relationship are not available.

(4) Coupling of macroturbulence and suspended sediment transport

Our studies have shown that macroturbulent flow structures at both field sites are responsible for the suspension and upward transfer of fine sediment. This implies that the presence and scale of macroturbulence plays a dominant role in the vertical mixing of sediment in suspension. Results from both field studies have shown that these processes are highly variable between ebb and flood tide, and - due to flow unsteadiness - even during a tidal cycle.

Furthermore, we have demonstrated that the characteristics and availability of fine sediment has an important effect on the dispersion of sediment in the upper water column. The separation of the fine sediment fraction from the coarser bed material in the Elbe Estuary, results in the formation of distinct ‘turbidity clouds’. The separation is caused by the combination of high concentrations of fine material and the presence of biogenic material, causing the sediment to pertain cohesive properties. This observation is typical for estuarine conditions where high salinity gradients are coupled to high productivity. During slack water, increased flocculation and settling induce the formation of ephemeral fluid mud layers, which are entrained during accelerating currents. By contrast, in the Knudedyb tidal inlet, although the grain size distribution of material in suspension is similar to the Elbe, such cohesive properties are most probably absent. Sediment dispersion once transported to the upper water column is enhanced in the Knudedyb suspension structures compared to the Elbe clouds.

We have shown that under tidal-induced flow reversal and with varying characteristics of fine sediments, suspended sediment transport is a complex phenomenon that currently lacks adequate description. In case of the Knudedyb tidal inlet, suspended sediment transport during the ebb was shown to actively influence bedform morphology and possible add to the net ebb-directed migration of compound bedforms, while little morphological changes occurred during the flood period. In general, neglection of the observed processes might severely under- or overestimate sediment transport budgets in tidal inlets and estuaries.

(5) Implications for hydraulic roughness

Turbulence production associated with compound bedforms was shown to vary from one tidal cycle to the other, causing variable hydraulic roughness between ebb and flood tide. Such tidal-induced variation in hydraulic roughness is not accounted for in current morphodynamic models. Hydraulic roughness was further shown to depend on the lee-slope of bedforms, which show a great variation in the natural environment. Thus, there exists a great need to implement roughness in a non-uniform and non-constant form into current numerical models. This description should consider not only changes in water level, and bedform geometries such as height and length, but also the relative orientation of bedform and flow direction and lee-slope characteristics.

5.3. Suggestions for future research

The deposition-entrainment-cycle of fluid mud described in **Chapter 2** raises several questions, for example, how the location of the turbidity maximum of the Elbe Estuary would influence the presence of fluid mud in the observed compound bedform field; and how that in turn would alter formation of macroturbulence leading to the observed turbidity clouds. Here, dedicated field campaigns taking into account variations in river discharge are required.

In **Chapter 3**, it was suggested that the transport of sediment in suspension plays a dominant role in compound bedform morphology and dynamics in the tidal inlet. A detailed study, combining a high-resolution bathymetric survey with measurements of suspended sediment in the water column would allow volumetric calculations of changes in bedform morphology and amount of sediment in suspension. In doing so, our hypothesis regarding the differences in ebb and flood sediment transport could be validated.

In **Chapter 4,** it has been proposed that shear layer characteristics downstream of bedforms depend not only on the lee-slope but also on the angle leading towards the brink point. Furthermore, it has been shown previously [*Lefebvre et al*., sub] that the downstream stoss significantly influences the extent of the flow separation zone and the overlying wake layer. It is recommended to examine the relationships behind these phenomena in more detail, so that applicable formulations can be put forward. It would also be interesting to see how superimposed secondary bedforms on the stoss-side influence the flow features of the primary bedform.

In general, the quantification of scale and frequency of macroturbulent structures and coupling to suspended sediment transport from field measurements is still limited, particularly regarding moving boat measurements. Deployment of lander-based stationary observation systems at several strategic locations in the bedform field might overcome these shortcomings. For one, upward-looking ADCPs have proven well to examine the translation of macroturbulence and suspension structures through the water column and could thus be used to examine changes in the flow structure or suspended sediment with downstream distance. Furthermore, near-bed measurements from lander-based systems providing high-resolution 3D velocity and suspended sediment concentration could aid in the understanding of the mechanisms behind sediment entrainment by these macroturbulent structures. Detailed laboratory studies should complement this research by examining macroturbulence over a mobile bed. Such facilities should be able to simulate tidal hydrographs including flow reversal, and be equipped with high-resolution instrumentation able to detect the 3-dimensional nature of the macroturbulence. Recent Large eddy simulation (LES) modeling advances of 3-dimensional macroturbulence downstream of bedforms are also promising.

References

Abdalla, I. E., Z. Yang, and M. Cook (2009). Computational analysis and flow structure of a transitional separated-reattached flow over a surface mounted obstacle and a forward-facing step. *International Journal of Computational Fluid Dynamics*, *23*(1), 25–57, doi:10.1080/10618560802566246.

Adrian, R. J. (2007). Hairpin vortex organization in wall turbulence. *Physics of Fluids*, *19*(4), 041301, doi:10.1063/1.2717527.

Ainslie, M. A., and J. G. McColm (1998). A simplified formula for viscous and chemical absorption in sea water. *Journal of the Acoustic Society of America*, *103*(3), 1671-1672.

Allen, J. R. L. (1982). Sedimentary structures, their character and physical basis, Elsevier Science, New York, USA.

Antonia, R. A. (1981). Conditional sampling in turbulence measurements. *Annual Review of Fluid Mechanics*, *12*, 131–156.

Anwar, H. O. (1981). A study of the turbulent structure in a tidal flow. *Estuarine, Coastal and Shelf Science*, *13*(4), 373–387, doi:10.1016/S0302-3524(81)80035-7.

Ashley, G. M. (1990). Classification of large-scale subaqueous bedforms: a new look at an old problem. *Journal of Sedimentary Petrology*, *60*(1), 160–172.

Baas, J. H., and J. L. Best (2008). The dynamics of turbulent, transitional and laminar clay-laden flow over a fixed current ripple. *Sedimentology*, *55*(3), 635–666.

Babakaiff, C. S., and E. J. Hickin (1996). Coherent flow structures in Squamish River Estuary, British Columbia, Canada. In *Coherent Flow Structures in Open Channels*, edited by P. J. Ashworth, S. J. Bennett, J. Best, and S. J. McLelland, pp. 321–342, Wiley & Sons, Chichester.

Badesab, F., T. von Dobeneck, K. R. Bryan, H. Müller, R. M. Briggs, T. Frederichs, and E. Kwoll (2012). Formation of magnetite-enriched zones in and offshore of a mesotidal estuarine lagoon: An environmental magnetic study of Tauranga Harbour and Bay of Plenty, New Zealand. *Geochemistry, Geophysics, Geosystems*, *13*(6), 1-20, doi:10.1029/2012GC004125.

Bartholdy, J., B. W. Flemming, V. B. Ernstsen, and C. Winter (2010). Hydraulic roughness over simple subaqueous dunes. *Geo-Marine Letters*, *30*(1), 63–76.

Becker, M., K. Schrottke, A. Bartholomä, V. Ernstsen, C. Winter, and D. Hebbeln (2013). Formation and entrainment of fluid mud layers in troughs of subtidal dunes in an estuarine turbidity zone. *Journal of Geophysical Research: Oceans*, *118*(4), 2175–2187, doi:10.1002/jgrc.20153.

Bennett, S. J., and J. L. Best (1995). Mean flow and turbulence structure over fixed, two-dimensional dunes: implications for sediment transport and bedform stability. *Sedimentology*, *42*(3), 491–513, doi:10.1111/j.1365-3091.1995.tb00386.x.

Best, J., S. Simmons, D. Parsons, K. Oberg, J. Czuba, and C. Malzone (2010). A new methodology for the quantitative visualization of coherent flow structures in alluvial channels using multibeam echo-sounding (MBES). *Geophysical Research Letters*, *37*(6), L06405, doi:10.1029/2009GL041852.

Best, J. (2005a). Kinematics, topology and significance of dune-Related macroturbulence: some observations from the laboratory and field. In *Fluvial Sedimentology VII*, edited by M.D. Blum, S.B. Marriott and S. F. Leclair, Blackwell publishing Ltd., Oxford, UK, doi:10.1002/9781444304350.ch3.

Best, J. (2005b). The fluid dynamics of river dunes: A review and some future research directions. *Journal of Geophysical Research*, *110*(F4), F04S02, doi:10.1029/2004jf000218.

Best, J., and R. A. Kostaschuk (2002). An experimental study of turbulent flow over a low-angle dune. *Journal of Geophysical Research*, *107*(C9), 3135, doi:10.1029/2000jc000294.

Best, J., R. A. Kostaschuk, and P. Villard (2001). Quantitative visualization of flow fields associated with alluvial sand dunes: results from the laboratory and field using ultrasonic and acoustic doppler anemometry. *Journal of Visualization*, *4*(4), 373–381, doi:10.1007/bf03183900.

Best, J. L., P. J. Ashworth, M. H. Sarker, and J. E. Roden (2007). The Brahmaputra-Jamuna River, Bangladesh. In *Large Rivers: Geomorphology and Management*, edited by A. Gupta, pp. 395-430, Wiley & Sons, Chichester.

Bradley, R. W., J. G. Venditti, R. A. Kostaschuk, M. Church, M. Hendershot, and M. A. Allison (2013). Flow and sediment suspension events over low-angle dunes: Fraser Estuary, Canada. *Journal of Geophysical Research: Earth Surface, 118,* 1-17, doi:10.1002/jgrf.20118.

Bradley, R. W. (2012). Coherent flow structures and suspension events over low-angle dunes : Fraser River. MSc Thesis, Department of Geography, Simon Fraser University, Burnaby, Canada.

Bridge, J. S., and J. L. Best (1988). Flow, sediment transport and bedform dynamics over the transition from dunes to upper-stage plane beds: implications for the formation of planar laminae. *Sedimentology*, *35*(5), 753–763.

Carling, P. A., E. Gölz, H. G. Orr, and A. Radecki-Pawlik (2000a). The morphodynamics of fluvial sand dunes in the River Rhine, near Mainz, Germany. I . Sedimentology and morphology. *Sedimentology*, *47*, 227–252.

Carling, P. A., J. J. Williams, E. Gölz, and A. D. Kelsey (2000b). The morphodynamics of fluvial sand dunes in the River Rhine, near Mainz, Germany. II . Hydrodynamics and sediment transport. *Sedimentology*, *47*, 253–278.

Cellino, M., and U. Lemmin (2004). Influence of coherent flow structures on the dynamics of suspended sediment transport in open-channel flow. *Journal of Hydraulic Engineering, 130*, 1077-1088.

Chang, K., and G. Constantinescu (2013). Coherent structures in flow over two-dimensional dunes. *Water Resources Research*, *49*, 1–15, doi:10.1002/wrcr.20239.

Church, M. (2006). Bed material transport and the morphology of alluvial river channels. *Annual Review of Earth Planetary Science*, *34*, 325–354.

Coleman, S. E., and V. I. Nikora (2011). Fluvial dunes: initiation, characterization, flow structure. *Earth Surface Processes and Landforms*, *36*(1), 39–57, doi:10.1002/esp.2096.

Coleman, J. M. (1969). Brahmaputra river: Channel processes and sedimentation. *Sedimentary Geology,* 3, 129-239.

Czuba, J. A., K. A. Oberg, J. L. Best, D. R. Parsons, S. M. Simmons, K. K. Johnson, and C. Malzone (2011). Temporal characteristics of coherent flow structures generated over alluvial sand dunes, Mississippi River, revealed by acoustic Doppler current profiling and multibeam echo sounding. *RCEM*, Beijing, 6-8 September 2011, 1-6. http://hydroacoustics.usgs.gov/publications/Final-RCEM-ADCP-Dunes.pdf.

Dade, W. B., and P. F. Friend (1998). An empirical model of subcritical bedform migration. *The Journal of Geology*, *106*(6), 661–676.

Dantec Dynamcis (2011). *DynamicStudio v3.20*. Skovlunde, Denmark.

Dalrymple, R. W., and R. N. Rhodes (1995). Estuarine dunes and bars. In *Developmentsin Sedimentology*, Vol. 53, edited by G. M. E. Perillo, Sedimentology, pp. 359–422, Elsevier.

Davies, A. G., L. C. van Rijn, J. Damgaard, J. van de Graaff, and J. S. Ribberink (2002). Intercomparison of research and practical sand transport models. *Coastal Engineering*, *46*, 1–23.

Deines, K. L. (1999). Backscatter estimation using Broadband acoustic Doppler current profilers. *Oceans 99 MTS/IEEE*, pp. 249–253, San Diego, USA.

Deltares (2011). User Manual Delft3D-FLOW.., Deltares, Delft, the Netherlands.

Driver, D. M., H. L. Seegmiller, and J. G. Marvin (1987). Time-dependent behavior of a reattachment shear layer. *American Institute of Aeronautics and Astronautics Journal,* 25, 914-919.

Dyer, K. R. (1997). Estuaries: A physical introduction. Wiley & Sons Ltd., Chichester.

Einstein, H. A., and N. L. Barbarossa (1952). River channel roughness. *Transactions of the American Society of civil Engineers*, *117*(1), 1121–1132.

Engelund, F., and J. Fredsoe (1982). Sediment ripples and dunes. *Annual Review of Fluid Mechanics*, *14*(1), 13–37.

Engelund, F., and E. Hansen (1967). Monograph on sediment transport in alluvial streams. Teknisk forlag, Copenhagen.

Ernstsen, V. B., R. Noormets, C. Winter, D. Hebbeln, A. Bartholomä, B. W. Flemming, and J. Bartholdy (2006). Quantification of dune dynamics during a tidal cycle in an inlet channel of the Danish Wadden Sea. *Geo-Marine Letters*, *26*(3), 151–163, doi:10.1007/s00367-006-0026-2.

Fernandez, R., J. Best, and F. López (2006). Mean flow, turbulence structure, and bed form superimposition across the ripple-dune transition. *Water Resources Research*, *42*, W05406, doi:10.1029/2005WR004330.

Flemming, B. W. (1988). Zur Klassifikation subaquatischer, strömungstransversaler Transportkörper. *Bochumer geologische und geotechnische Arbeiten*, *29*(93-97).

Gabel, S. L. (1993). Geometry and kinematics of dunes during steady and unsteady flows in the Calamus River, Nebraska, USA. *Sedimentology*, *40*(2), 237–269, doi:10.1111/j.1365-3091.1993.tb01763.x.

Gartner, J. W. (2004). Estimating suspended solids concentrations from backscatter intensity measured by acoustic Doppler current profiler in San Francisco Bay, California. *Marine Geology*, *211*(3-4), 169–187, doi:10.1016/j.margeo.2004.07.001.

Gomez, B., R. L. Naff, and D. W. Hubbell (1989). Temporal variations in bedload transport rates associated with the migration of bedforms. *Earth Surface Processes and Landforms*, *14*(2), 135–156.

Gordon, C. M. (1975). Sediment entrainment and suspension in a turbulent tidal flow. *Marine Geology*, *18*, 57–64.

Goring, D. G., and V. I. Nikora (2002). Despiking Acoustic Doppler Velocimeter Data. *Journal of Hydraulic Engineering*, *128*(1), 117–126, doi:10.1061/(ASCE)0733-9429(2002)128:1(117).
Grant, W. D., and O. S. Madsen (1982). Movable bed roughness in unsteady oscillatory flow. *Journal of Geophysical Research*, *87*(C1), 469, doi:10.1029/JC087iC01p00469.
Grabemann, I., J. Kappenberg, J., and G. Krause (1995). Aperiodic variations of the turbidity maxima of two German coastal plain estuaries. *Aquatic Ecology,* 29, 217-227.
Grigoriadis, D. G. E., E. Balaras, and A. A. Dimas (2009). Large-eddy simulations of unidirectional water flow over dunes. *Journal of Geophysical Research*, *114*(F2), F02022, doi:10.1029/2008JF001014.

Hill, D. C., S. E. Jones, and D. Prandle (2003). Derivation of sediment resuspension rates from acoustic backscatter time-series in tidal waters. *Continental Shelf Research,* 23, 19-40.
Hoitink, A. J. F., and P. Hoekstra (2005). Observations of suspended sediment from ADCP and OBS measurements in a mud-dominated environment. *Coastal Engineering,* 52, 103-118.
Holdaway, G. P., P. D. Thorne, D. Flatt, S. E. Jones, and D. Prandle (1999). Comparison between ADCP and transmissometer measurements of suspended sediment concentration. *Continental Shelf Research*, *19*(3), 421–441, doi:10.1016/s0278-4343(98)00097-1.
Huthoff, F. (2012). Theory for flow resistance caused by submerged roughness elements. *Journal of hydraulic research*, *50*(1), 10–17.

Itakura, T., and T. Kishi (1980). Open channel flow with suspended sediment on sand waves. *Third International Symposium on Stochastic Hydraulics*, Tokyo, Japan, 1980, pp. 589-598. International Association of Hydraulic Research.

Jackson, R. G. (1976). Sedimentological and fluid-dynamic implications of the turbulent bursting phenomenon in geophysical flows. *Journal of Fluid Mechanics*, *77*(03), 531–560, doi:doi:10.1017/S0022112076002243.
Julien, P. Y., G. J. Klaassen, W. B. M. Ten Brinke, and A. W. E. Wilbers (2002). Case study: Bed resistance of Rhine River during 1998 flood. *Journal of Hydraulic Engineering*, *128*(12), 1042–1050.

Kadota, A., and I. Nezu (1999). Three-dimensional structure of space-time correlation on coherent vortices generated behind dune crest. *Journal of Hydraulic Research*, *37*, 59–80.
Kappenberg, J., and I. Grabemann (2001). Variability of the mixing zones and estuarine turbidity maxima in the Elbe and Weser estuaries. *Estuaries and Coasts,* 24, 699-706.
Kappenberg, J., G. Schymura, and H. U. Fanger (1995) Sediment dynamics and estuarine circulation in the turbidity maximum of the Elbe river. *Aquatic Ecology,* 29, 229-237.
Kerner, M. (2007). Effects of deepening the Elbe Estuary on sediment regime and water quality. *Estuarine, Coastal and Shelf Science,* 75, 492-500.
Kostaschuk, R., D. Shugar, J. Best, D. Parsons, S. Lane, R. Hardy, and O. Orfeo (2009). Suspended sediment transport and deposition over a dune: Río Paraná, Argentina. *Earth Surface Processes and Landforms*, *34*(12), 1605–1611, doi:10.1002/esp.1847.
Kostaschuk, R. A., and J. Best (2005). Response of sand dunes to variations in tidal flow: Fraser Estuary, Canada. *Journal of Geophysical Research*, *110*(F4), F04S04, doi:10.1029/2004jf000176.
Kostaschuk, R. A. (2000). A field study of turbulence and sediment dynamics over subaqueous dunes with flow separation. *Sedimentology,* 47, 519-531.
Kostaschuk, R. A., and M. Church (1993). Macroturbulence generated by dunes: Fraser River, Canada. *Sedimentary Geology*, *85*(1-4), 25–37, doi:10.1016/0037-0738(93)90073-E.
Kostaschuk, R. A., and P. Villard (1996a). Turbulent sand suspension events: Fraser River, Canada. In *Coherent Flow Structures in Open Channels*, edited by P. J. Ashworth, S. J. Bennett, J. Best, and S. J. McLelland, pp. 303–319, Wiley & Sons, Chichester.
Kostaschuk, R. A., and P. Villard (1996b). Flow and sediment transport over large subaqueous dunes: Fraser River, Canada. *Sedimentology*, *43*(5), 849–863, doi:10.1111/j.1365-3091.1996.tb01506.x.
Kostaschuk, R. A., and P. Villard (1999). Turbulent sand suspension over dunes. In *Fluvial Sedimentology VI*, edited by N. D. Smith and J. Rogers, Blackwell Publishing Ltd., Oxford, UK, doi: 10.1002/9781444304213.ch1.
Kostaschuk, R. A., J. Best, P. Villard, J. Peakall, and M. Franklin (2005). Measuring flow velocity and sediment transport with an acoustic Doppler current profiler. *Geomorphology*, *68*(1-2), 25–37, doi:10.1016/j.geomorph.2004.07.012.
Kwoll, E., C. Winter, and M. Becker (*2013*). Intermittent suspension and transport of fine sediment over natural tidal bedforms. In *Coherent flow structures at Earth's surface*, edited by J. G. Venditti, J. L. Best, M. Church, and R. Hardy, pp. 231–242, John Wiley & Sons, Ltd.

Kwoll, E., and C. Winter (2011). Determination of the initial grain size distribution in a tidal inlet by means of numerical modelling. *Journal of Coastal Research*, *SI*(64), 1081-1085.

Lapointe, M. (1992). Burst-like sediment suspension events in a sand bed river. *Earth Surface Processes and Landforms*, *17*(3), 253–270, doi:10.1002/esp.3290170305.

Largeau, J. F., and V. Moriniere (2006). Wall pressure fluctuations and topology in separated flows over a forward-facing step. *Experiments in Fluids*, *42*(1), 21–40, doi:10.1007/s00348-006-0215-9.

Lefebvre, A., V. B. Ernstsen, and C. Winter (2011). Influence of compound bedforms on hydraulic roughness in a tidal environment. *Ocean Dynamics*, *61*(12), 2201–2210, doi:10.1007/s10236-011-0476-6.

Lefebvre, A., V. B. Ernstsen, and C. Winter (2013a). Estimation of roughness lengths and flow separation over compound bedforms in a natural-tidal inlet. *Continental Shelf Research*, *61-62*, 98–111, doi:10.1016/j.csr.2013.04.030.

Lefebvre, A., Y. Ferret, A. J. Paarlberg, V. B. Ernstsen, and C. Winter (2013b). Variation of flow separation over large bedforms during a tidal cycle, *Marine and River Dune Dynamics*, pp. 169–175, Bruges, Belgium.

Lefebvre, A., A. J. Paarlberg, and C. Winter (*sub*.). Flow separation and shear stress over angle of repose bedforms: a numerical investigation. *Water Resources Research*.

Levi, E. (1983). A Universal Strouhal Law. *Journal of Engineering Mechanics*, *109*(3), 718–727, doi:10.1061/(asce)0733-9399(1983)109:3(718).

Lin, C. M., and J. G. Venditti (2013). An Empirical Model of Subcritical Bedform Migration. *Sedimentology*. 1-14, doi: 10.1111/sed.12056.

Lu, Y., and R. G. Lueck (1999). Using a Broadband ADCP in a Tidal Channel. Part II: Turbulence. *Journal of Atmospheric and Oceanic Technology,* 16, 1568-1579.

Lu, S. S., and W. W. Willmarth (1973). Measurements of the structure of the Reynolds stress in a turbulent boundary layer. *Journal of Fluid Mechanics*, *60*(03), 481–511, doi:10.1017/S0022112073000315.

Maddux, T. B, S. R. McLean, and J. M. Nelson (2003). Turbulent flow over three-dimensional dunes: 2. Fluid and bed stresses. *Journal of Geophysical Research*, *108*(F1), 6010, doi:10.1029/2003JF000018.

Martin, R. L., and D. J. Jerolmack (2013). Origin of hysteresis in bed form response to unsteady flows. *Water Resources Research*, *49*(3), 1314–1333, doi:10.1002/wrcr.20093.

Martinius, A. W., and J. H. Van den Berg (2011). Atlas of sedimentary structures in estauarine and tidally-influenced river deposits Rhine-Meuse-Scheldt System: Their application and interpretation of analagous outcrop and subsurface depositional systems, EAGE publications, Houten.

Matthes, G. H. (1947). Macroturbulence in natural stream flows. *Transactions American Geophysical Union*, *28*, 255–262.

McLean, S. R., S. R. Wolfe, and J. M. Nelson (1999). Spatially averaged flow over a wavy boundary revisited. *Journal of Geophysical Research, 104,* 15743-15753.

McLean, S. R., J. M. Nelson, and S. R. Wolfe (1994). Turbulence structure over two-dimensional bed forms: Implications for sediment transport. *Journal of Geophysical Research,*99: 12,729-12,747.

Nelson, J., S. McLean, and S. Wolfe (1993). Mean flow and turbulence fields over two-dimensional bed forms. *Water Resources Research*, *29*(12), 3935–3953.

Nezu, I., and H. Nakagawa (1993). Turbulence in open-channel flows. IAHR-Monograph, Balkema, Rotterdam.

Ogink, H. J. M. (1988). Hydraulic roughness of bedforms, *Rep. M2017*.

Omidyeganeh, M., and U. Piomelli (2011). Large-eddy simulation of two-dimensional dunes in a steady, unidirectional flow. *Journal of Turbulence*, *12*(N42), 1–31.

Paarlberg, A. J., C. M. Dohmen-Janssen, S. J. M. H. Hulscher, and P. Termes (2007). A parameterization of flow separation over subaqueous dunes. *Water Resources Research*, *43*, W12417, doi:10.1029/2006WR005425.

Paarlberg, A. J., C. M. Dohmen-Janssen, S. J. Hulscher, and P. Termes (2009). Modeling river dune evolution using a parameterization of flow separation. *Journal of Geophysical Research,* 114, F01014, doi: 10.1029/2007jf000910.

Paarlberg, A. J., C. M. Dohmen-Janssen, S. J. M. H. Hulscher, P. Termes, and R. Schielen (2010). Modelling the effect of time-dependent river dune evolution on bed roughness and stage. *Earth Surface Processes and Landforms*, *35*(15), 1854–1866.

Parsons, D. R., J. L. Best, O. Orfeo, R. J. Hardy, R. Kostaschuk, and S. N. Lane (2005). Morphology and flow fields of three-dimensional dunes, Rio Paraná, Argentina: Results from simultaneous multibeam

echo sounding and acoustic Doppler current profiling. *Journal of Geophysical Research*, *110*(F4), F04S03, doi:10.1029/2004jf000231.
Parsons, D. R., and J. Best (2013). Bedforms: views and new perspectives from the third international workshop on Marine and River Dune Dynamics (MARID3). *Earth Surface Processes and Landforms*, *38*(3), 319–329, doi:10.1002/esp.3360.

Rao, K. N., R. Narasimha, and M. Narayanan (1971). The 'bursting' phenomenon in a turbulent boundary layer. *Journal of Fluid Mechanics,* 48, 339-352.
RD Instruments (2008). ADCP coordinate transformation formulas and calculations. *Technical Report.*
Ren, H., and Y. Wu (2011). Turbulent boundary layers over smooth and rough forward-facing steps. *Physics of Fluids*, *23*(4), 045102, doi:10.1063/1.3576911.
Roden, J. E. (1998). The sedimentology and dynamics of mega-dunes, Jamuna River, Bangladesh. PhD Thesis, School of Geography, University of Leeds.
Rood, K. M., and E. J. Hickin (1989). Suspended-sediment concentration and calibre in relation to surface-flow structure in Squamish River estuary, southwestern British Columbia. *Canadian Journal of Earth Sciences,* 26, 2172-2176.

Saunderson, H. C., and F. P. J. Lockett (1983). Flume experiments on bedforms and structures at the dune-plane bed transition. *Modern and Ancient Fluvial Systems: International Association of Sedimentologists, Special Publication*, *6*, 49–58.
Schmeeckle, M., Y. Shimizu, K. Hoshi, H. Baba, and S. Ikezaki (1999). Turbulent structures and suspended sediment over two-dimensional dunes. In *River, Coastal and Estuarine Morphodynamics*, pp. 261–270, Springer, New York, USA.
Shugar, D. H., R. A. Kostaschuk, J. L. Best, D. R. Parsons, S. N. Lane, O. Orfeo, and R. J. Hardy (2010). On the relationship between flow and suspended sediment transport over the crest of a sand dune, Río Paraná, Argentina. *Sedimentology*, *57*(1), 252–272, doi:10.1111/j.1365-3091.2009.01110.x.
Simpson, R. (1989). Turbulent boundary-layer separation. *Annual Review of Fluid Mechanics*, *21*, 205–234.
Smith, J. D., and S. R. McLean (1977). Spatially averaged flow over a wavy surface. *Journal of Geophysical Research*, *82*(12), 1735–1746, doi:10.1029/JC082i012p01735.
Soulsby, R. L. J. (1980). Selecting record length and digitization rate for near-bed turbulence measurements. *Journal of Physical Oceanography*, *10*, 208–219.
Stark, N., H. Hanff, C. Svenson, V. B. Ernstsen, A. Lefebvre, C. Winter, and A. Kopf (2011). Coupled penetrometer, MBES and ADCP assessments of tidal variations in surface sediment layer characteristics along active subaqueous dunes, Danish Wadden Sea. *Geo-Marine Letters*, *31*(4), 249–258, doi:10.1007/s00367-011-0230-6.
Stoesser, T., C. Braun, M. García-Villalba, and W. Rodi (2008). Turbulence Structures in Flow over Two-Dimensional Dunes. *Journal of Hydraulic Engineering*, *134*(1), 42–55, doi:10.1061/(ASCE)0733-9429(2008)134:1(42).
Strouhal, V. (1878). Ueber eine besondere Art der Tonerregung. *Annalen der Physik*, *241*(10), 216–251, doi:10.1002/andp.18782411005.
Sukhodolov, A. N., J. J. Fedele, and B. L. Rhoads (2006). Structure of flow over alluvial bedforms: an experiment on linking field and laboratory methods. *Earth Surface Processes and Landforms*, *31*(10), 1292–1310, doi:10.1002/esp.1330.
Svenson, C., V. B. Ernstsen, C. Winter, A. Bartholomä, and D. Hebbeln (2009). Tide-driven sediment variations on a large compound dune in the Jade tidal inlet channel, Southeastern North Sea, *Journal of Coastal Research*, *SI 56*, 361–365.

Thorne, P. D., P. J. Hardcastle, D. Flatt, and J. D. Humphery (1994). On the use of acoustics for measuring shallow water suspended sediment processes. *IEEE Journal of Oceanic Engineering, 19*(1), 48–57.
TSI Incorporated (2005). Phase Doppler Particle Analyzer (PDPA)/ Laser Doppler Velocimeter (LDV), Shoreview, USA.

Urick, R. J. (1948). The absorption of sound in suspension of irregular particles. *The Journal of the Acoustical Society of America*, *20*(2), 283–289, doi:10.1121/1.1916937.

Vanoni, V. A., and N. H. Brooks (1957). Laboratory studies of the roughness and suspended load of alluvial streams. Technical Report. California Institute of Technolohy, Pasadena, USA.
van Rijn, L. C. (1993). Principles of sediment transport in rivers, estuaries and coastal seas. Aqua publications Amsterdam.

Venditti, J. G. (2013). Bedforms in sand-bedded rivers. In *Treatise on Geomorphology*, edited by J. Shroder and E. Wohl, pp. 137–162, Academic Press, San Diego, CA.
Venditti, J. G. (2007). Turbulent flow and drag over fixed two- and three-dimensional dunes. *Journal of Geophysical Research*, *112*(F4), F04008, doi:10.1029/2006JF000650.
Venditti, J. G., and B. O. Bauer (2005). Turbulent flow over a dune: Green River, Colorado. *Earth Surface Processes and Landforms*, *30*(3), 289–304, doi:10.1002/esp.1142.
Venditti, J. J. G., and S. S. J. Bennett (2000). Spectral analysis of turbulent flow and suspended sediment transport over fixed dunes. *Journal of Geophysical Research*, *105*(C9), 22,035–22,047, doi:10.1029/2000jc900094.
Villard, P., and R. Kostaschuk (1998). The relation between shear velocity and suspended sediment concentration over dunes: Fraser Estuary, Canada. *Marine Geology*, *148*(1-2), 71–81, doi:10.1016/S0025-3227(98)00015-2.

Wan, Z., and Z. Y. Wang (1994). Hyperconcentrated Flow. A. A. Balkema, Rotterdam, The Netherlands.
Wilkinson, R. H. (1984). A method for evaluating statistical errors associated with logarithmic velocity profiles. *Geo-marine letters*, *3*(1), 49–52.
Winter, C. (2011). Observation and modelling of morphodynamics in sandy coastal environments. Habilitation, Department of Geosciences, University of Bremen.
Winter, C., D. Katoshevski, A. Bartholomä, and B. W. Flemming (2007). Grouping dynamics of suspended matter in tidal channels. *Journal of Geophysical Research, 112*, C08010, doi:10.1029/2005JC003423.
Winter, C., M. Chiou, R. Riethmüller, V. B. Ernstsen, D. Hebbeln, and B. W. Flemming (2006). The concept of "representative tides" in morphodynamic numerical modelling. *Geo-Marine Letters*, *26*(3), 125–132, doi:10.1007/s00367-006-0031-5.
Wren, D. G., R. a. Kuhnle, and C. G. Wilson (2007). Measurements of the relationship between turbulence and sediment in suspension over mobile sand dunes in a laboratory flume. *Journal of Geophysical Research*, *112*(F3), F03009, doi:10.1029/2006JF000683.
Wright, L. D., and B. G. Thom (1977). Coastal depositional landforms: a morphodynamic approach. *Progress in Physical Geography*, *1*(3), 412–459.

Yalin, M. S. (1992). River Mechanics. New York, Pergamon Press.
Yalin, M. S. (1972). Mechanis of sediment transport. Pergamon Press, Oxford.